THE USE OF POLARISATION IN SYNTHETIC APERTURE RADAR

Pierluigi Mancini

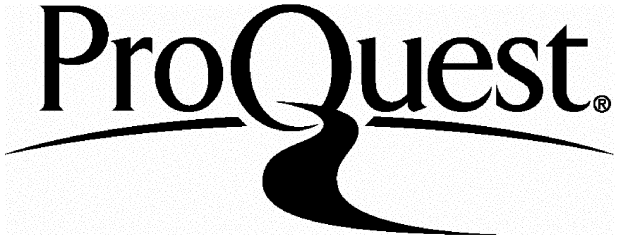

Abstract

The role of Synthetic Aperture Radar (SAR) in remote sensing is of paramount importance. Classically, compared with optical imaging sensors it has two main advantages: the imaging capability independent of weather condition, and the spatial resolution independent of the satellite altitude. Recently the utilisation of airborne SAR has given the opportunity to exploit new instrument concepts. In particular, multifrequency and multipolarisation airborne SARs have shown that improved information about the electromagnetic and geometrical properties of the imaged surface can be obtained. The main objective of this thesis is to show the potential of polarisation information in SARs, and in particular in the use of the Covariance matrix as a second order descriptor for multipolarised SAR images. The relation of the eigenvalues and the eigenvectors of the Covariance matrix with the maximisation of the power backscattered from two areas with different scattering properties is demonstrated applying the Rayleigh maximisation principle. Both for the Gaussian and Gamma clutter models, the potential in obtaining texture information of the span polarimetric image from the knowledge of the eigenvalues of the Covariance matrix is shown. The developed analytical tools are validated with data from multifrequency and multipolarisation SAR airborne campaigns. The definition of a new descriptor of the unpolarised radiation content is introduced and its performance compared against the minimum eigenvalue of the Covariance matrix and the polarisation signature pedestal height. Critical instrument aspects such as range ambiguity contamination, signal-to-noise ratio and alternative orthogonal waveform techniques capable of improving the sensor polarisation performances are also analysed.

Acknowledgements

I wish to thank Douglas Maccoll for having introduced me to the field of microwave remote sensing.

LIST OF CONTENTS

LIST OF FIGURES

LIST OF TABLES

TABLE OF PRINCIPAL SYMBOLS

SAR	synthetic aperture radar
EOS	earth observing system
PO	physical optics
GO	geometrical optics
SPM	small perturbation method
λ	wavelength
SNR	signal-to-noise ratio
B	chirp signal bandwidth
B_s	azimuth spatial frequency bandwidth
B_t	azimuth time frequency bandwidth
rr	range resolution
ra	azimuth resolution
P_t	peak transmitted power
G	antenna gain
N	average thermal noise power
σ	radar cross section
t	pulse time duration
f_r	range sampling frequency
σ_0	uniform normalised radar cross section
c	velocity of light
PRF	pulse repetition frequency
L_r	across track antenna dimension
v	spacecraft velocity
L_a	along track antenna length
STC	sensitivity time control
AGC	automatic gain control
BFPQ	block floating point quantization
BAQ	block adaptive quantization
FFT	fast Fourier transform
SAW	surface acoustic wave

ADC	analog to digital converter
Nr	number of range cells
Mr	range replica size
L	number of looks
Na	number of azimuth lines
Nov	azimuth line overlap
N_{FFT}	FFT size
OPS	number of operations per second
PDF	probability density function
var	variance
sd	standard deviation
MBPS	megabits per second
DRAR	distributed range ambiguity ratio

1. INTRODUCTION

1.1 *Review of Spaceborne SAR Sensors*

The synthetic aperture radar (SAR), together with the radar altimeter and the scatterometer, is one of the most important active microwave instruments for remote sensing. It was first conceived by Wiley in 1951 [1], and since then the SAR has received increasing attention from the remote sensing community. Classically, compared with optical imaging sensor it has two main advantages: imaging capability independent of weather condition and spatial resolution independent of satellite altitude. The first property is due to the use of microwave frequencies while the second is a consequence of the SAR processing.

The first civilian spaceborne SAR was the United States' SEASAT which provided a proof of concept for radar imaging from space [2, 3]. The instrument was designed for a lifetime of two years but due to a failure in the solar panel power system, its mission was reduced to three months (July-September 1978). Due to the lack of on-board recording capability, the SAR was able to operate only during the time periods when it was in view of one of the five ground stations equipped to receive its data, nevertheless it imaged a total area of 126 million square kilometres. Both optical and digital processing techniques were developed for handling SEASAT data.

This first spaceborne SAR was followed in 1981 by SIR A [3], the first of three Shuttle missions devoted to the development of the basic phenomenological understanding and the related quantitative tools to analyse future Earth Observing System (EOS) data.

SIR A was essentially very similar to the SEASAT instrument: due to the short duration of the mission (around three days) together with a halved swath width with respect to the previous one, it was able to optically record the data on board so as to be independent of the ground stations locations.

In 1984 the SIR B was launched. The fundamental difference with respect to previous spaceborne SAR sensors was the multilook angle capability obtained with the use of a mechanically steereable antenna [3]. The main reason for using different incidence angles was the need to generate topographic maps from space. Unfortunately due to failures in the data downlink system and in the antenna signal connections, the objectives of the mission were only partially accomplished.

The next Shuttle mission SIR C / X-SAR, lunched in 1993 and 1994, had multifrequencies (L, C, and X band) and multipolarisation (at L and C band) capabilities [4]. The L and C-band antenna were realised using active phased array technology and for the first time from space, was able to achieve reception of the entire Scattering matrix. The SIR C / X-SAR has been an experimental sensor of fundamental importance due to its unmatched flexibility and technology complexity. It is considered as the last step toward the long design life operational sensor EOS-SAR.

In Europe as well as participating in the third SIR mission with the X-SAR, the European Space Agency has launched in July 1991 the ERS-1 satellite which carries among other instruments a synthetic aperture radar [5]. The planned design lifetime is three years. After the first phase of the mission in which the satellite has been placed in a three day repeat orbit for validation and verification purposes, two different orbit repeat periods were chosen: 35 days for SAR and 176 days for altimetry applications. A follow on mission, ERS-2, very

similar to ERS-1 has been started in 1995 to ensure data continuity to the remote sensing community.

In February 1992 the Japanese remote sensing satellite J-ERS-1 was launched. After some initial difficulties in the SAR antenna deployment mechanism, the sensor is now functioning according to the design specifications. The main J-ERS-1 SAR characteristics are very similar to those of SEASAT except for a larger incidence angle properly tailored for geological application in order to avoid distortion due to height variation of the imaged surface.

In the frame of future planned SARs, an important role is occupied by the Canadian RADARSAT. This sensor, to be launched in 1995, will represent an extremely useful tool for testing new SAR operation modes such as the SCANSAR. In particular, this novel technique will permit an imaged swath width of the order of 500 Km. Beyond that, the unique possibility of rotating the SAR antenna on both sides of the orbital plane will permit the global coverage of the polar regions [6].
The main characteristics of the sensors previously described are listed in Table 1 in the next page. The presence of such a large number of spaceborne SAR realised or to be realised together with the proliferation of experimental airborne activities, clearly demonstrates the importance deemed by the remote sensing community to such an instrument.

SPACEBORNE SAR SYSTEMS							
	Seasat	**SIR-A**	**SIR-B**	**ERS-1**	**J-ERS-1**	**SIR-C / X-SAR**	**Radar-sat**
Frequency (GHz)	1.275	1.278	1.282	5.25	1.275	1.25,5.3 9.6	5.3
Incidence angle (°)	23	50	15 - 64	23	38	15 - 55	20 - 50
Polarisation	HH	HH	HH	VV	HH	MP(L,C) VV(X)	HH
Antenna size (m)	10.7 x 2.16	9.4 x 2.18	10.7 x 2.16	10 x 1	11.9 x 2.4	12 X(3, .75, .4)	15 x 1.5
Noise eq. σ^0 (dB)	-24	-32	-28	-24	-20.5	- 40 ,-28	-23
Range res. (m)	25	40	25	26	18	10 - 30	10 - 100
Azimuth res. (m)	25	40	58 -17	28	18	30	9 - 100
Number of looks	4	6	4	6	3	4	1 - 8
Swath width (Km)	100	50	10 - 60	100	75	15 - 60	10 - 500
Altitude (Km)	800	260	350,225	780	568	225	800

TABLE 1

1.2 *Review of SAR Applications*

The main SAR applications areas can be divided in four categories:

- AGRICULTURE and FORESTRY

- GEOLOGY

- OCEANOGRAPHY

- SNOW and ICE

Due to the electromagnetic interactions between the transmitted pulse and the imaged surface, radar characteristics such as frequency, polarisation and incidence angle play an important role in the backscattering mechanism involved. In the next paragraphs examples of different SAR images will be presented, together with the relevant basic principles of scattering theory.

1.3 *Agriculture and Forestry*

The unique sensitivity of microwave frequencies to surface roughness and dielectric properties makes the SAR a sensor well matched to agriculture and forestry applications. The CO_2 flux from deforestation is a fundamental parameter in the global carbon cycle and it is presently unknown. In the first 10 - 20 years, forests reach their largest biomass to better absorb the solar radiation. Because of this phenomenon the lower canopy cannot be detected by optical instruments and microwave wavelengths are well suited to this type of application. In particular, crop classification, soil moisture analysis, and forest map inventory are areas of recognised interest [7,8].

The backscattered electromagnetic field from an agricultural scene is usually seen as due to three different contributions: a component

related to the vegetation volume, a second one related to the soil surface and a last term describing the interactions between the surface and the vegetation volume. Their relative importance depends on the wavelength, polarisation and incidence angle of the SAR [9].

The soil surface scattering radiation is typically modelled, depending on the values of the correlation length (L) and the root mean square height (σ) of the surface with respect to the radar wavelength, using physical optics (PO), geometrical optics (GO) or small perturbation method (SMP). Both PO and GO are different approximations of the Kirchhoff model. They are mainly based on the assumption that the surface correlation length is comparable with the radar wavelength (i.e. the surface is considered locally flat). No depolarisation effects are involved in these two cases. Typically the PO model finds quite a large application for small incidence angles, while the GO model is able to predict the backscattered field at a wider range of incidence angles mainly due to the larger roughness involved [10].

The SMP model follows the approach used by Lord Rayleigh in acoustics and further developed by Rice in electromagnetics. The surface is described as a sum of spectral components with the major contribution to the backscattered field due to the term satisfying the so-called Bragg resonance condition. Because of its resonant nature, the SMP is sensitive to the small scale roughness of the surface.
The lossy properties of the medium, often related to the moisture content, are taken in account with the introduction of a complex dielectric constant.

The figure in the next page, shows the regions of validity of these different models.

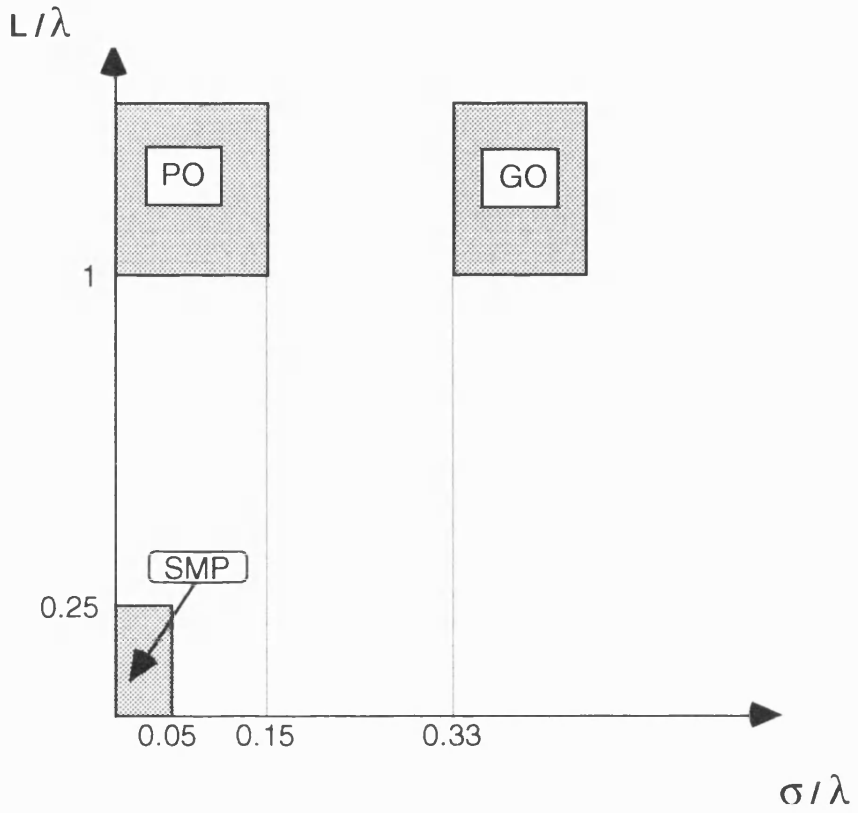

Fig.1.1 Regions of validity of scattering models, L is the correlation length and σ is the root mean square height of the surface

Unfortunately these scattering models fail to cover roughness conditions that often occur in nature, and are incapable of predicting any crosspolarised components unless the SMP is extended to the second order approximation.

In the case of forestry applications several type of models have been used to describe the interaction between the vegetation volume and the soil surface. From several Scatterometer and SAR airborne campaigns, some general conclusions can be drawn: for frequency below 6 GHz and incidence angles smaller than 20 degrees, the main contribution to the backscattered energy is due to the soil surface, on the other hand in the presence of dense canopy for

higher frequencies and larger incidence angles the surface contribution is minimised. In this second case there is a strong component of backscattered unpolarised energy due to multiple scattering taking place in the vegetation volume.

In fig. 1.2 and fig. 1.3 two examples of agricultural and forestry images from the SAR 580 airborne campaign are shown [11]. The SAR 580 was a multifrequency (L, C, X bands) and multipolarisation (HH, VV, HV) instrument operating over a large range of incidence angles in order to optimise the radar parameters for different application areas.

In the first figure, different crop types are imaged with the X band SAR channel. Depending on the vegetation state of each field , the backscattering intensity varies. Indeed the lightest tones are associated with crop types (sugar beet and potatoes) with the largest vegetation volume at that time of the year. The darkest tones are mainly related to the soil surface reflectivity.

In fig.1.3 the two airborne SAR images at L and X band respectively, demonstrate the need for a multichannel capability in order to measure the forest biomass. The imaged area corresponds to a combination of agricultural field and forest. The L band image shows a clear difference between the two, while the X band image due to the decreased penetration depth is only affected by the forest crown volume, therefore making the two different areas of very similar tone.

Fig.1.2 SAR 580 image, X band, HH polarisation, agricultural fields (after M.G. Wooding, 1988)

A

B

Fig.1.3 SAR 580 images, HH polarisation, forested areas and agricultural fields, **A**. L band **B**. X band (after M.G. Wooding, 1988)

1.4 *Geology*

The main areas of interest in geology are subsurface, geomorphological and topographic mapping. The penetration capability of the SAR electromagnetic signal in very dry surfaces has been demonstrated during the SIR A mission. Indeed the imaging of old river channels, buried in few metres of dry sand cover in the Egyptian desert, was one of the most striking results of that experiment.

Topographic applications utilise techniques such as stereo imaging, or more recently SAR interferometry. In the stereo technique the same scene is seen from two slightly different positions, and through the image feature difference analysis, information related to the relief is retrieved. This technique is able to achieve accuracy of the order of ten metres, however for such precision it is necessary to have a very similar image quality, thematic characteristics (tone and texture) and illumination of the scene. The SIR B provided the first stereo images from space due to its multilook angle capability.

SAR interferometry uses the wave interference of two phase displaced images of the same area to determine topographic information. This technique can be exploited using an instrument with two antennas or using multiple satellite passes of a conventional SAR. Like most interferometric techniques the results are corrupted by 'phase wrapping'. To demonstrate the concept, several experiments have been performed using airborne dual antenna SAR and data from adjacent orbits from spaceborne SAR. The main conclusion has been that an instrument optimised for interferometric spaceborne application could be able to reach a height accuracy of the order of metres [12].

The use of SAR 'third dimension' techniques in geology applications, is a very promising tool to generate topographic global mapping with high spatial resolution and height accuracy independently of weather conditions.

1.5 *Oceanography*

The understanding of SAR ocean wave imagery is the subject of many scientific researches in the world. The study of the interaction of the transmitted electromagnetic wave with a moving target such as the ocean together with the use of coherent Doppler processing is obviously a very complex problem and several attempts have been made to explain it. The main sources of backscattered energy are the short gravity waves due to the resonant interactions with the microwave SAR transmitted signal (SMP scattering). However these waves will typically have wavelength smaller than SAR resolution and therefore their contributions will appear as a modulation of the reflected energy from larger swells and wind waves. Three theories have essentially been proposed to explain SAR ocean scattering: tilt, roughness and orbital velocity modulation [13].

The tilt modulation describes the scattering mechanism through the variation of the local incidence angle. This model is very sensitive to different transmitted polarisation and wave direction. Indeed it shows a larger modulation for horizontal polarisation and for wave travelling normally to the line of flight.

In the case of roughness modulation, the model considers the increased roughness on the forward face and the smoothing effect on the backward face of the large wave as the major cause of reflectivity modulation. This interpretation is therefore associated with the variation of the surface roughness spectrum in the Bragg resonance condition. This type of modulation is weakly dependent on

the wave direction and on the polarisation of the transmitted electromagnetic waves.

The orbital velocity modulation explains the scattering mechanism through the analysis of the extra doppler shift due to this velocity component in the SAR image formation. This effect is capable of modulating the scattering particle density and therefore the ocean reflectivity. This model is not able to justify the imaging of large waves travelling parallel or perpendicular to the sensor track. The figure below shows for the three different models considered, the different sensitivities to the angle between the line of flight and the wave direction.

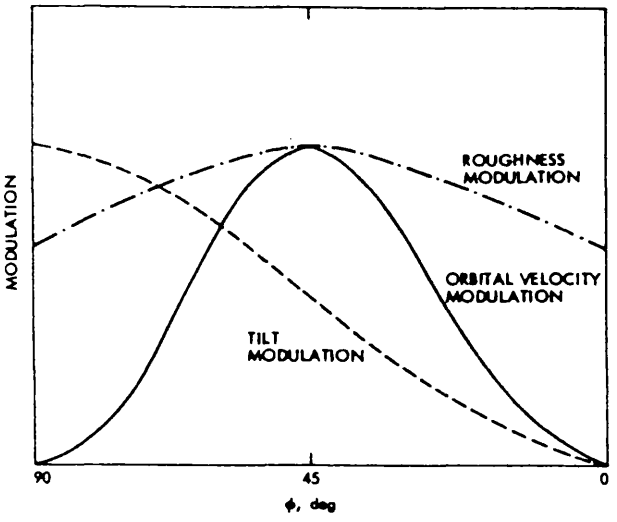

Fig.1.4 Modulation dependence on angle between sensor track and wave direction (after C.Elachi and W.E. Brown, 1977)

In general the three modulation effects will exist simultaneously and depending on the local wind condition and the relative geometry between the wave and the sensor, their contributions will vary.

The application of SAR in oceanography is not only limited to surface waves. Information on oil spills, internal waves, current patterns and bottom bathymetry have also been retrieved due to their capability of producing a surface signature in terms of relative velocity or surface roughness [14].

The potential of ocean oil spill detection using SAR was already demonstrated in the SEASAT and SIR-A missions. To confirm the first qualitative results, a large amount of oleyl alcohol was discharged near the coast of Japan during the SIR-B flight. The spill was imaged by the SAR over a 1 km x 2.5 km area. The interaction of the alcohol with the sea surface simulated the damping effect of the oil on the small scale surface roughness. An example of this phenomenon can be seen in the SEASAT image in figure 1.5. The oil slick in the left corner of the image has a darker tone due to the decreased backscattered energy.

A very useful way to display SAR sea data is by the use of the directional wave spectrum. It shows the direction, the spatial wavelength and the energy of the sea waves in a wave number polar format. Typically it will exhibit a 180 degree ambiguity that is resolved through the knowledge of local wind direction. Due to the SAR imaging mechanism, there are several difficulties in extracting quantitative information from directional wave spectrum. The energy content is biased towards lower wave numbers and it strongly affected by the presence of speckle. The speckle filtering is a very critical issue due to the correlation from pixel to pixel induced by the SAR impulse response function. A filtering approach working directly on the SAR complex image has proved to be very successful [15]. A typical example of directional wave spectrum taken from the JPL

multipolarisation airborne SAR is shown in figure 1.6. There is evidently a very large speckle component. A strong contribution from large wavelength can be identified. The small difference between the two polarisations is also remarkable [16].

The use of the SAR in oceanography is of paramount importance. Several important open questions remain in its capability of imaging azimuth travelling waves and in the modelling of the electromagnetic interaction. The importance of tilt modulation with respect to orbital or roughness modulation will certainly be explored with future advanced sensor due to their multifrequency, multiangle and multipolarisation capabilities.

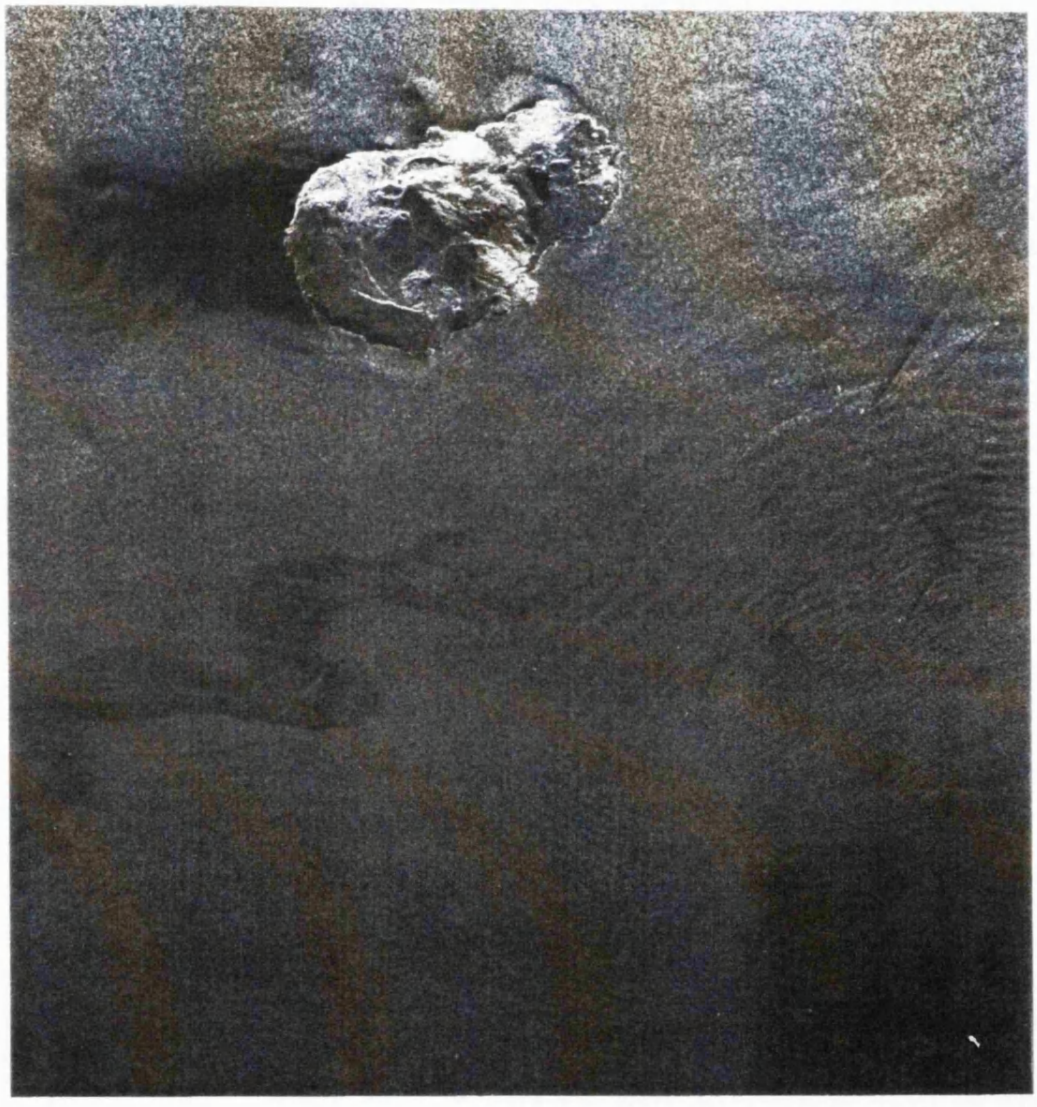

Fig.1.5 Seasat image, oil slick near the island of Pantelleria, HH polarisation, L band (after M.G. Wooding, 1988)

A

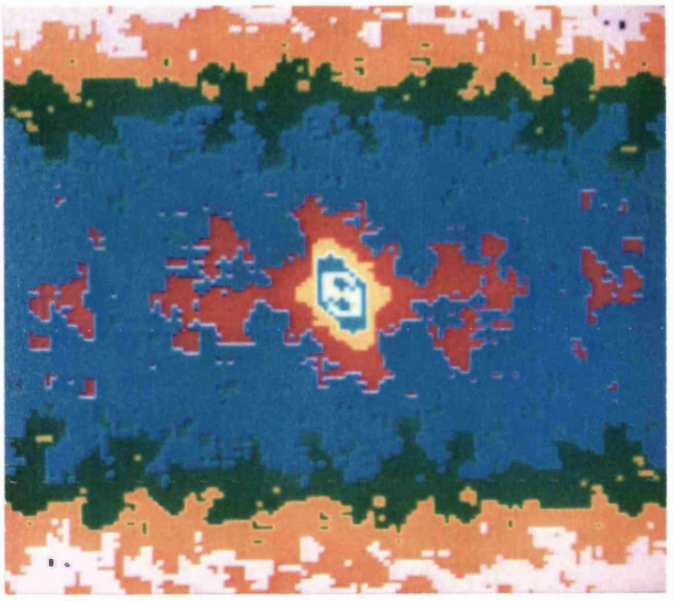

B

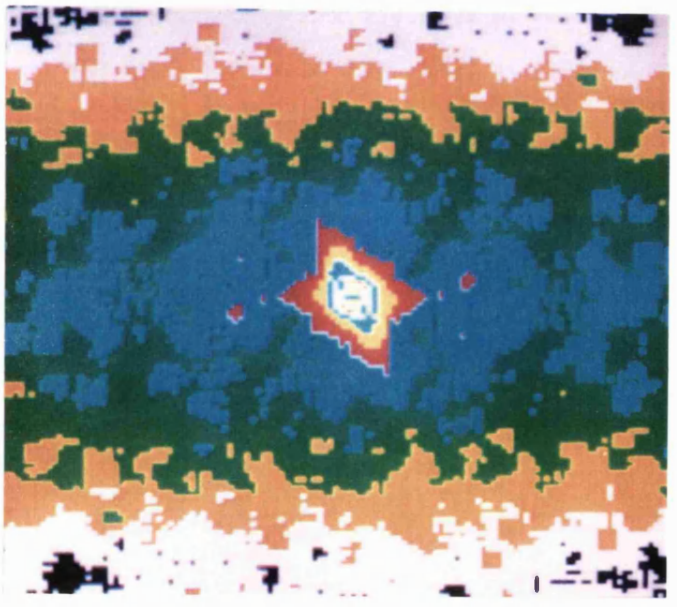

Fig.1.6 Directional wave spectrum, (a) VV polarisation, (b) HH polarisation, L band, JPL multipolarisation airborne SAR (after L.M.J. Brown, J.A.Conway, J.T.Macklin, D.C.Brewster and N.R.Stapleton, 1989)

1.6 *Snow and Ice*

Most of the world's fresh water is frozen. The periodic mapping of sea ice distribution is of fundamental importance for the understanding of the global energy budget. Indeed both the heat fluxes from the sea to the atmospheric boundary layer and the fluxes of surface heat into the deeper ocean are strongly affected from the ice thickness [17]. Due to the high spatial resolution of the SAR, fine scale measurement of sea ice motion, type and concentration can be realised. First year sea ice has typically much higher surface salinity content and smaller roughness with respect to multi-year sea ice. Glaciers, river and lake ice on the contrary are practically pure ice and therefore with a larger volumetric scattering component.

The monitoring of the accumulation and melting of the seasonal snow cover is also very important due to its direct effect on the albedo and water balance. For these types of applications a multipolarisation and multifrequency SAR is highly desirable due to its intrinsic capability to explore anisotropic media at different penetration depths.

Figure 1.7 shows an example of the SAR capability in ice discrimination: the brightest zones correspond to thick multi-year ice and the dark areas are essentially first year ice(*).The SAR sensitivity to small scale surface roughness is quite remarkable.

The SAR has also found application in mapping the extent of glacial ice. Figure 1.8 shows an example of this capability using a SEASAT image of ice caps in Iceland. In the upper right corner the glacial ice can be recognised. The grey uniform tone is explained by the flat undisturbed surface ice. The light tone is probably related to specular reflection by the steep ice slope present at the edge of the ice caps.

(*) or open water

Fig.1.7 Seasat image, multi-year ice (light tones) and new ice (dark tones), HH polarisation, L band, (after M.G.Wooding, 1988)

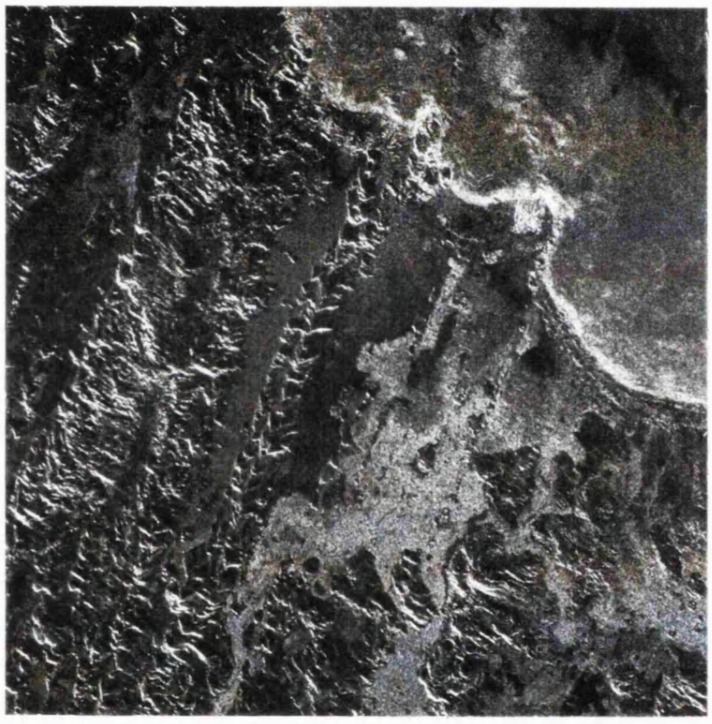

Fig.1.8 Seasat image of ice caps in Iceland, HH polarisation, L band, (after M.G.Wooding, 1988)

1.7 *SAR polarimetry*

From the review of the major application areas the need for a more versatile SAR is evident in order to satisfy the scientific and commercial objectives. In particular, a multifrequency and multipolarisation SAR with variable incidence angle is highly desirable.

The potential of sensing the scene with different wavelengths will provide an improved understanding of the electromagnetic interaction mechanism. It will be of paramount importance for sensing the total vegetation biomass, in providing subsurface mapping capability, and in measuring the effect of small gravity waves with respect to the capillary waves in the Bragg scattering.

On the other hand the multipolarisation capability will allow us to have a complete vectorial picture of the scene. Any type of scatterer acts as a polarisation transformer; therefore in order to have a full understanding of the phenomena, the vectorial nature of the electromagnetic field cannot be neglected. The potential for separation and measurement of soil and vegetation moisture, the ability in classifying forest canopy using the crosspolarised channel information and the unique feature of detecting different scattering mechanism contributions in ocean and ice scattering makes the multipolarisation capability a need for future SAR sensors.

Most of the effort in SAR polarimetry has been devoted to the realisation of an instrument able to receive the copolar and crosspolar components of the backscattered echo. The proper combination of the receiving channels, together with an alternate polarisation transmission capability, has been used on the ground to synthesise any desired polarisation. A large variety of techniques has been applied on polarimetric SAR data in order to improve the interpretation of the information associated with the Scattering matrix

or other more complex second order descriptors of the vectorial information.

The main objectives of this thesis are therefore to show the potential of polarisation information in SAR, and in particular in the use of the Covariance matrix as a second order descriptor for multipolarised SAR images. The application of the eigenvalues of the Covariance matrix for the characterisation of multipolarised SAR images will be presented together with the physical interpretation.

1.8 *Summary of structure of rest of thesis*

The second chapter will be devoted to the fundamentals of SAR theory. Speckle noise, azimuth and range ambiguities, bidimensional matching filter theory and SAR radar equation will be reviewed.

In the third chapter the basis of SAR polarimetry will be presented. A summary of scattering theories with application to experimental SAR polarisation signatures from airborne SAR campaigns will be shown in order to realistically demonstrate the theoretical results.

In the fourth chapter a detailed analysis of new applications of the Covariance matrix descriptor will be presented. The eigenvalues of the Covariance matrix will be analytically demonstrated to be associated with the intrinsic spatial variability of the span image, and the eigenvectors will be related to a Rayleigh quotient maximisation problem. Different ways to associate physical meaning to the eigenvalues will be shown (target randomness, unpolarised image content, polarisation matching capability).

In the fifth chapter the previously analysed approaches will be applied to experimental airborne SAR data. Several SAR images corresponding to different type of scattering mechanism will be considered. The effect of instrument anomalies, such as poor signal-

to-noise ratio, antenna polarisation isolation and instrument reciprocity will be analysed. An alternative approach capable of deriving useful polarimetric information before SAR processing directly on raw data will be considered. Its potentials in correcting the lack of instrument reciprocity will be demonstrated.

In the last chapter the main results of the thesis will be summarised. The concepts with greatest potential will be highlighted and ideas for future research work will be proposed.

Although not quoted explicitly, references [104]-[111] are also relevant to this thesis.

2. SAR THEORY

2.1 *Matched filtering in SAR*

A parameter of fundamental importance for remote sensing sensors is the spatial resolution. It is often expressed as the ability of the instrument in differentiating two closely spaced target of similar brightness. For a real aperture radar the spatial resolution is directly proportional to the transmitted wavelength λ and the target range R and inversely proportional to the aperture diameter D. The human eye, being itself a real aperture (i.e. the pupil section), has a resolution of typically 3 metres at a distance of 10 km. To be capable of achieving the same resolution at microwave frequencies it is necessary to use antenna dimensions of the order of hundreds of metres. This is the fundamental reason why for remote sensing applications in order to have spatial resolutions at microwave frequencies of the order of metres, it is necessary to use a synthetic aperture approach.

The SAR uses a two dimensional matching filtering approach to resolve targets located inside the antenna footprint. In this application, the matched filtering is not used to optimise the signal-to-noise ratio (SNR), but only to achieve a required spatial resolution. To explain this fundamental concept, it is assumed in the following formulation that the system is linear, therefore the analysis can be limited to a point target without loss of generality.

The response of a linear stationary filter matched to an input signal s can be expressed as [18]:

$$y(t) = \int_{-\infty}^{+\infty} s^*(t_d-\tau)\, s(t-\tau)\, d\tau \qquad 2.1$$

where t_d is the time delay between the signal and filter impulse response function. The above expression represents the autocorrelation function of the signal s with respect to a reference delay time t_d. It is worthwhile to note that matched filtering corresponds to correlation processing. For $t=t_d$ the output of the matching filter is equal to the energy of the signal s. Because the autocorrelation function is related to the signal power spectral density through the Fourier transform, for $t_d=0$ the matched filter output is linked to the Fourier transform S(f) of the input signal s(t) in the following way:

$$y(t)=\int_{-\infty}^{+\infty} |S(f)|^2 \exp(-j2\pi ft)df \qquad 2.2$$

The above formula demonstrates that the output signal of the matching filter will have a significant contribution for a time proportional to the inverse of the input signal bandwidth B (under the assumption that S(f) has a more or less uniform behaviour). A simple proof of the previous consideration can be easily done by considering a constant magnitude spectrum $|S(f)|=K$ over a bandwidth B centred at an offset frequency f_C, then the filter output will take the familiar form:

$$y(t)=K^2 B e^{-j2\Pi f_C t}\left[\frac{\sin(\pi Bt)}{\pi Bt}\right] \qquad 2.3$$

The next figure shows the normalised intensity of the previous expression for three different values of B.

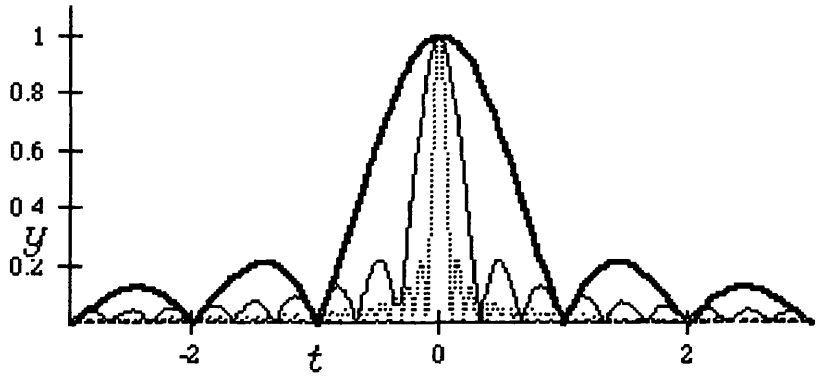

Fig.2.1 Output intensity of the matched filter for a constant magnitude input spectrum with relative bandwidths: B=1 thick line, B=3 normal line, B=10 dotted line

The width of the main lobe of the matched filter output depends only on the bandwidth of the input signal B, therefore the use of matched processing decouples the time resolution of the filter output from the duration of the input pulse. As important consequence of using a longer pulse length is the relaxation of peak power from the transmitting amplifier without affecting the detectability requirements. In order to exploit this technique, it is necessary to generate signals for which the time-bandwidth product is larger than unity. Classically in SAR a linear frequency modulated pulse or "chirp" has been employed for this task, mainly due its capability to remain phase matched for Doppler frequency shift affecting the radar received signal [18,19,20]. Indeed a small frequency translation of the received spectrum with respect to the signal bandwidth will mainly result in a modest decrease of the matched filter output peak amplitude (it can be demonstrated that the error due to the frequency translation approximation of the Doppler effect is negligible if the product of radar line of sight target/sensor velocity and the time-bandwidth product of the transmitted pulse are smaller than the velocity of propagation [18]).

The amplitude spectrum of a chirp signal for time-bandwidth products larger than 100 contains approximately 98 per cent of the signal energy within the chirp frequency sweep B [19]. The figure below shows three amplitude chirp spectra for different time-bandwidth products [20].

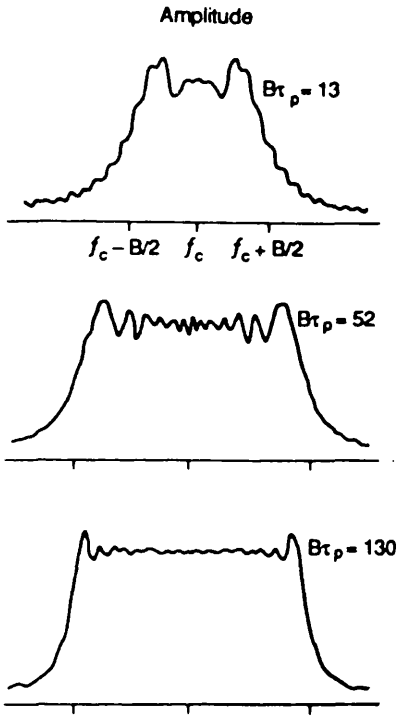

Fig.2.2 Linear FM amplitude spectra for different time-bandwidth products (after J.C.Curlander and R.N.McDonough, 1991)

Therefore for time-bandwidth products larger than 100, as often is the case in SAR applications, a sharp cut off dispersive filter properly matched to the transmitted linear frequency modulation will very closely resemble the optimum matched filter. The output pulse envelope will follow the typical sin(t)/t form, consequently the amount

of the input signal energy not allocated in the compressed pulse length will appear in the sidelobes of the matching filter response. It is interesting to note that since thermal noise is characterised as samples from a white stationary Gaussian process, it will remain uniformly spread over the uncompressed pulse length. The matched filter will essentially concentrate the input signal energy on a shorter time interval 1/B with an associated increase in SNR (compression gain) and a corresponding degradation outside the compressed pulse length.

In the case of a multitude of adjacent point targets, the matched filter processing will enable them to be resolved for differential time delay larger than 1/2B (note the factor 2 is necessary because of the two-way propagation of the radar), however, due to the overlapping of sidelobes belonging to adjacent resolved targets, the SNR will essentially remain unchanged (in other words the decreased reflecting area due to the improved resolution will balance the compression gain in the SNR).

The SAR, to resolve scatterers inside the antenna footprint, must generate a coherent frequency variation over each target. In range this is achieved on a single pulse basis using a chirp pulse radar approach, in azimuth it is necessary to use the information related to several transmitted pulses and the sensor motion. If the SAR is flying along a straight line x according to figure 2.3, the reflected signal is:

$$E = A \exp(-j2Kr) = A \exp(-j2\omega r/c) \qquad 2.4$$

where c is the velocity of propagation, ω is the radar radian frequency (note the term $\exp(j\omega t)$ is implicitly assumed in all the formulae).

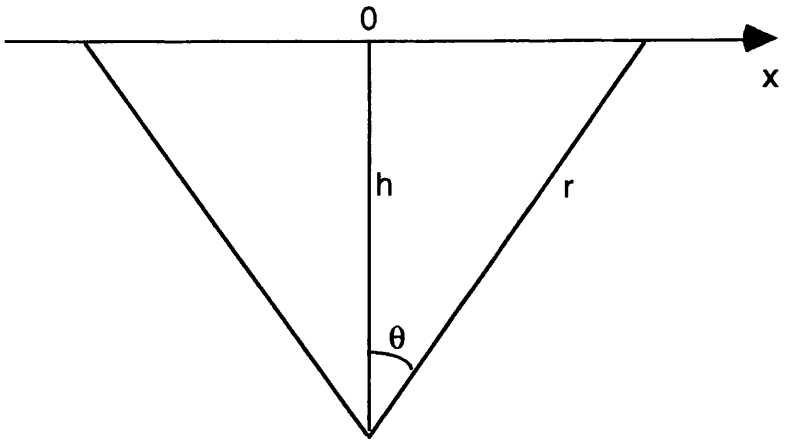

Fig.2.3 Synthetic Aperture Radar along track geometry

The spatial frequency of this signal is:

$$f_s = \frac{1}{2\pi}(d\Phi/dx) = -2f/c\,\frac{x}{\sqrt{x^2+h^2}} \qquad 2.5$$

and the total azimuth spatial frequency variation is :

$$B_s = (4f/c)\sin\theta \qquad 2.6$$

This parametric variation of the spatial frequency versus angle can be easily translated into the classical temporal Doppler frequency versus angle through the sensor velocity. The ability of the SAR to generate such a coherent frequency variation with the use of the Doppler effect is the key factor to achieve improved along track (azimuth) spatial resolution.

The chirp bandwidth B and the spatial Doppler bandwidth B_s will allow after range and azimuth matching processing, to achieve a range resolution rr and an azimuth resolution ra equal to:

$$rr = c/(2B\sin\alpha) \qquad 2.7$$

$$ra = 1/B_s = c/(4f \sin\theta) \qquad 2.8$$

where α as illustrated in the figure below, is the range elevation angle.

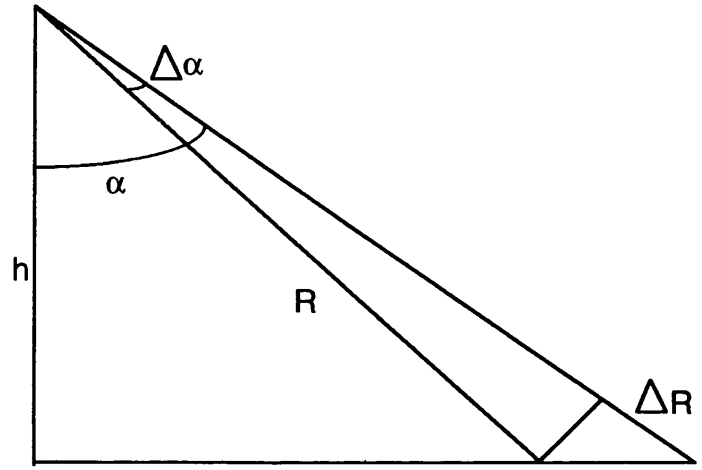

Fig.2.4 Synthetic Aperture Radar across track geometry

Using the small angle approximation ra becomes:

$$ra \approx \frac{c}{4f\theta} = \frac{L_a}{2} \qquad 2.9$$

where L_a is the azimuth antenna length. This is a result of paramount importance since it demonstrates the independence of SAR azimuth resolution of range and wavelength. From equation 2.8 it appears that the maximum azimuth resolution is obtained for a field of view of 180 degrees. For this case ra is equal to $\lambda/4$ which seems quite unrealistic. However in applications such as active seismology this level of resolution has been approached.

In the case of spaceborne application, it should be emphasised that the angle θ corresponding in equation 2.9 to half of the antenna 3 dB power beamwidth, shall be intended as:

$$\theta_{effective} = \frac{V_{sc}}{V_{beam}} \theta \qquad 2.10$$

where V_{sc} is the spacecraft velocity and V_{beam} is the velocity of the antenna beam on the earth surface. This substitution expresses the fact that due to the sphericity of the earth, the angle over which the scatterer is viewed from the sensor is increased with respect to the flat earth geometry. Indeed the conic sections of constant Doppler frequency generated from the spacecraft motion depend on V_{sc}, but the SAR integration time depends on V_{beam}. For spaceborne applications, V_{sc} is larger than V_{beam} in order to compensate the effect of the rotation of the satellite as it travels along the orbit [21].

2.2 *The SAR radar equation*

The SAR radar equation can be defined at two stages: at raw data level (essentially before range and azimuth compression), and at image level (after SAR processing). To further clarify the effect of compression of the received signal, both point and distributed targets will be considered. For the point target case, the implicit assumption that the power reflected from the background clutter is negligible with respect to the point target return will be used. The received peak power from a target of radar cross section σ is:

$$P_r = \frac{P_t G_t G_r \lambda^2 \sigma}{(4\pi)^3 R^4} + N \qquad 2.11$$

where P_t is the peak transmitted power, G_t and G_r are respectively the transmit and receive antenna gains, λ is the radar carrier wavelength, R is the slant range and N is the average thermal noise

power (white stationary Gaussian process is assumed). It is interesting to note that both speckle and ambiguity noises are considered as an inherent part of the useful signal. The propagation effects are neglected since they will mainly contribute in terms of attenuation. The received power from a point target at image level is:

$$P_{ri} = n^2 P_r + nN \qquad 2.12$$

where n is the product of range and azimuth samples integrated during the respective compression processing. The previous formula assumes a SAR processor without any losses due to mismatch or weighting of the reference functions. The different effect of the matching processing on the received signal and the thermal noise is due to the decorrelation among noise samples. In the range compression, the number of coherently integrated samples n_r is equal to the product of the pulse time duration t and the range sampling frequency f_r. In the azimuth compression, the number of samples n_a is equal to the product of the time the target is observed by the antenna pattern and the sampling frequency of the radar. In analytical form this can be expressed in the following way:

$$n_a = \frac{\lambda R}{2 v ra} PRF \qquad 2.13$$

$$n = t f_r \left(\frac{\lambda R}{2 v ra} PRF \right) \qquad 2.14$$

From the expression (2.12), it is evident that the ratio of peak power to average noise power is increased after processing proportionally to the total number of coherently integrated samples (compression gain). It is important to note that the variation in range dependence is caused by the azimuth integration time requirement to maintain a constant azimuth resolution across track.

In the case of a distributed target, the received power is intended as mean power averaged over all the elementary scatterers of the statistically homogeneous scene [22]. The mean received power before compression (i.e. raw data) is:

$$P_{rm} = \frac{\sigma_0 P_t G_t G_r \lambda^2 c\, t\, \Delta\theta}{(4\pi)^3 R^3\, 2 \sin\alpha} + N \qquad 2.15$$

where σ_0 is the uniform normalised radar cross section (sigma zero) and $\Delta\theta$ is the 3 dB azimuth antenna power beamwidth. In this case the reflected power corresponds to the uncompressed resolution cell. The mean received power at image level is:

$$P_{rmi} = n^2 \frac{\sigma_0 P_t G_t G_r \lambda^2 rr\, ra}{(4\pi)^3 R^4} + nN \qquad 2.16$$

For the distributed target case, the assumptions of a perfectly focused SAR processor and of a large scene and propagation medium coherence time with respect to the SAR integration time are not necessary. The only effect due to the presence of these errors will be a deterioration of the SAR spatial resolution and not of the average received power because of the redistribution of the mismatched energy in the adjacent resolution cells [23,24].

For the distributed target, the ratio of the SNRs before and after compression is equal to:

$$\frac{SNR_{image}}{SNR_{raw\ data}} = \left(\frac{PRF}{2v\Delta\theta/\lambda}\right)\left(\frac{f_r}{c/2rr}\right) \qquad 2.17$$

The above expression demonstrates that except for an oversampling factor, there is no compression gain for distributed targets. The main reason of this "oversampled gain" is due to the overlapping of the

SAR impulse response function of adjacent pixels [21]. This effect depends only on the pixel spacing and not on the SAR resolution.

2.3 *Range and azimuth ambiguities*

Due to the radar pulsed nature, the SAR performances are limited by the presence of ambiguities. They are traditionally divided into two main categories: range and azimuth ambiguities. Range ambiguities occur if two or more reflected echoes due to different transmitted pulses and ground locations are received simultaneously. In particular the range ambiguous regions are the areas outside the SAR useful swath whose slant range differs from that of the desired return by a factor equal to a multiple of c/2PRF. Referring to figure 2.4, to avoid range ambiguities it is necessary that the elapsed time between two transmitted pulses is larger than the time necessary to travel (two way) the slant swath width ΔR. Neglecting earth curvature and assuming a small angle $\Delta\alpha$, the following relations apply:

$$\Delta R = \left(\frac{h\Delta\alpha}{\cos\alpha}\right)\tan\alpha \qquad 2.18$$

$$\frac{c}{2PRF} \geq \Delta R \qquad 2.19$$

$$PRF \leq \frac{c\, L_r \cos^2\alpha}{2\lambda h \sin\alpha} \qquad 2.20$$

where L_r denotes the across track antenna dimension. From the above formula the upper bound on the PRF choice imposed by the need of avoiding range ambiguities is evident. Typically the sub-satellite (nadir) return is associated with the highest ambiguous energy due to its shortest range and the largest scene reflectivity. To avoid this range ambiguity without imposing stringent requirements

on the antenna sidelobes, the PRF is chosen so that the SAR transmission time and the reception of the nadir return coincide.

The azimuth ambiguities are due to aliased returns corresponding to Doppler frequencies whose differ of multiple of PRF with respect to the frequency history of the unambiguous return. For a SAR operating in a broadside configuration (i.e. the antenna beamwidth perpendicular to the sensor velocity), the total temporal frequency Doppler bandwidth B_t extends from $-v/L_a$ to v/L_a (where v is the spacecraft velocity and L_a is the along track antenna length). To properly sample this bandwidth, the PRF should be larger than the Doppler bandwidth B_t. The need of azimuth ambiguities suppression imposes a lower bound on the PRF choice. Combining the two ambiguity conditions, a minimum limit of the SAR antenna area is defined [3, 25]:

$$L_a L_r > \frac{4 \lambda h v \sin \alpha}{c \cos^2 \alpha} \qquad 2.21$$

Even if the SAR characteristics satisfy the inequality above, ambiguities will always occur. Indeed due to the finite antenna dimensions, a perfect shaped beam able to satisfy the range and azimuth ambiguity requirements cannot be synthesised.

The direct dependence of ambiguous returns on fundamental instrument characteristics is often used to describe ambiguity effects on the processed SAR images. In particular, the Doppler frequency history of the received signal of a spaceborne SAR can be approximately expressed as [26, 27]:

$$f(t) \approx f_{DC} + f_{DR}\, t \qquad 2.22$$

$$f_{DC} \approx -\frac{2 v \sin \theta}{\lambda} \qquad 2.23$$

$$f_{DR} \approx -\frac{2v^2}{\lambda R} \qquad 2.24$$

where f_{DC} and f_{DR} are respectively the Doppler centroid and the Doppler frequency rate of the received signal.

Depending on their slant range positions, range ambiguities will generate a highly dispersed image due to the mismatch of the FM rate between the received ambiguous range echo and the matched filter response. Azimuth ambiguities will mainly present difference of PRF multiple in the Doppler centroid. Due to the limited range variation along track, f_{DR} will remain unchanged. The effect of mismatch in the Doppler centroid will result in a displacement of the ambiguous target from its true location. This effect is strongly dependent on the SAR carrier frequency. Indeed for high frequency SAR, the displacement can be comparable with the resolution cell size. In this case, it is possible to generate focused images using aliased Doppler centroid at a price of a misregistration of the pixel location on the earth surface. To avoid this complication, multiple PRF techniques have been studied for estimating the correct Doppler centroid [20].

2.4 *Speckle Noise*

Images obtained by a coherent sensor (such as SAR or laser) are contaminated by a kind of multiplicative noise called speckle, which comes from multi-path interference of coherent waves scattered from a distributed target. Because of this type of noise, the SAR image of a statistically homogeneous surface will show brightness variations with the most probable intensity value at any point in the image equal to zero [28,29]. Speckle is considered an undesirable effect in the SAR image and it is often believed that the potential of using such an instrument for quantitative remote sensing will always be limited by the presence of this noisy component. In order to describe the

speckle phenomena, a simplified target geometry will be analysed. Consider two identical backscattering points, separated by a distance d, within the antenna beamwidth of a SAR flying at velocity v as shown in the figure below:

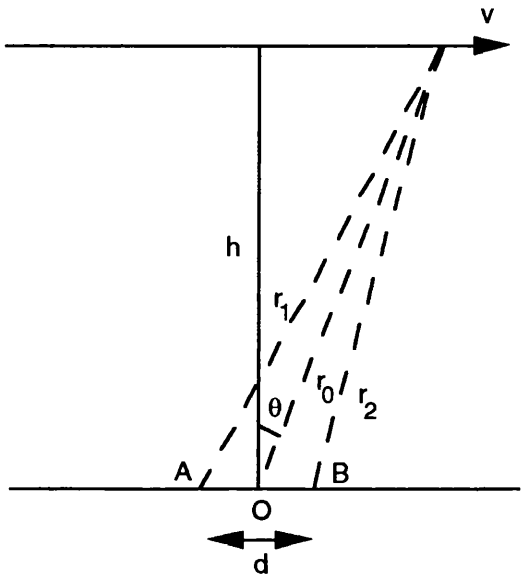

Fig.2.5 Plan view of geometry of the sensor and scatterers, A and B

The received amplitude S will vary according to the interference pattern:

$$S = 2\left|S_0 \cos\left(\frac{2\pi}{\lambda} d \sin\theta\right)\right| \qquad 2.25$$

where d is assumed much smaller than r_0. Due to the platform motion, the angle dependence can be changed to a dependence on time. Consequently, with all pairs of scatterers we are able to associate a frequency proportional to their separation d through the relation $f = 2vd/\lambda h$ (note the presence of the factor 2 is due to our interest in characterising the speckle random process through its power spectrum).

Due to the surface roughness, the various contributions at the same speckle frequency can be considered to add incoherently. For an antenna of along track length L_a, the total bandwidth of the speckle power spectrum will be equal to $2v/L_a$, and each frequency component will have a magnitude proportional to the number of possible pairs at separation d within the antenna footprint. More precisely, the frequency component of the speckle power spectrum will be the average performed over microscopically different scenes with the same macroscopic properties (ensemble). The zero frequency component will essentially be related to the mean reflectivity (sigma zero) and will generate the largest spectral component, being associated with the interactions of the scatterers with themselves [30,31]. The total bandwidth of the speckle power spectrum is also equal to the total Doppler frequency excursion of a point target echo. Due to the fact that the integration time of the sensor is always greater than the decorrelation time of the speckle, that is:

$$\frac{\lambda h}{L_a v} > \frac{L_a}{2v} \qquad 2.26$$

it is possible to perform an average of uncorrelated samples of the backscattered electromagnetic field to provide a better estimate of its mean value (sigma zero), at the inevitable price of a degradation of the azimuth resolution.

The same kind of argument will hold in the range dimension. However, due to the different compression technique involved, the bandwidth of the speckle power spectrum will be proportional to the chirp bandwidth. Indeed for the range dimension, the distance d in the expression (2.25) is equal to $ct/2\sin\theta$, where θ is now the local slant range incidence angle. In this case the speckle decorrelation time will be comparable to the compressed pulse length and therefore always smaller than the range integration time (pulse

length). The same conclusions could be reached by applying the Van Cittert-Zernicke theorem [32].

Speckle can also be seen as the result of a coherent filtering processing over a wide bandwidth random process. Consequently the speckle autocorrelation function will strongly resemble the SAR impulse response function and speckle will therefore be highly correlated for pixel distances smaller than the SAR resolution.

In order to combat speckle, it is necessary to perform an incoherent summation of uncorrelated samples of the SAR signal at a price of a degradation of the spatial resolution. The effect of this incoherent averaging operation is to decrease the normalised standard deviation of the sum of a factor proportional to the square root of the samples (looks). Typically to smooth speckle noise, two techniques can be envisaged: the averaging can be performed at pixel basis over the full resolution, image or splitting the integration time in the SAR processing in order to create look images that eventually are combined incoherently to generate the final image [33]. The first approach is often used in practice due to the flexibility in choosing the required spatial resolution and the level of speckle reduction appropriate for the specific application. The main drawback of this technique is the need to perform the SAR processing for the full resolution with a consequent large computational load. In the second scheme the splitting of the integration time, often performed in the azimuth direction because of the potential available finer resolution, allows the direct processing of low resolution images with a large computational saving. In this case, the total Doppler bandwidth is typically split into non-overlapping fractions (looks) using zero phase shift bandpass filters and then the output of each filter is subsampled in order to remove redundant information. The overall computational saving is therefore due to the decreased integration time and to the resultant reduced PRF. Consequently, the total amount of processed pulses is reduced by N^2, where N is the number of looks.

An alternative approach to reduce speckle is to exploit the antenna pattern effect on the speckle power spectrum [30]. From expression (2.25), $u=\sin\theta$ and $f=2d/\lambda$ can be considered the new Fourier transform pair. Physically f represents the rapidity of signal fluctuations with angle. For the azimuth direction, the speckle spatial bandwidth defined by the 3dB antenna beamwidth is equal to $2h/L_a$. The antenna output power can be characterised in the angular domain through the relation [34]:

$$p(u) = \int_{-1}^{1} a(u-u')s(u')du' \qquad 2.27$$

where a(u) is the antenna power pattern plotted in reverse and s(u) is the distribution of the speckle power with angle. Assuming the antenna dimension to be much larger than the wavelength, expression (2.27) can be formulated in the spatial frequency domain using the convolution theorem in the following way:

$$P(f) = A(f)S(f) \qquad 2.28$$

where P(f) is the antenna spatial power spectrum, S(f) is the spatial speckle power spectrum and A(f) can be shown to be equal to the complex conjugate of the autocorrelation function of the antenna illumination [34]. The spatial speckle power spectrum is essentially related to the field strength over the illuminated backscattering region that is expressed statistically through its spatial autocorrelation. The antenna is therefore capable of partially filtering the spatial speckle power spectrum. Physically this means that by modifying the antenna taper we can affect the amount of speckle received; indeed, the use of a wider beamwidth will increase the angular range over which the higher spatial frequencies can be averaged out [30]. This technique becomes of great interest with the use of active antenna array technology, where the potential of modifying the antenna pattern between transmit and receive mode allows an improved speckle

reduction without a large penalty in SNR and azimuth ambiguity suppression.

2.5 *SAR errors and orbit considerations*

In the analysis of a SAR sensor attitude errors play a fundamental role due to their direct impact on the SAR processing. In particular, the roll attitude error will mainly affect the gain control on the time receiving window. Typically techniques such as sensitivity time control (STC) and automatic gain control (AGC) are used to compensate the two-way antenna gain variation, the range attenuation difference across the swath and the pulse to pulse amplitude variation respectively. Lately, purely digital techniques such as block floating point quantization (BFPQ) and block adaptive quantization (BAQ) have demonstrated superior performances mainly due to the increased processing capability of digital technology [20].

Yaw and pitch attitude errors create uncertainties in the determination of the Doppler centroid. For a broadside SAR, the Doppler bandwidth should be symmetrically located with respect to the zero frequency but the presence of these errors will translate randomly the Doppler bandwidth, deteriorating both the SNR and the azimuth ambiguity ratio. Furthermore in the case of high carrier frequency SAR, the presence of yaw or pitch errors may cause a frequency shift of the Doppler centroid much larger than the total Doppler bandwidth with consequent uncertainty in the determination of the unambiguous Doppler centroid in the azimuth processing. The presence of yaw and pitch errors limits the use of the attitude control subsystem to correct the deterministic frequency shift introduced from the earth rotation. The next figure shows the variation of the observed Doppler frequency at the antenna boresight with respect to the orbit anomaly for the SEASAT SAR [26].

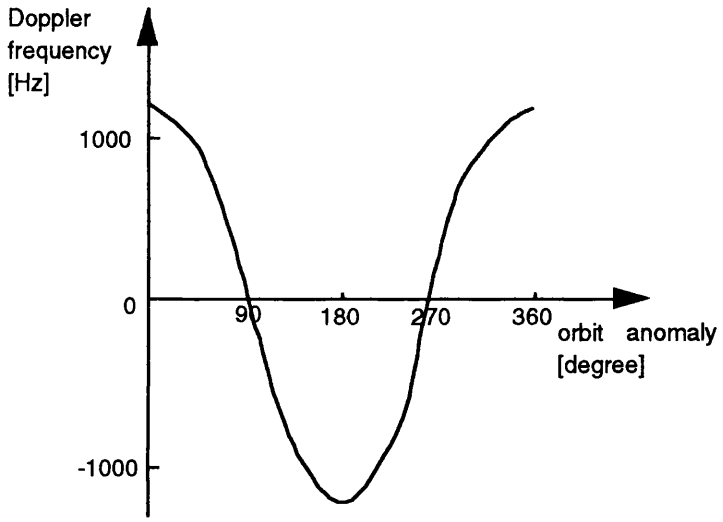

Fig.2.6 Observed Doppler frequency at the antenna boresight with respect to the orbit anomaly for the SEASAT SAR (after F.K.Li and W.T.K.Johnson, 1983)

In order to compensate this deterministic effect three main approaches can be used [3]: positioning the antenna main beam direction towards the zero Doppler line through the yaw angle attitude control, modulating the receiver local oscillator frequency to eliminate the induced Doppler shift caused by the earth rotation or using technique such as Clutterlock during processing [27].

For SAR applications, a circular orbit is considered very desirable due to the constant frequency characteristics along the orbit. In particular a fixed sensor altitude and orbital velocity will allow a faster processing of SAR images due to the minimisation of the inaccuracies related to the use of nominal orbital data. However, other important factors such as the potential of using fixed solar arrays, the relaxation of the spacecraft thermal control due to constant sun illumination direction and the solar array wings parallel to the orbit plane capable to minimise the drag effect will often constrain the SAR orbit towards down-dusk sun-synchronous orbits.

The change of altitude along the orbit is typically corrected with a corresponding PRF variation, where the change of orbital velocity (relevant for the case of highly elliptical orbit) will result in changes of Doppler centroid and FM rate. The former error is compensated with techniques similar to the earth rotation correction, where for the latter automatic techniques such as autofocus are often applied [27].

Typically the attitude errors will deteriorate the compression performance of the SAR processor. Mainly the azimuth compression mechanism will be affected due to the longer integration time involved. As an example, the effect of a quadratic amplitude error has been simulated. In figure 2.7, the bidimensional impulse response function of a typical SAR is shown. Both range and azimuth compressions are unweighted and the sinx/x behaviour clearly appears in the cardinal planes. In figure 2.8, a positive quadratic amplitude error is introduced in both range and azimuth compressions. The sidelobe level has increased; due to the presence of the error, the main lobe energy has spread into the sidelobe region. In the case of introduction of a Hamming weighting function, figures 2.9 and 2.10 show the SAR impulse response function without and with errors respectively. It appears evident that the presence of the weighting function allows a lower vulnerability to the quadratic errors at a price of a decreased spatial resolution.

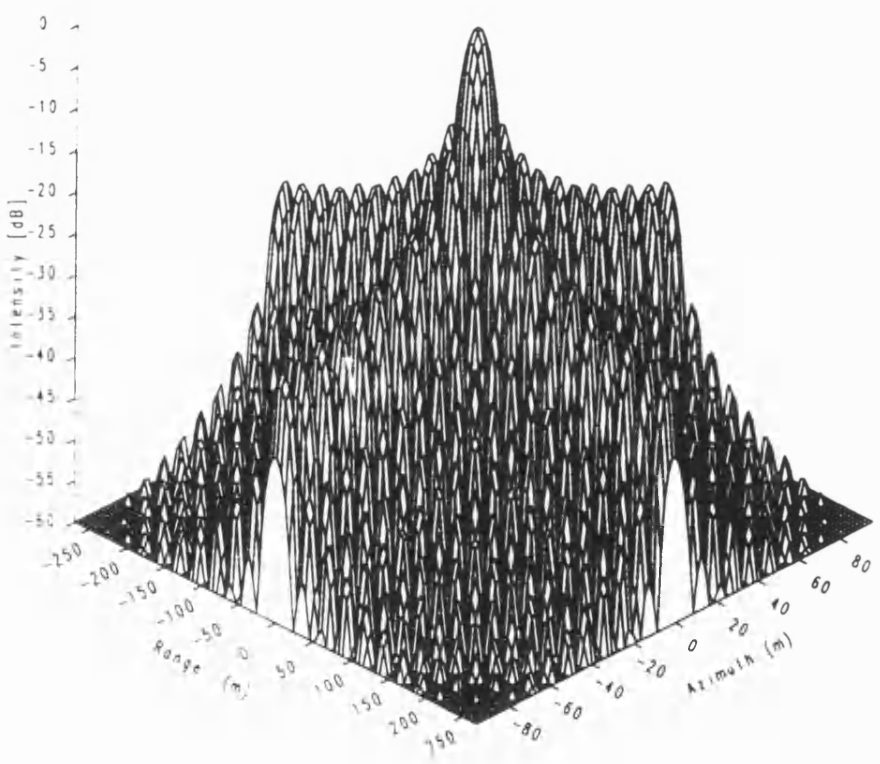

Fig.2.7 Unweighted error-free SAR impulse response function

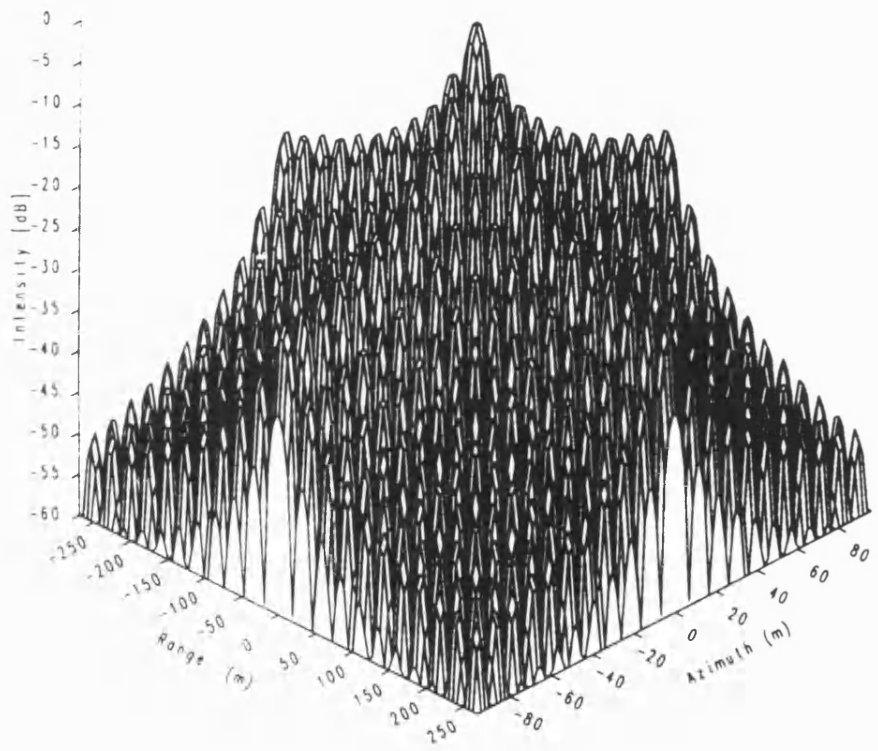

Fig.2.8 Unweighted SAR impulse response function with positive quadratic amplitude error

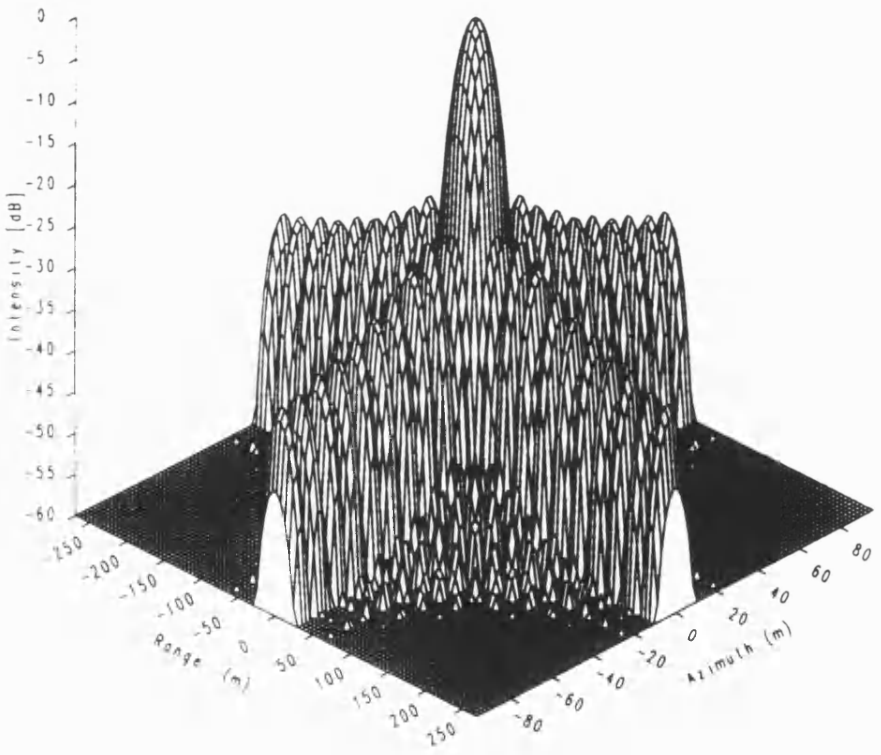

Fig.2.9 Hamming weighted error-free SAR impulse response function

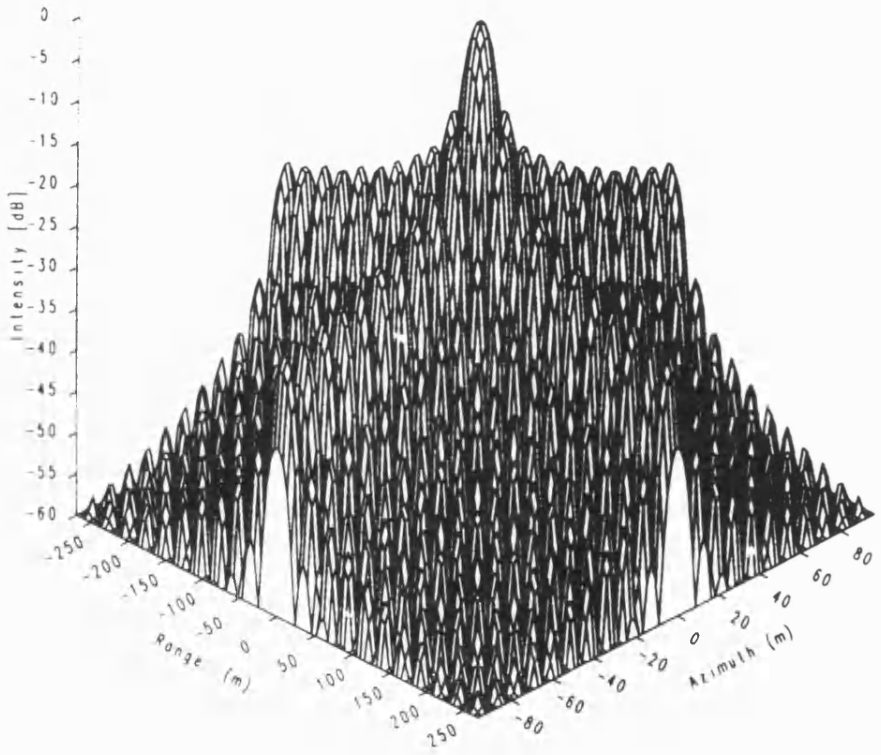

Fig.2.10 Hamming weighted SAR impulse response function with positive quadratic amplitude error

2.6 *SAR processing*

The SAR processor has to be able to implement the two dimensional matched filtering operation for each resolution cell of the image. The first SAR data were optically processed [35]. Despite the large amount of data that this technique was capable of processing in a small amount of time, dynamic range and calibration were serious drawbacks. Nowadays, the digital approach is the most popular way to process SAR data. A data flow describing the fundamental SAR processing operations is shown below:

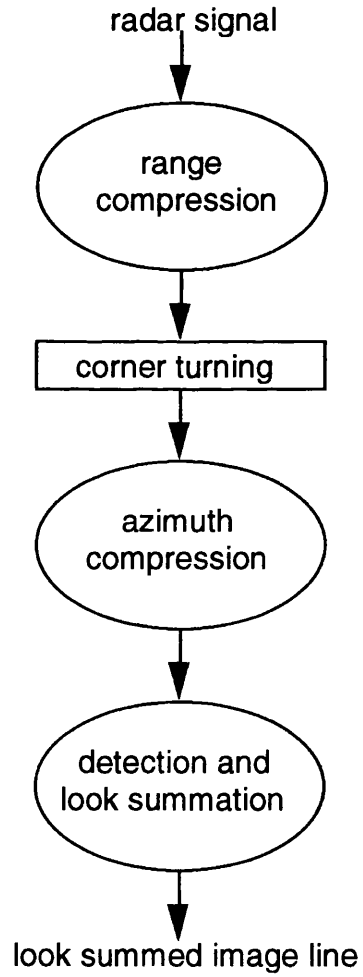

Fig.2.11 SAR image processing data flow diagram

After being range compressed, the received radar signal is stored in the corner turning memory array where each range line is placed in a corresponding row. The Doppler frequency history is automatically generated in each column where the azimuth compression is then applied. The compressed complex pixel is then detected and summed with other pixel corresponding to different looks. This flow of operation is performed on a pixel to pixel basis and for each new compressed range line, the corner turning array memory drops out the oldest memory row information. The necessary parameters for the compression algorithms, such as pulse replica, Doppler centroid, FM rate and number of looks are typically fixed before processing for the range compression, and dynamically estimated with the use of attitude and orbit data for the azimuth compression.

A problem of paramount importance in the processing of spaceborne SAR images is range migration. This is caused by the variation of the target range during the SAR azimuth integration. If this variation is larger than the range resolution, the SAR Doppler history of the illuminated target will not belong to a single column of the corner turning memory array and corrections will become necessary in order to properly perform the azimuth compression operation. Typically a larger part of the range migration error is due to attitude errors, orbit ellipticity and earth rotation [3]. Depending on the SAR processing implementation, different correction techniques for the range migration error are implemented.

The most well known processing schemes are: time-domain correlation, range-doppler, spectral analysis and two-dimensional fast correlation.

The time domain correlation method performs the matching process through the convolution operation in the time domain. Often the range compression is performed with the use of surface acoustic wave devices (SAW). Correction of range migration error can be

partially performed using interpolation techniques in the time domain. This mainly consists of a convolution of adjacent samples with a suitable spreading function. Alternative techniques can be implemented through the modification of the addressing strategy of the range samples from the corner turning memory array. The figure below shows a classical implementation of a convolution operation using a tapped delay line (transversal filter):

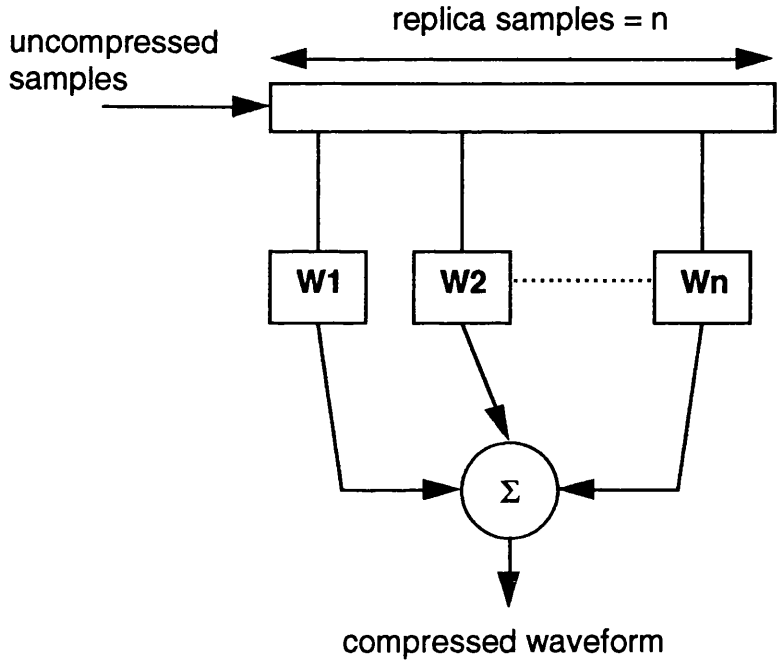

Fig.2.12 Convolution by transversal filter

The range-doppler method performs the compression operations in the frequency domain with the use of the Fast Fourier Transform (FFT). The main idea behind this concept is the analogy between the convolution in the time domain and the multiplication in the frequency domain. The following figure shows the flow diagram of a convolution performed in the frequency domain using FFT.

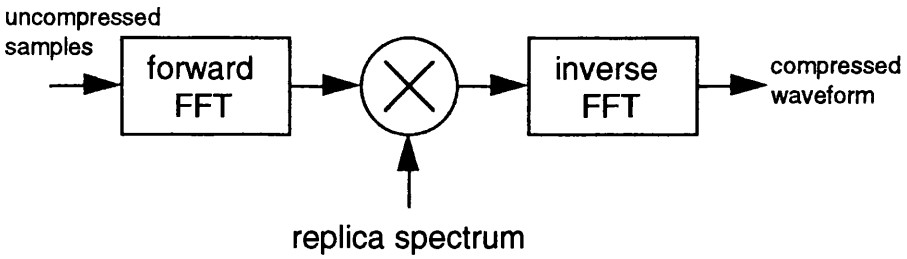

Fig.2.13 Convolution via spectral transform

The main advantages of this approach is the computational saving of the FFT with respect to standard time domain convolution techniques and the potential in applying simple range migration correction algorithms and looks separation in the frequency domain.

The spectral analysis method is based on the concept of using deramp processing in order to perform the compression operations. This approach relies on the fact that the product of a linear FM signal with a similar delayed waveform results in a constant frequency signal. The frequency and the time length of the deramped signal are related to the relative time delay and the duration of the overlap respectively. The range information is directly translated in the frequency domain and therefore a Fourier transform operation on the deramped signal will be capable of retrieving the desired product.

The main advantage of this technique is the capability of reducing the frequency bandwidth necessary for the required spatial resolution [36]. In the case of on-board range compression, this processing scheme is very interesting. Indeed not only the operational load is reduced because of the efficiency of the FFT algorithm, but also the sampling frequency of the ADC's is relaxed. The main drawback of such processing is the need of limiting the number of samples in the spatial window of interest in order to reduce the processed bandwidth. The following figure shows for the case of range

compression, the frequency history of a linear FM signal before and after multiplication with the properly delayed replica.

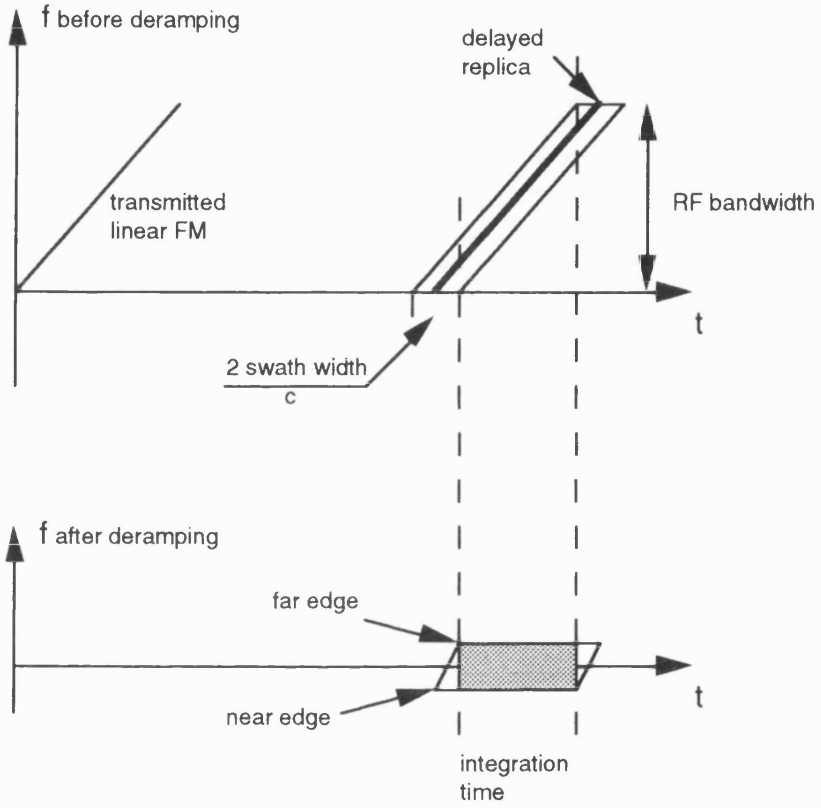

Fig.2.14 Frequency history of a linear FM signal before and after deramping processing

The two-dimensional fast correlation method considers both range and azimuth compressions simultaneously. It is conceptually very similar to the range-doppler method but the use of two-dimensional FFTs avoids the need of having a corner turning memory array. The most interesting feature of this approach is that range migration correction is not necessary since the replica is a two dimensional function and includes range migration as well. This technique for its bidimensional characteristics can be seen as the digital equivalent of SAR optical processing [37].

As an example, the computation complexity of the range-doppler SAR processing algorithm is computed. The following table summarises the relevant processing parameter for the ERS-1 SAR:

SAR PROCESSING PARAMETERS		
Parameter	**Symbol**	
Pulse Repetition Frequency	PRF	1700 Hz
Number of range cells	Nr	12500
Range replica size	Mr	700
Number of looks	L	4
Number of azimuth lines	Na	2048
Azimuth line overlap	Nov	400

TABLE 2

To perform the frequency domain range compression, efficient algorithms such as radix-2 FFT are used. The length of each FFT must be equal to or greater than the Nr + Mr-1. This avoids the overlapping due to end effects of the circular convolution. Instead of using a large FFT to cover all the range cells, it is convenient to use four FFTs of 4096 points which overlap each other by the range replica points. Since both the frequency domain replica and each FFT must have the same size, the replica is interpolated using a zero-padded approach in the time domain. The number of radix-2 butterflies for each FFT is $\frac{N_{FFT}}{2}\log_2 N_{FFT}$ where N_{FFT} is the FFT size.

To perform the product between the replica spectrum and the transformed range lines four N_{FFT} complex multiplications are necessary. The overall compression as to be performed at the PRF rate. As there are ten basic operations in a FFT butterfly computation (where an operation is a real addition or multiplication) and each complex multiplication requires six basic operations, the total number

of operations per second (OPS) for the range compression can be estimated according to the following table:

Range compression operations per second		
Forward FFT	$10 \times \frac{N_{FFT}}{2} \log_2 N_{FFT} \times 4 \times PRF$	1671 MOPS
Complex multiplication	$6 \times N_{FFT} \times 4 \times PRF$	167 MOPS
Inverse FFT	$10 \times \frac{N_{FFT}}{2} \log_2 N_{FFT} \times 4 \times PRF$	1671 MOPS
Total		3509 MOPS

TABLE 3

The frequency domain azimuth compression consists practically of the same type of operations as in range with some differences due to the presence of azimuth looks. The number of azimuth lines Na necessary for the FFT operation is chosen to be a power of two. In order to be capable to retrieve the total Doppler history of a point target located at the edge of the processed frame, it is necessary to allow an overlap of azimuth lines proportional to the azimuth integration time. The azimuth frame rate is therefore PRF/(Na-Nov).

The total number of FFTs necessary for the azimuth compression of a frame of dimension Nr x Na is equal to Nr and the number of complex multiplications necessary for the product with the replica spectrum are Nr x Na. The inverse FFT operation is applied separately on each look, therefore the number of FFTs required for the inverse Fourier transformation is equal to Nr x L with a size reduced by a factor 1/L. The total number of operations per second necessary for the azimuth compression of the range-doppler processing scheme is evaluated in Table 4.

Azimuth compression operations per second		
Forward FFT	$10\frac{N_a}{2}\log_2 N_a \times N_r \times \frac{PRF}{Na\text{-}Nov}$	1452 MOPS
Complex multiplication	$6 \times N_r \times N_a \times \frac{PRF}{N_a\text{-}N_{ov}}$	158 MOPS
Inverse FFT	$10\frac{N_a}{2}\log_2 \frac{N_a}{L} \times N_r \times \frac{PRF}{Na\text{-}Nov}$	1188 MOPS
Total		2798 MOPS

TABLE 4

The total number of operations per second for both range and azimuth compressions is 6307 MOPS. In this estimation, range migration, look registration, detection and look summation operations have not been considered since are typically a small fraction of the overall processing task. It is important to note that the overall number of operations per second is very high, real-time SAR processing is a very challenging task for existing digital technologies. In particular the fundamental point of on-board SAR processor is in achieving the necessary computational power within the size, weight and power constraints of the space platform.

In this chapter the basic principles of SAR theory have been presented. The radar equation, azimuth and range ambiguities, bidimensional matched filter theory and error analysis have been described. An alternative spatial frequency description of the Doppler imaging mechanism has been introduced in order to show the direct implication of the antenna taper on the speckle filtering. Different SAR processing techniques such as time-domain correlation, range-doppler, spectral-analysis and two-dimensional fast correlation have been reviewed in order to demonstrate their suitability for different sensor specifications.

3. SAR POLARIMETRY

3.1 *Introduction*

The first utilisation of the polarisation properties of electromagnetic waves dates back to the eighth century. At that time, the Vikings were using dichroic mineral to navigate the Baltic sea, avoiding the need for direct sunlight. In 1669, Erasmus Bartolinus published the first paper on polarisation effects, describing his experimental observations on the splitting of a light ray through a crystal. Due to the work of Christian Huygens in optics, the wave nature of light and its vectorial properties were recognised (1677).

At the beginning of the nineteenth century, the experimental discovery of Augustine Fresnel and Sir David Brewster demonstrated the transverse wave nature of light, and its reflection and transmission behaviour in the presence of a dielectric material. In 1832, Michael Faraday started the theoretical formulation of the electromagnetic field, then followed by the work of George Gabriel Stokes (1852) on the description of partially polarised light, and James Clerk Maxwell (1873) with his fundamental postulation of the displacement current, whose existence was later demonstrated by Heinrich Hertz (1886). Diffraction theory was the main subject of subsequent works by Helmholtz (1881), Lord Rayleigh (1881), Kirchhoff (1883) and Sommerfeld (1896). An important contribution to the understanding of polarisation was made by Henri Poincare' demonstrating that all possible polarisation states could be represented using the Riemann sphere (1892) [38,39].

In the last century, the utilisation of polarisation properties of electromagnetic waves has increased enormously due to the large interest devoted to the radar and laser fields and the associated technological developments. In order to properly address the subject of the thesis, a review of radar polarisation theory together with experimental data from a multipolarisation airborne SAR will be presented in this chapter.

3.2 *Polarisation theory*

The electric vector of a monochromatic plane wave travelling in the $+\hat{z}$ direction in a Cartesian coordinate system is:

$$\vec{E}(z,t) = |E_x| \cos(wt-kz+\phi_x)\vec{x} + |E_y| \cos(wt-kz+\phi_y)\vec{y} \qquad 3.1$$

for a fixed value of z, the vectorial sum of the orthogonal components as a function of time will describe an ellipse (the polarisation ellipse). Depending on the phase difference $\phi = \phi_y - \phi_x$ and the magnitude of the orthogonal components, the ellipse will degenerate into a straight line or a circle and the corresponding polarisation state will be linear or circular respectively.

A classical way to describe the polarisation state is through three geometric parameters of the corresponding polarisation ellipse: the orientation angle ε, which is the angle the major axis of the ellipse makes with the x axis, the ellipticity angle τ, which is the angle whose corresponding tangent is the ratio of the minor to the major axis and the ellipse size defined as $\sqrt{|E_x|^2+|E_y|^2}$. These geometrical parameters, as shown in figure 3.1, are capable of completely characterising the polarisation of the electromagnetic wave when the ellipse size and the phase difference ϕ are time independent. It is important to notice that, by definition, any monochromatic wave is always completely polarised.

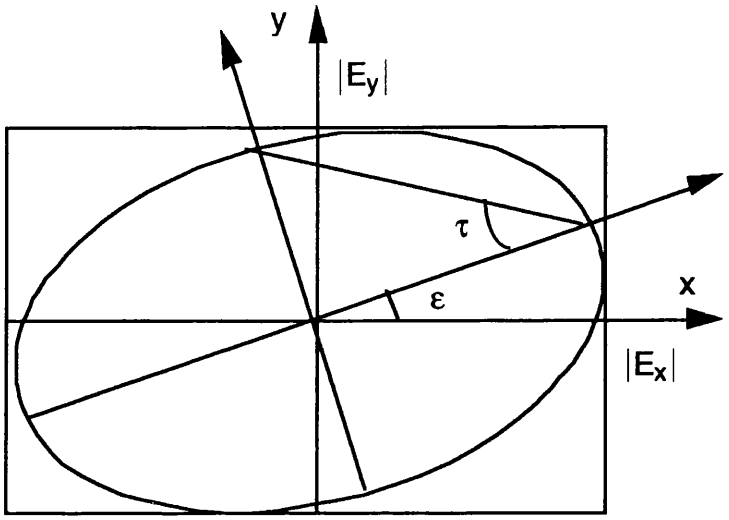

Fig.3.1 Polarisation ellipse

The orientation and ellipticity angles can be easily related to the magnitudes of the two orthogonal components $|E_x|$ and $|E_y|$ and their relative phase ϕ using the following formulas:

$$\tan(2\varepsilon) = \frac{2|E_x||E_y|\cos\phi}{|E_x|^2 - |E_y|^2} \qquad 3.2$$

$$\sin(2\tau) = -\frac{2|E_x||E_y|\sin\phi}{|E_x|^2 + |E_y|^2} \qquad 3.3$$

Alternatively, another way to represent polarisation is through the use of phasor notation:

$$\overrightarrow{E(z)} = \overrightarrow{E(0)}\exp(-jkz) \qquad 3.4$$

$$\vec{E}(z, t) = \mathrm{Re}\{\overrightarrow{E(z)}\ \exp(jwt)\} \qquad 3.5$$

where $\overrightarrow{E(0)}$ is represented through its orthogonal components in the following way :

$$\overrightarrow{E(0)} = \begin{bmatrix} |E_x| \exp(j\phi_x) \\ |E_y| \exp(j\phi_y) \end{bmatrix} \qquad 3.6$$

and using the polar coordinate reference system, the complex amplitude of the phasor $\overrightarrow{E(z)}$ becomes:

$$\overrightarrow{E(0)} = |\overrightarrow{E(0)}| \exp(j\phi_x) \begin{bmatrix} \cos(\gamma) \\ \sin(\gamma) \exp(j\phi) \end{bmatrix} \qquad 3.7$$

$$|\overrightarrow{E(0)}| = \sqrt{|E_x|^2 + |E_y|^2} \qquad 3.8$$

$$\gamma = \tan^{-1}\left(\frac{|E_y|}{|E_x|}\right) \qquad 3.9$$

The formulation of the polarisation state of the electromagnetic wave through the orthogonal components of the complex amplitude is also called the Jones vector of the wave [40].

In the previous description of the polarisation state, we have intrinsically assumed that $|E_x|$, $|E_y|$ and ϕ are time independent. Essentially this means that the wave is completely polarised, as is always the case for the electromagnetic field radiated from an antenna. However, in considering the backscattered signal from a natural surface, due to the presence of many elementary scattering points contributing to the reflected signal, a wider theory has to be introduced which can fully describe the physical phenomena. In this case, we use a new set of descriptors, the Stokes parameters, that

become necessary to describe the unpolarised component of the radiation.
For the case of a completely polarised wave the Stokes parameters are [41,42]:

$$S_0 = |E_x|^2 + |E_y|^2 \qquad 3.10$$

$$S_1 = |E_x|^2 - |E_y|^2 \qquad 3.11$$

$$S_2 = 2|E_x||E_y|\cos\phi \qquad 3.12$$

$$S_3 = -2|E_x||E_y|\sin\phi \qquad 3.13$$

of which only three are independent, and can be related in the following way:

$$S_0^2 = S_1^2 + S_2^2 + S_3^2 \qquad 3.14$$

S_0 is the total power density of the wave, S_1 is the power associated with the horizontal or vertical polarised intensity, S_2 is the power related to the linear polarised component orientated at ε = 45 or 135 degrees and S_3 is associated with the power of the circularly polarised component.

The Stokes parameters can be related to the orientation and ellipticity angles through the use of expressions 3.2 and 3.3, obtaining the following formulation:

$$S_1 = S_0 \cos 2\varepsilon \cos 2\tau \qquad 3.15$$

$$S_2 = S_0 \sin 2\varepsilon \cos 2\tau \qquad 3.16$$

$$S_3 = S_0 \sin 2\tau \qquad 3.17$$

As expected, S_3 will only depend on the ellipticity angle, indeed circular polarisation is independent of the orientation angle.

Considering a natural surface, the polarisation of the backscattered signal will be a function of time or spatial position and the reflected electromagnetic field will be partially polarised. Typically, since a natural surface is characterised as a random medium, it is necessary to introduce in the definition of the Stokes parameters an ensemble average operation. The resultant Stokes parameters are:

$$S_0 = \langle E_x E_x^* \rangle + \langle E_y E_y^* \rangle \qquad 3.18\ a$$

$$S_1 = \langle E_x E_x^* \rangle - \langle E_y E_y^* \rangle \qquad 3.18\ b$$

$$S_2 = \langle E_x E_y^* \rangle + \langle E_y E_x^* \rangle \qquad 3.18\ c$$

$$S_3 = -j\langle E_x E_y^* \rangle + j\langle E_y E_x^* \rangle \qquad 3.18\ d$$

For coherent sensors such as SARs, the received signal is strongly contaminated by a multiplicative noise called speckle due to phase modulation of the backscattered wave over the natural surface. The statistical variations of the reflected wave from a homogeneous surface are due to the random position of elementary scatterers inside the resolution cell.
This is clearly observed in a single look SAR image of a statistically uniform area, where the Fourier transform of the image carries more

information about the SAR than about the scene. For reducing the speckle noise, due to the lack of simultaneous samples of the random process, the ensemble average operator may be substituted by a spatial average. It is important to notice that for justifying this operation, the random surface is assumed ergodic and consequently stationary.

In the case of a partially polarised wave, the equality 3.14 is not satisfied; part of the wave energy will belong to the unpolarised component and consequently the following inequality will hold:

$$S_0^2 > S_1^2 + S_2^2 + S_3^2 \qquad 3.19$$

In the case of a completely unpolarised wave, the energy will be equally distributed between the two orthogonally polarised components, with a relative phase ϕ randomly fluctuating and its mean value equal to zero. Therefore any unpolarised radiation is generated from random variation of polarised states. In this case due to the statistical independence between $|E_x|$, $|E_y|$ and ϕ, only S_0 will have a value different from zero.

To quantitatively assess the amount of unpolarised component in an electromagnetic wave, the degree of polarisation P is introduced:

$$P = \frac{\sqrt{S_1^2 + S_2^2 + S_3^2}}{S_0} \qquad 3.20$$

and a partially polarised wave can be decomposed into unpolarised and polarised components, as expressed below.

$$\begin{bmatrix} S_0 \\ S_1 \\ S_2 \\ S_3 \end{bmatrix} = S_0 \begin{bmatrix} 1 - P \\ 0 \\ 0 \\ 0 \end{bmatrix} + S_0 \begin{bmatrix} P \\ P \cos 2\varepsilon \cos 2\tau \\ P \sin 2\varepsilon \cos 2\tau \\ P \sin 2\tau \end{bmatrix} \qquad 3.21$$

where ε and τ specify the geometric parameters for the ellipse of the polarised component.

An alternative way to represent the polarisation state is through the use of the Poincare' sphere as shown in the figure below. The Cartesian coordinates of each point on the sphere surface correspond to a set of three Stokes parameters S_1, S_2 and S_3 and consequently to a particular polarisation state. Due to the three-dimensional nature of the descriptor, the unpolarised component of the radiation can only be seen as a modulation of the sphere radius representing the energy of the polarised radiation [42].

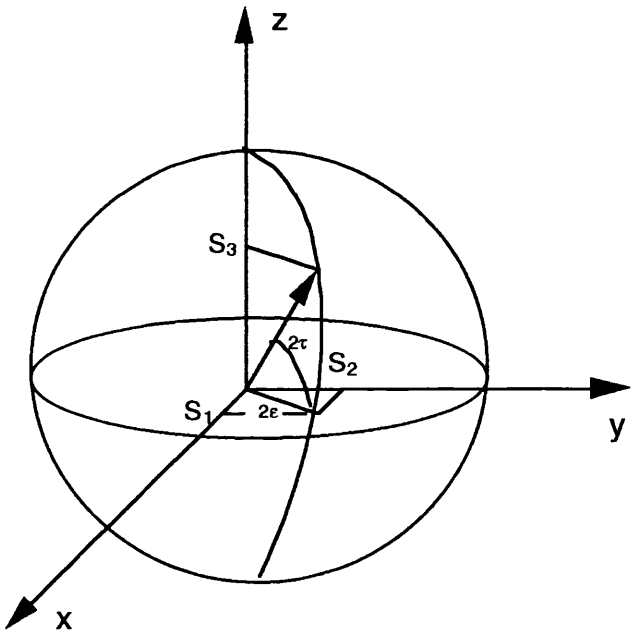

Fig.3.2 Poincare' sphere

When an electromagnetic wave illuminates a target, the backscattered radiation will not in general have the same polarisation as the incident wave and will not be fully polarised. Assuming we are observing the backscattered radiation for very short time and space

intervals such that the reflected field from any type of target can be considered fully polarised, the scatterer can be described using the so-called Scattering matrix [43]:

$$\begin{bmatrix} E_{x'} \\ E_{y'} \end{bmatrix}_{sc} = [S] \begin{bmatrix} E_x \\ E_y \end{bmatrix}_{tr} \qquad 3.22$$

where the matrix [S] is:

$$[S] = \frac{e^{jKr}}{kr} \begin{bmatrix} S_{x'x} & S_{x'y} \\ S_{y'x} & S_{y'y} \end{bmatrix} \qquad 3.23$$

the superscript ' identifies the receiving coordinate system, the subscripts sc and tr represent the scattered and transmitted Jones vectors respectively and r the distance between the target and the receiving antenna. The coordinate systems shown in the next figure will be adopted for the following analysis. It should be noticed that in the case of monostatic geometry, the transmit and receive coordinate systems will coincide(*).

In general, each element of the Scattering matrix will be complex, and neglecting an absolute phase term, seven independent parameters will be necessary to fully determine the Scattering matrix. In the monostatic case, under the assumption that reciprocity holds, the independent parameters will reduce to five. For virtually any natural target in the backscattering direction, even if it is anisotropic and inhomogeneous, the assumption of having equal cross-polarised scattering elements is valid [44].

(*) This coordinate system choice will be selected for any further analysis.

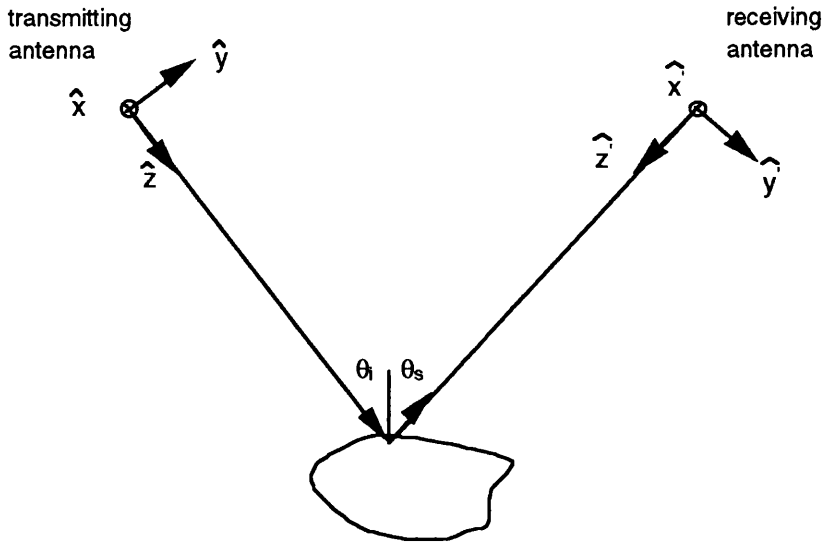

Fig.3.3 Scattering geometry and associated coordinate systems

An equivalent relation to 3.22 can be obtained between the Stokes parameters of the transmitted and reflected waves. In the coherent case, formulating equations 3.18 in matrix form:

$$\begin{bmatrix} S_0 \\ S_1 \\ S_2 \\ S_3 \end{bmatrix} = \begin{bmatrix} 1 & 1 & 0 & 0 \\ 1 & -1 & 0 & 0 \\ 0 & 0 & 1 & 1 \\ 0 & 0 & -j & j \end{bmatrix} \begin{bmatrix} E_x E_x^* \\ E_y E_y^* \\ E_x E_y^* \\ E_y E_x^* \end{bmatrix} \qquad 3.24$$

$$\vec{S} = [R]\vec{G} \qquad 3.25$$

where $\vec{S}$ and $\vec{G}$ are the four dimensional vectors whose components are the Stokes parameters and the electric field cross-products respectively. Using the Scattering matrix relations, it is possible to relate the cross-products of the transmitted and reflected scattered electric fields in the following way:

$$\begin{bmatrix} E_{x'}E_{x'}^{*} \\ E_{y'}E_{y'}^{*} \\ E_{x'}E_{y'}^{*} \\ E_{y'}E_{x'}^{*} \end{bmatrix} = \begin{bmatrix} S_{x'x}S_{x'x}^{*} & S_{x'y}S_{x'y}^{*} & S_{x'x}S_{x'y}^{*} & S_{x'y}S_{x'x}^{*} \\ S_{y'x}S_{y'x}^{*} & S_{y'y}S_{y'y}^{*} & S_{y'x}S_{y'y}^{*} & S_{y'y}S_{y'x}^{*} \\ S_{x'x}S_{y'x}^{*} & S_{x'y}S_{y'y}^{*} & S_{x'x}S_{y'y}^{*} & S_{x'y}S_{y'x}^{*} \\ S_{y'x}S_{x'x}^{*} & S_{y'y}S_{x'y}^{*} & S_{y'x}S_{x'y}^{*} & S_{y'y}S_{x'x}^{*} \end{bmatrix} \begin{bmatrix} E_xE_x^{*} \\ E_yE_y^{*} \\ E_xE_y^{*} \\ E_yE_x^{*} \end{bmatrix}$$

3.26

where the transformation matrix is denoted by [W] (note that for the sake of simplicity the spherical wave factor in the Scattering matrix definition has been omitted).

Combining the two previous relations:

$$[R]^{-1}\begin{bmatrix} S_0' \\ S_1' \\ S_2' \\ S_3' \end{bmatrix}_{sc} = [W][R]^{-1}\begin{bmatrix} S_0 \\ S_1 \\ S_2 \\ S_3 \end{bmatrix}_{tr} \qquad 3.27$$

Denoting the four dimensional vector formed by the Stokes parameter as the Stokes vector, in the monostatic case according to our choice of coordinate systems, the previous equality becomes:

$$\vec{S}_{sc} = [R][W][R]^{-1}\vec{S}_{tr} \qquad 3.28$$

$$\vec{S}_{sc} = [R][R]^{t}([R]^{t})^{-1}[W][R]^{-1}\vec{S}_{tr} = [R][R]^{t}[M][S]_{tr} \qquad 3.29$$

where the superscript t identifies the transpose operation. The matrix [M] is called the Stokes scattering operator [45,46,47].

Of the sixteen real elements of the Stokes scattering operator, in the coherent case only seven are independent and consequently there exist nine relations to determine the remaining matrix elements. In

the monostatic case, the Stokes scattering operator becomes symmetric and the relations will reduce to five. These relations, if valid, are necessary and sufficient conditions to associate the Stokes scattering operator to an equivalent Scattering matrix [42]. In SAR applications, the coherent nature of the Scattering matrix is rarely preserved, therefore nine independent parameters become necessary to fully describe the Stokes scattering operator.

It is important to note the difference between the Stokes scattering operator and the Mueller matrix defined below [43,46]:

$$[L] = [R][W][R]^{-1} \qquad 3.30$$

The Mueller matrix relates in a direct manner the transmitted and scattered Stokes vectors and therefore it is the exact analogue of the Scattering matrix for the Jones vectors. However, unlike the Stokes scattering operator in the monostatic case, it is never symmetrical. To reduce data volume, in polarimetric SAR applications, the Stokes scattering operator is often used.

The power received from a matched antenna when a plane wave is incident on it is [45]:

$$P_{rec} = K \left| \vec{E}_{rec} \cdot \vec{E}_{inc} \right|^2 \qquad 3.31$$

where K is a constant independent of the transmit and receive polarisations, $\vec{E}_{rec}$ is the electric far field vector radiated by the receiving antenna and $\vec{E}_{inc}$ is the electric field vector of a plane wave incident on the antenna.
The incident electric vector, due the chosen coordinate system, in the monostatic case is equivalent to the backscattered electric field and the previous equation utilising 3.25 and 3.26 becomes:

$$P_{rec} = K \left(\vec{E}_{rec} \cdot \vec{E}_{sc} \right) \cdot \left(\vec{E}_{rec} \cdot \vec{E}_{sc} \right)^{*} \qquad 3.32$$

$$P_{rec} = K \, \vec{G}_{rec}^{\,t} \, \vec{G}_{sc} \qquad 3.33$$

$$P_{rec} = K \, \vec{G}_{rec}^{\,t} \, [W] \, \vec{G}_{tr} \qquad 3.34$$

$$P_{rec} = K \, \vec{S}_{rec}^{\,t} \left([R]^{t} \right)^{-1} [W] \, [R]^{-1} \, \vec{S}_{tr} \qquad 3.35$$

$$P_{rec} = K \, \vec{S}_{rec}^{\,t} \, [M] \, \vec{S}_{tr} \qquad 3.36$$

The last equation demonstrates the relation between the Stokes scattering operator and the power absorbed by a matched load of an antenna in a monostatic configuration.

An alternative way to represent the received power is through the scattering cross section defined in the following way [42]:

$$\sigma_{r,t} = \lim_{r \to \infty} (4\pi r^2) \left(\frac{P_{rec\,r,t}}{P_{tr}} \right) \qquad 3.37$$

where $P_{rec\,r,t}$ is the power received in the presence of a transmit t and receive r polarisations when P_{tr} is the power transmitted, and the factor $4\pi r^2$ together with the limit assure the far field condition and the necessary physical dimension. Combining the two previous equations and expressing the Stokes parameters in terms of the orientation and ellipticity angles, the scattering cross section can be written in the following way:

$$\sigma(\varepsilon_t, \tau_t, \varepsilon_r, \tau_r) = K_0 \begin{bmatrix} 1 \\ \cos 2\varepsilon_r \cos 2\tau_r \\ \sin 2\varepsilon_r \cos 2\tau_r \\ \sin 2\tau_r \end{bmatrix}^t [M] \begin{bmatrix} 1 \\ \cos 2\varepsilon_t \cos 2\tau_t \\ \sin 2\varepsilon_t \cos 2\tau_t \\ \sin 2\tau_t \end{bmatrix}$$

3.38

where K_0 is a normalising factor which is polarisation independent. The previous expression defines the polarisation signature of the target.

In SAR applications, in order to reduce speckle noise, the power of adjacent pixels may be combined to reduce the statistical variation of the resultant signal. If the transmit and receive polarisations are considered constant during the averaging operation, then summing power samples will simply reflect in summing the Stokes scattering operators. This is equivalent to if the backscattered field was due to several scatterers radiating incoherently [45].

The incoherent nature of the averaging operation justifies the use of second order descriptors for multipolarisation SAR. Indeed the Scattering matrix by definition is only capable of characterising coherent scattering phenomena. The averaging operation will destroy the relation between the Stokes scattering operator (or any second order descriptor) and the Scattering matrix unless the distributed target of interest presents highly homogeneous scattering properties.

3.3 *Scattering theory*

Most of the existing scattering theories are devoted to scalar problems. This is due to the complexity introduced by the vectorial description of the phenomena, together with the historical motivation that acoustics has been the main subject where scattering theories have found applications. Lately, essentially due to Radar Polarimetry and communication satellite antennas (frequency re-use), interest in vectorial scattering theories has strongly increased [48].

The two classical approaches used in electromagnetic theory for the analysis of the backscattered radiation from statistical rough surface are the physical (PO) and geometrical (GO) optics approximations [48,49]. In the physical optics approximation, the induced surface current is computed assuming the reflecting surface locally flat as shown in figure 1.1. For a perfectly conducting medium, the induced surface current capable to satisfy the boundary condition is equal to:

$$\vec{J} = 2\,\vec{n} \times \vec{H_i} \qquad 3.39$$

where $\vec{n}$ is the local normal to the surface and $\vec{H_i}$ is the incident magnetic field. From this approximation, in the presence of a perfect conductor the backscattered radiation will not show any depolarisation when the incident field is linearly polarised. Expanding the physical optics approximation and considering the dyadic Green function of each patch into which the reflecting surface is subdivided, the previous expression becomes [48]:

$$\vec{J} = 2\,\vec{n} \times \vec{H_i} + e\,(\,\vec{u}\,(\vec{n} \times \vec{H_i}\,)_u - \vec{v}\,(\vec{n} \times \vec{H_i}\,)_v\,) \qquad 3.40$$

where $\vec{u}$ and $\vec{v}$ are the unit principal vectors of the patch and

$$e = r\,\frac{(\,R_u - R_v\,)}{4} \qquad 3.41$$

where r is the patch radius and R_u and R_v are the principal values of the curvature in the $\vec{u}$ and $\vec{v}$ directions. In this extended PO formulation, the backscattered field from a perfect conductor will exhibit depolarisation unless the patch of interest presents equal principal curvatures or if the local surface coordinate and the incident field coordinate are aligned.

The geometrical optics approximation (GO) usually applies in the presence of a rough surface (large root mean square height with respect to the radar wavelength) as shown in figure 1.1. The backscattered electromagnetic field is computed applying the stationary phase method for solving the integral equation relating the induced surface current to the backscattered electromagnetic field. The main contribution to the scattered field is in the same direction of the ray satisfying locally the first Snell law.

Both PO and GO in the presence of a highly conductive surface (unless extended PO is considered) do not predict any depolarisation and do not show any difference in the scattering behaviour between the two copolarised scattering coefficients.

For the determination of the backscattered electromagnetic field from a statistical smooth surface, as shown in figure 1.1, the small perturbation method (SMP) or Bragg scattering model, is often considered [7,16,44,48]. Typically, the surface is described as an expansion of several terms forced to match the boundary conditions. Depending on the number of terms considered in the model, a set of equations is generated from which the unknown backscattered electromagnetic field is determined. The boundary condition used in this formulation is also called the Bragg resonance condition and is formulated in the following way:

$$\Lambda = n\,\lambda/2 \sin\theta, \quad n = 1,2,... \qquad 3.42$$

where Λ is the spatial wavelength of the surface component corresponding to the n term and θ is the incidence angle.

The small perturbation method, due to its resonant nature, is more sensitive to smaller scale roughness than the PO and GO approximations. The first order appoximation (n=1) generates the strongest backscattering contribution but does not predict any depolarisation. In order to obtain any depolarisation effect with SMP, it is necessary to extend the approximation to second or higher orders.

The first order copolarised backscattering cross section is expressed in the following way [7]:

$$\sigma_{HH,VV} = 8\, K^4 h^2 \cos^4(\theta) \,|\alpha_{HH,VV}|^2\, W(2k\sin(\theta)) \qquad 3.43$$

where K is the wave number, h is the surface root mean square height, W is the Fourier transform of the surface correlation function (i.e. the surface roughness spectrum) and $\alpha_{HH,VV}$ is a factor depending on the polarisations of the transmitted and reflected waves according to the following expressions:

$$\alpha_{HH} = \frac{1-\varepsilon}{\left[\cos(\theta) + \sqrt{\varepsilon - \sin^2(\theta)}\,\right]^2} \qquad 3.44$$

$$\alpha_{VV} = (\varepsilon-1)\,\frac{\sin^2(\theta) - \varepsilon\,(1+\sin^2(\theta))}{\left[\varepsilon\cos(\theta) + \sqrt{\varepsilon - \sin^2(\theta)}\,\right]^2} \qquad 3.45$$

where ε is the surface dielectric constant.

The Bragg scattering model does predict a difference in the two copolarised backscattering cross sections as is shown in figure 3.4, where the amplitudes of α_{HH} and α_{VV} are plotted with respect to the

incidence angle, for a value of the surface dielectric constant equal to 73.7 - i69.2 corresponding to sea water at L band for a surface temperature of 15° C [16].

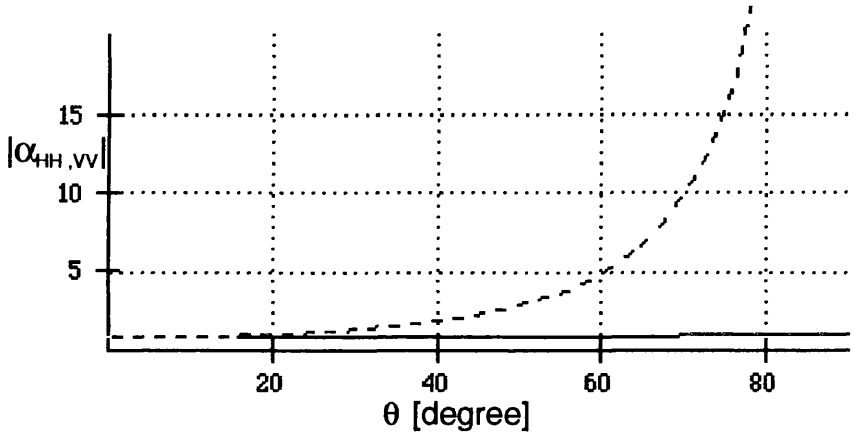

Fig.3.4 Amplitudes of Bragg factors α_{HH} (normal line) and α_{VV} (dashed line) for $\varepsilon = 73.7 - i69.2$

The above figure shows the typical behaviour of Bragg factors versus incidence angle, demonstrating the need for using vertical polarisation for scattering phenomena where the small perturbation method applies.

An extension of the Bragg scattering model is the so-called two scale model where the small scale roughness (typically capillary and small gravity waves in sea surface modelling at microwave frequencies) is modelled using SMP and the large scale roughness (surface with correlation length larger than the radar wavelength) is modelled using a PO derivation. The main advantage of this approach is that it is suitable for both small incidence angles with specular type of backscattering and large incidence angles together with Bragg type of backscattering.

In the presence of volume scattering, techniques such as radiative transfer and statistical wave theories have found wide applications.

The first of these is an incoherent theory describing the backscattering phenomena as a balance of scattered, radiated and absorbed energies. The second approach characterises the scattering volume as a continuous media with perturbed electrical properties. It is often applied in dense medium where the coherent contribution cannot be neglected [48,50,51].

In order to verify the validity of the previously described scattering models, it is necessary to compute the polarisation signature of some canonical targets and compare them with experimental polarisation signatures from airborne polarimetric SAR.

The Scattering matrix for a flat dielectric surface at normal incidence, according to the coordinate system of figure 3.3 is:

$$[S] = C\begin{bmatrix} 1 & 0 \\ 0 & 1 \end{bmatrix} \qquad 3.46$$

where C is the Fresnel reflection coefficient at normal incidence. The matrix [W] in 3.26 becomes:

$$[W] = c^2\begin{bmatrix} 1 & 0 & 0 & 0 \\ 0 & 1 & 0 & 0 \\ 0 & 0 & 1 & 0 \\ 0 & 0 & 0 & 1 \end{bmatrix} \qquad 3.47$$

and consequently the Stokes scattering operator from 3.29 is:

$$[M] = ([R]^t)^{-1}[W][R]^{-1} = \frac{c^2}{2}\begin{bmatrix} 1 & 0 & 0 & 0 \\ 0 & 1 & 0 & 0 \\ 0 & 0 & 1 & 0 \\ 0 & 0 & 0 & -1 \end{bmatrix} \qquad 3.48$$

As predicted from the previous analysis, the matrix is symmetrical and the main diagonal also satisfies the trace rule:

$$M_{11} = M_{22} + M_{33} + M_{44} \qquad 3.49$$

It is important to compute the scattering cross section using expression 3.38. For the sake of clarity, the polarisation signature is often computed with equal polarisation states (copolarised signature) or with orthogonal polarisation states (crosspolarised signature) of the transmit and receive antennas. The resulting copolarised polarisation signature is:

$$\sigma(\varepsilon, \tau) = K_0 \frac{c^2}{2} \begin{bmatrix} 1 \\ \cos 2\varepsilon \cos 2\tau \\ \sin 2\varepsilon \cos 2\tau \\ \sin 2\tau \end{bmatrix}^t \begin{bmatrix} 1 & 0 & 0 & 0 \\ 0 & 1 & 0 & 0 \\ 0 & 0 & 1 & 0 \\ 0 & 0 & 0 & -1 \end{bmatrix} \begin{bmatrix} 1 \\ \cos 2\varepsilon \cos 2\tau \\ \sin 2\varepsilon \cos 2\tau \\ \sin 2\tau \end{bmatrix}$$

3.50

$$\sigma(\varepsilon,\tau) = K_0 c^2 \cos^2(2\tau) \qquad 3.51$$

In this case the backscattered received power does not depend on the orientation angle. The copolarised signature will be maximised for any linear polarisation and will be zero for any circular polarisation. In the crosspolarised signature, the largest backscattered energy will be obtained for any circular polarisation where the linear polarisation will not generate any crosspolarised backscattered return.

In practice when the SAR is imaging natural surfaces, this scattering model applies very rarely because of the sensor slant geometry (it is important to notice that a trihedral corner reflector is actually described with a similar Scattering matrix to 3.46). Exceptions might result in the presence of ambiguous nadir returns or for a rough surface where the scattering is dominated by reflections from facets orthogonal to the slant range direction [52].

It is interesting to note the similarity of this signature with that of an isotropic sphere model, which explains why circular polarised antennas are often used for suppressing rain clutter.
In the case of Bragg scattering, the first order approximation will predict a Scattering matrix equal to:

$$[S] = \begin{bmatrix} S_{HH} & 0 \\ 0 & S_{VV} \end{bmatrix} \qquad 3.52$$

where S_{HH} and S_{VV} are linearly related to the Bragg factors α_{HH} and α_{VV} respectively. Similarly to the specular reflection case, the Stokes scattering operator can be computed. It is important to notice that with respect to the previous example, the first order Bragg scattering model will present a major difference because of the dependence of the Bragg factors on incidence angle. Indeed for increasing incidence angles, more energy will be backscattered in the vertically polarised channel than in the horizontal one.

In order to compare these theories with real SAR images, data collected during 1985 with the JPL L-band airborne multipolarisation SAR (NASA CV990) have been processed [47,53]. The NASA CV990 aircraft was flying at an altitude of 11 kilometres with near and far range incidence angles of 25 and 55 degrees respectively. The SAR one look spatial resolution is 7.5 metres in slant range and 3 metres in azimuth. The data are arranged in a four-look Stokes scattering operator format with a pixel spacing of 11 metres in both ground range and azimuth. The main sensor parameters are summarised in Table 5 [54].
Three copolarised and crosspolarised signatures of the sea, taken from equal sized pixel subsets of approximately 40 resolution elements at three different range incidence angles, have been synthesised. The need to minimise signal statistical variations together with preserving fundamental scattering properties has driven the choice of the subset size [55].

NASA CV990 SAR SPECIFICATIONS	
wavelength	24.5 cm
RF bandwidth	18 MHz
pulse length	4.9 μs
peak power	5 kW
pulse repetition rate	1 per 34 cm along-track
slant range resolution	7.5 metres
azimuth resolution	3 metres
incidence angles	25 - 55 degrees
aircraft velocity	200 - 300 m/s
aircraft operating altitude	11 km

TABLE 5

In figures 3.5 and 3.6, for an incidence angle of 25 degrees, the signatures show a strong specular reflection component, the vertical polarisation (ε = 90 degree, τ=0 degree) in the copolar signature 3.5 is slightly larger than the horizontal polarisation (ε = 0,180 , τ=0 degree) and in the crosspolarised signature 3.6, the low return in the case of orthogonally linearly polarised transmit and receive antenna is evident. In figures 3.7 and 3.8, the Bragg scattering mechanism starts to have a predominant effect, and the vertical polarisation in the copolar signature is more pronounced than in the previous case. Finally, figures 3.9 and 3.10 shows very clearly a predominant Bragg scattering mechanism. The two nulls in the crosspolarised signatures change depth and positions for different incident angle. This due to the variations of Bragg factors for different range incidence angles.

From this example, it appears evident that multipolarisation SAR allows the validation of the classical scattering model that consider dominant specular reflection for small incidence angles and Bragg scattering for large incidence angles. Note the that small perturbation method applies for surfaces where the root mean square height is

much less than the SAR carrier wavelength, therefore the sea surface contribution is due to height variations of the order of few centimetres.(see Fig.1.1)

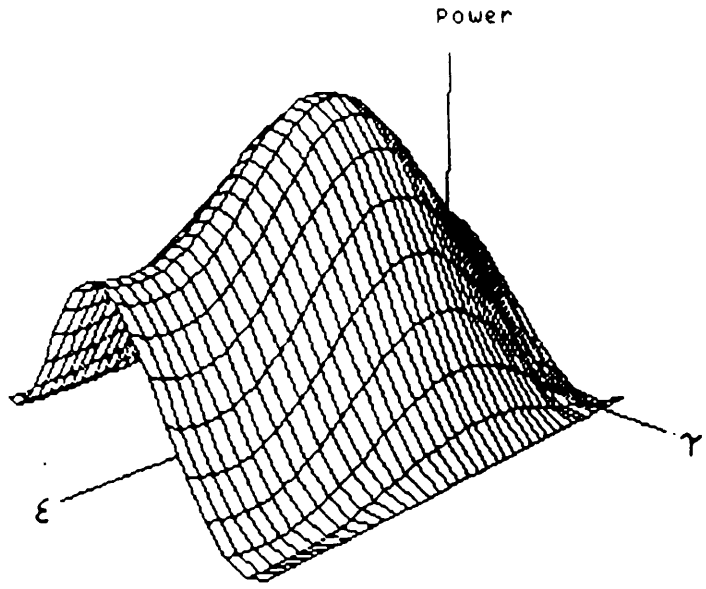

Fig.3.5 Copolar signature of the sea at 25 degree incidence angle

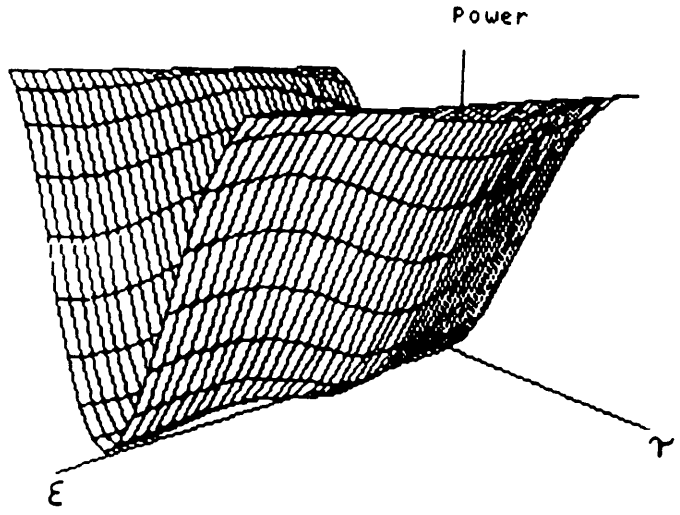

Fig.3.6 Crosspolar signature of the sea at 25 degree incidence angle

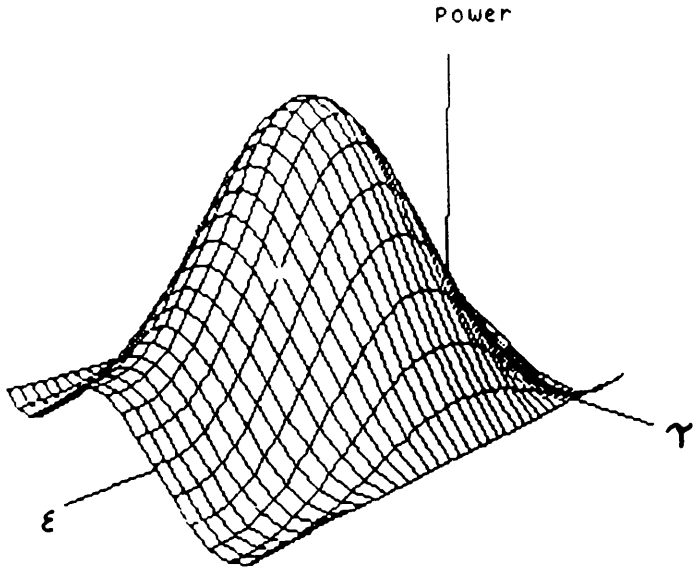

Fig.3.7 Copolar signature of the sea at 40 degree incidence angle

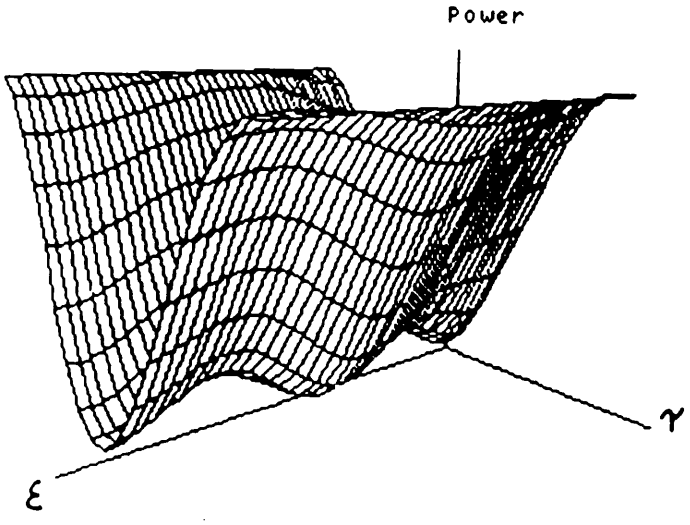

Fig.3.8 Crosspolar signature of the sea at 40 degree incidence angle

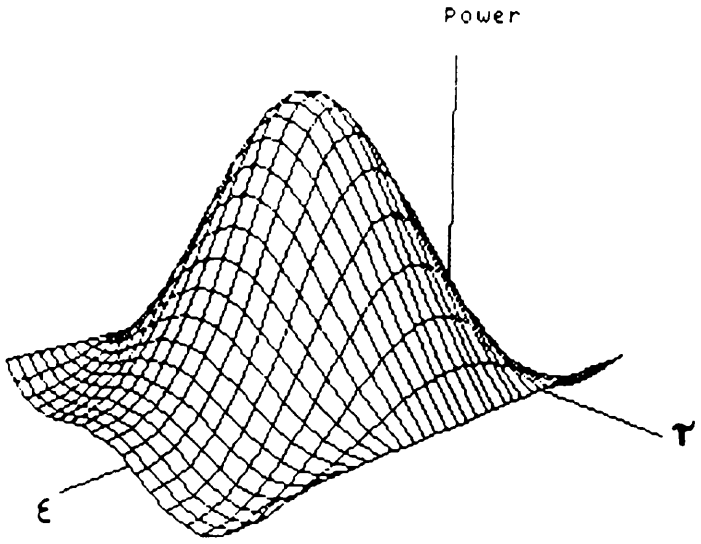

Fig.3.9 Copolar signature of the sea at 55 degree incidence angle

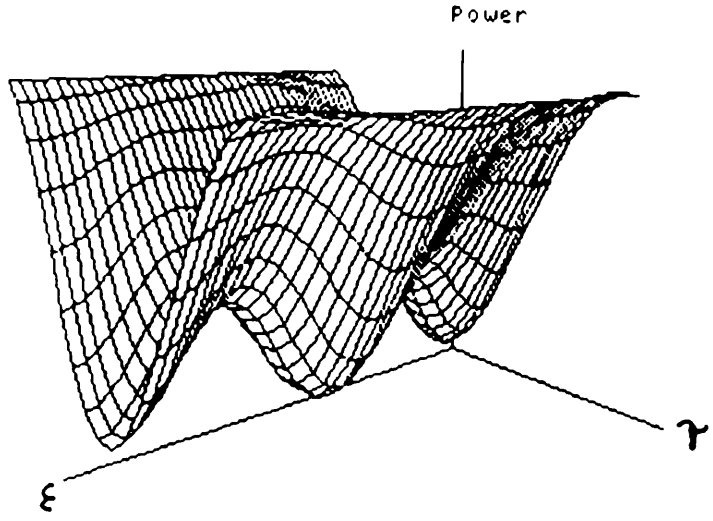

Fig.3.10 Crosspolar signature of the sea at 55 degree incidence angle

Another important type of target to analyse is the dihedral corner reflector [42]. Due to the double bounce nature of the scattering mechanism involved, the Scattering matrix can be expressed in the following way:

$$[S] = \begin{bmatrix} -R_h(\theta_1)R_h(\theta_2) & 0 \\ 0 & R_v(\theta_1)R_v(\theta_2) \end{bmatrix} \qquad 3.53$$

where R_h and R_v are the Fresnel reflection coefficients for horizontal and vertical polarisations respectively, and θ_1 , θ_2 are shown in the figure below: (where $\sigma_1 = 90^0 - \theta_2$)

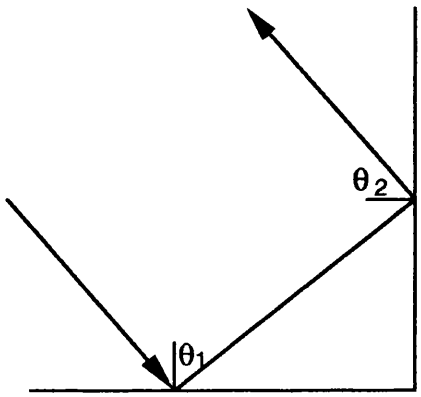

Fig.3.11 Dihedral corner reflector geometry

The associated Stokes scattering operator for a perfectly conducting dihedral corner reflector of area A illuminated along its boresight becomes:

$$[M] = \frac{k^2 A^2}{32\pi^2} \begin{bmatrix} 1 & 0 & 0 & 0 \\ 0 & 1 & 0 & 0 \\ 0 & 0 & -1 & 0 \\ 0 & 0 & 0 & 1 \end{bmatrix} \qquad 3.54$$

Figures 3.12 and 3.13 show an example of the copolar and crosspolar signatures of a conducting dihedral corner reflector.

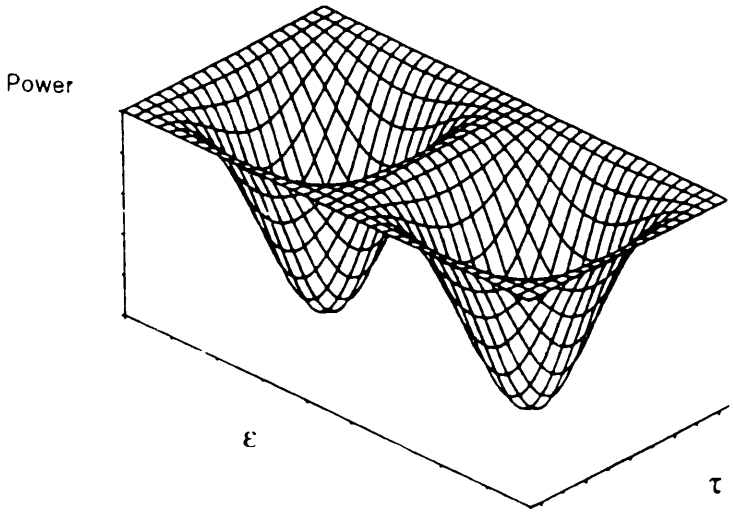

Fig.3.12 Copolar signature of a conducting dihedral corner reflector

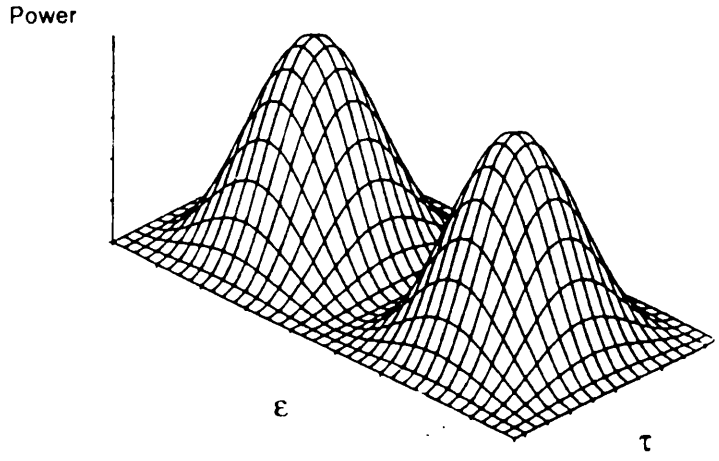

Fig.3.13 Crosspolar signature of a conducting dihedral corner reflector

From the JPL airborne SAR data, we have synthesised the polarisation signatures of an urban area of approximately 40 resolution elements at 35 degrees incidence angle (figures 3.14 and 3.15). A similarity is evident with the previous signatures of an ideal dihedral corner reflector. The urban area of interest is characterised by streets normal to the radar illumination, resulting in a large component of dihedral-type scattering behaviour. The main difference with the ideal case is the presence of a large pedestal in both the copolar and crosspolar signatures of the urban area. The pedestal is strongly related to the amount of unpolarised radiation. The incoherent summation of multiple scattering phenomena is the main source of the unpolarised component. The incoherent averaging process, necessary to filter signal statistical variations, generates a resulting signature composed by Stokes scattering operators related to different resolution cells. Depending on the amount of spatial homogeneity in the scattering behaviour of the selected area, the polarisation signature will generate a larger or smaller pedestal.

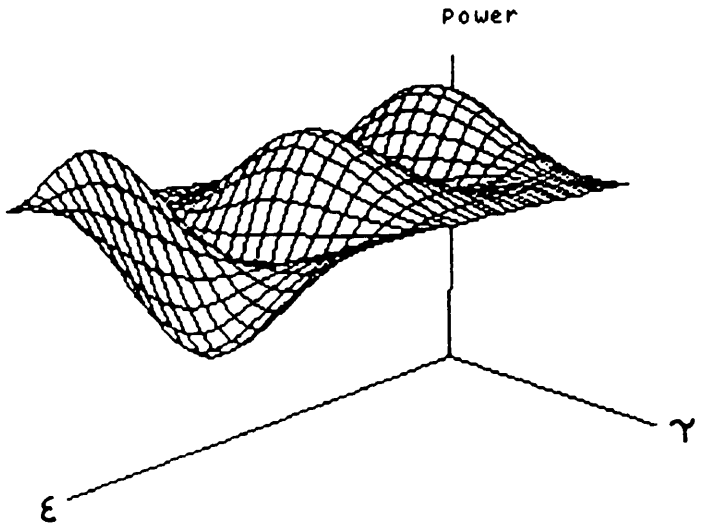

Fig.3.14 Copolar signature of an urban area at 35 degrees incidence angle

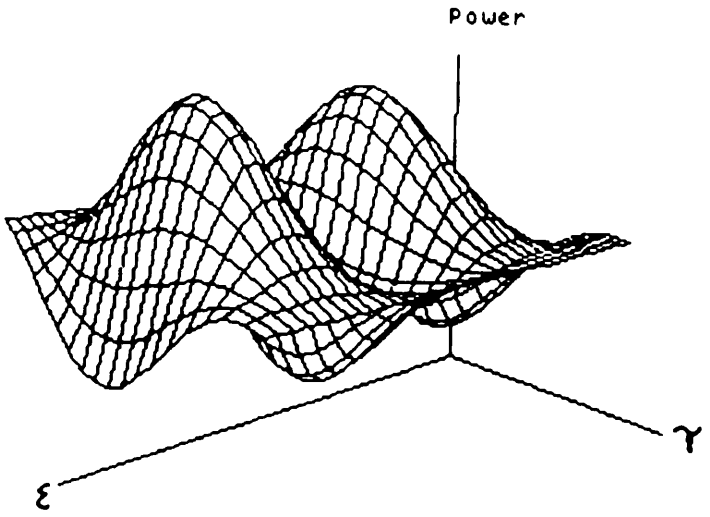

Fig.3.15 Crosspolar signature of an urban area at 35 degrees incidence angle

To emphasise this aspect it is useful to analyse a vegetation area. Typically the scattering model to describe the electromagnetic interaction mechanism includes volume scattering, surface scattering and their mutual interaction [16]. It is often quite difficult to identify a dominant scattering phenomenon, and it strongly depends on the local characteristics of the imaged area and the main sensor parameters such as polarisation, frequency and incidence angle.

In figures 3.16 and 3.17, are shown the copolarised and crosspolarised signatures of a vegetation area of approximately 40 resolution cells synthesised from the JPL airborne SAR data at 40 degrees incidence angle. The imaged area generates a large unpolarised component as can be seen from the volume of the pedestal under the signature surface. With respect to the sea

signatures, they show a very poor polarisation discrimination capability.

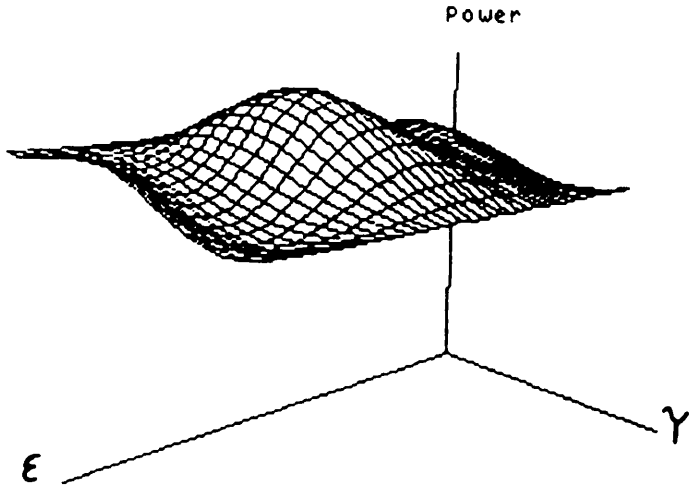

Fig.3.16 Copolarised signature of a vegetation area at 40 degrees incidence angle

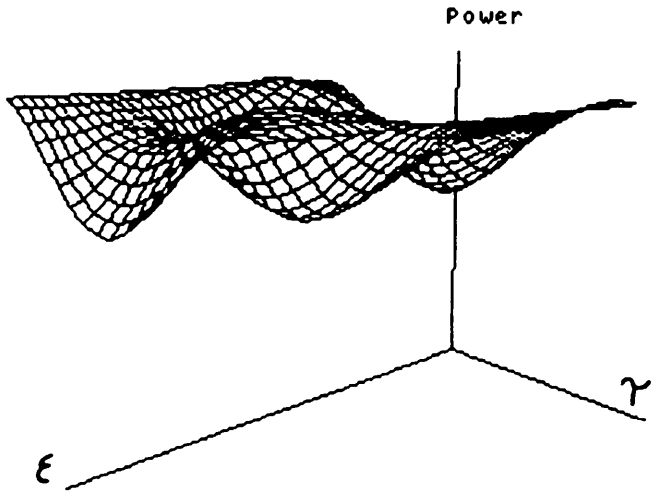

Fig.3.17 Crosspolarised signature of a vegetation area at 40 degree incidence angle

Typically all the multibounce scattering mechanisms such as the volume scattering from the canopy foliage towards the sensor and the ground, reflections from trunks, branches and underneath surfaces will contribute to the unpolarised radiation component.

The pedestal height carries very valuable information about the target and the instrument itself. Several scattering theories such as PO and GO will produce the same type of Scattering matrix with equal elements on the principal diagonal. The only difference will appear in a constant of proportionality that will directly affect the pedestal height of the polarisation signature. Therefore different scattering mechanisms can produce equal shape of the signature surface but raised on different pedestals(*)

The unpolarised component will also depend on the amount of thermal noise injected in the signal, indeed Gaussian thermal noise is itself an unpolarised signal.

It is important to estimate thermal noise not only to determine the unbiased pedestal height, but mainly to perform the overall sensor calibration. The effect of additive noise on a SAR pixel is simulated considering the following model: the noise contribution is associated to a vector of constant amplitude A and uniformly distributed phase θ modulating the resultant vector as illustrated in figure 3.18. Assuming the true vector of unitary amplitude, the power and phase error statistical properties are computed [56]:

$$\text{Power, error} = 1+A^2+2A\cos\theta \qquad 3.55$$

$$\text{mean} = 1 + A^2 \qquad 3.56$$

$$\text{standard deviation} = \sqrt{2}\,A \qquad 3.57$$

(*) According to PO and GO there is no pedestal, but in practice one is observed.

$$\text{Phase, error} = \tan^{-1}\left[\frac{A\sin\theta}{1+A\cos\theta}\right] \qquad 3.58$$

$$\text{mean} = 0 \qquad 3.59$$

$$\text{standard deviation} \approx \sqrt{\frac{A^2}{2}+\frac{A^4}{8}+\cdots} \qquad 3.60$$

In figures 3.19, 3.20, 3.21 both power and phase errors are plotted.

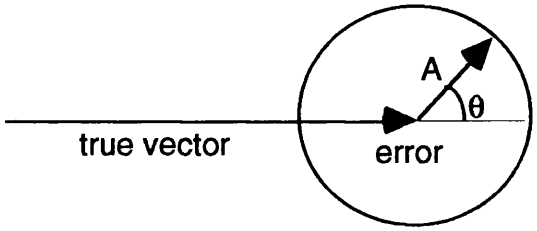

Fig.3.18 Noise vector model

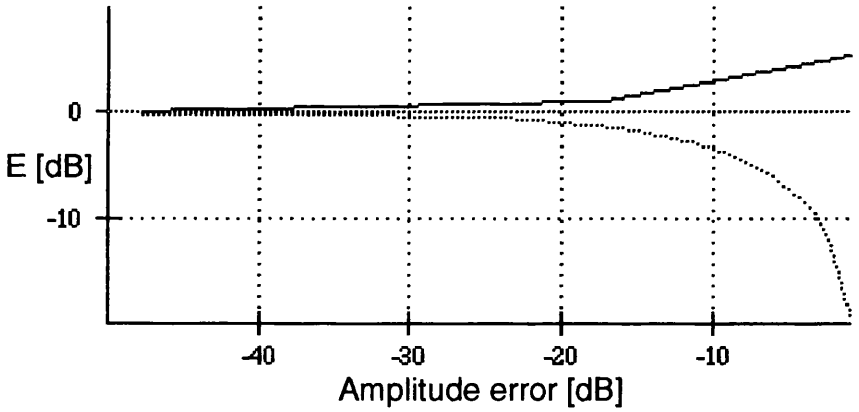

Fig.3.19 Peak power error

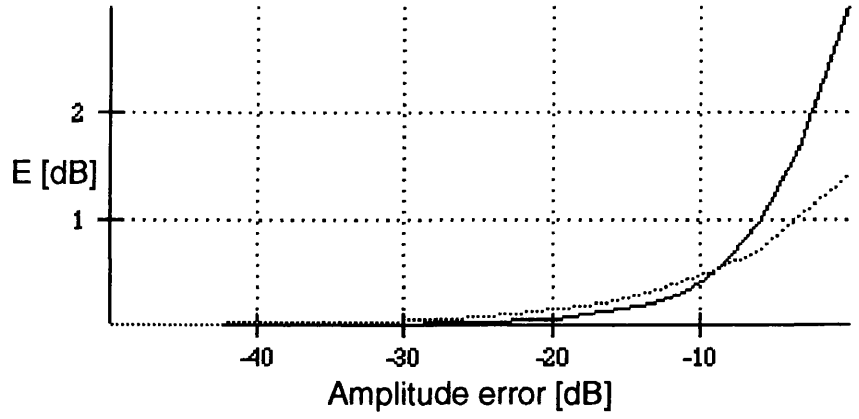

Fig.3.20 Mean (normal line) and standard deviation (dotted line) power errors

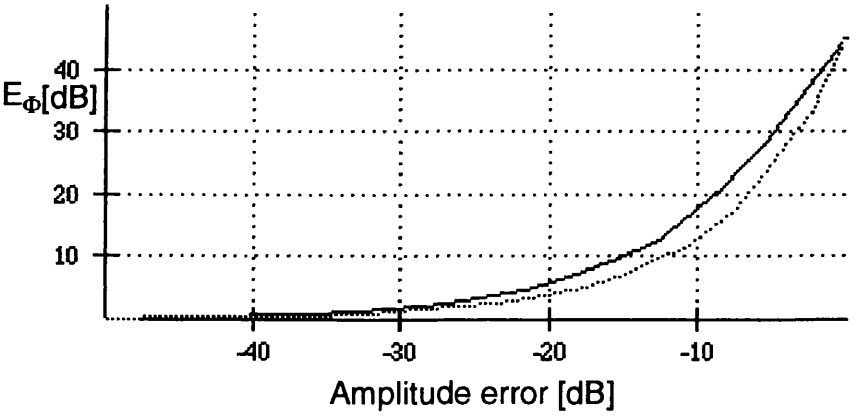

Fig.3.21 Peak (normal line) and standard deviation (dotted line) phase errors

Due to the unitary definition of the true vector, the previous figures can be directly related to the effect of signal-to-noise ratio on the power and phase errors. It is evident that in order to keep mean power and rms phase errors approximately around one decibel and 10 degree respectively, it is necessary to operate with signal-to-noise ratio larger than 10 dB.

In a multipolarisation SAR, the effect of thermal noise can be described expressing the measured Scattering matrix in the following way:

$$[S_m] = K \begin{bmatrix} 1 & \delta_1 \\ \delta_2 & f \end{bmatrix} \begin{bmatrix} S_{xx} & S_{xy} \\ S_{xy} & S_{yy} \end{bmatrix} \begin{bmatrix} 1 & \delta_2 \\ \delta_1 & f \end{bmatrix} + \begin{bmatrix} n_{xx} & \frac{n_{yx} + n_{xy}}{2} \\ \frac{n_{yx} + n_{xy}}{2} & n_{yy} \end{bmatrix} \quad 3.61$$

where K is a complex calibration factor, δ_1 and δ_2 are the cross talks associated to the vertical (y) and horizontal (x) polarisations respectively, f is the copolarised channel imbalance and n_{xx} , n_{yy}, n_{xy} are the thermal noise contributions in each polarisation channel. Due to the fact that during data compression the measured Scattering matrix is symmetrized, the radar system is forced to be reciprocal. It can be demonstrated that this operation does not affect the data calibration [57].

A standard algorithm to calibrate polarimetric SAR data has been introduced by JPL [58]. Using this technique it is possible to perform the radar cross talk calibration without relying on the presence of external calibration targets that are only needed for the channel imbalance and the absolute radiometric calibration. The fundamental assumption of this technique is the decorrelation of the copolarised and crosspolarised elements of the Scattering matrix. It has been demonstrated that this assumption is correct to second order Born approximation for a layer of randomly located elementary scatterers provided they present an azimuthally isotropic distribution [50].

A classical example of this assumption is the ocean composite surface scattering model [59]. In this case, the sign of the crosspolarised phase depends on the patch azimuth tilt direction, where the copolarised phase is independent of the sign of the tilt. Therefore assuming a symmetrical horizontal distribution of tilts with respect to zero, the correlation of the copolarised and crosspolarised

components of the backscattered electromagnetic field will result in a net contribution equal to zero.

The effect of thermal noise in the retrieval of the cross talk parameter is to increase the decorrelation between the uncalibrated copolarised and crosspolarised channels. This results in a poor estimation of the cross talk parameter since at the heart of the algorithm is the hypothesis of the correlation between the copolar and crosspolar channels due to the lack of isolation between them.

In the ideal case, the calibration algorithm allows us to retrieve cross talks, channel imbalance and the modulus of the complex calibration factor (its phase has limited importance with respect to polarisation applications). After polarimetric calibration, the cross-products of the calibrated Scattering matrix elements are calculated in order to estimate the Stokes scattering operator. Let us assume that the noise terms are zero mean gaussian distributed with copolarised noise powers equal to σ^2_{xx} and σ^2_{yy} and with equal noise power in the crosspolarised channels. Furthermore, the noise terms are also uncorrelated both from each other and from the useful signal. The resultant cross-products are:

$$\langle S_{xxm} S^*_{xxm} \rangle = \langle S_{xx} S^*_{xx} \rangle + \sigma^2_{xx} \qquad 3.62$$

$$\langle S_{yym} S^*_{yym} \rangle = \langle S_{yy} S^*_{yy} \rangle + \sigma^2_{yy} \qquad 3.63$$

$$\langle S_{xym} S^*_{xym} \rangle = \langle S_{xy} S^*_{xy} \rangle + \frac{\sigma^2_{xy}}{2} \qquad 3.64$$

$$\langle S_{xxm} S^*_{yym} \rangle = \langle S_{xx} S^*_{yy} \rangle \qquad 3.65$$

It appears evident that the knowledge of the noise power is of paramount importance to properly estimate the Stokes scattering operator. In particular the crosspolarised power is the quantity most sensitive to noise error due to the limited depolarising ability of most natural targets. It is interesting to note that after the symmetrization operation, the noise power in the crosspolarised channel is reduced by a factor of 2. This is the main justification for combining the crosspolarised channels of a polarimetric SAR [60].

To estimate the noise power in each polarisation channel, it is necessary to consider an area where first order Bragg scattering model applies [61]. The estimates are then subtracted from each relevant cross-product in order to remove the bias contribution of the thermal noise. It should be emphasised that in the Bragg scattering approximation, used for the estimation of the noise power, the Scattering matrix elements of the copolar channels are assumed to be in phase. This approximation is not always valid since the surface dielectric constant has an imaginary part due to the medium conductivity. The figure below shows the phase difference for the Bragg scattering model between copolarised channels for a sea surface at L band (normal line) and a moist soil at Ku band (dotted line).

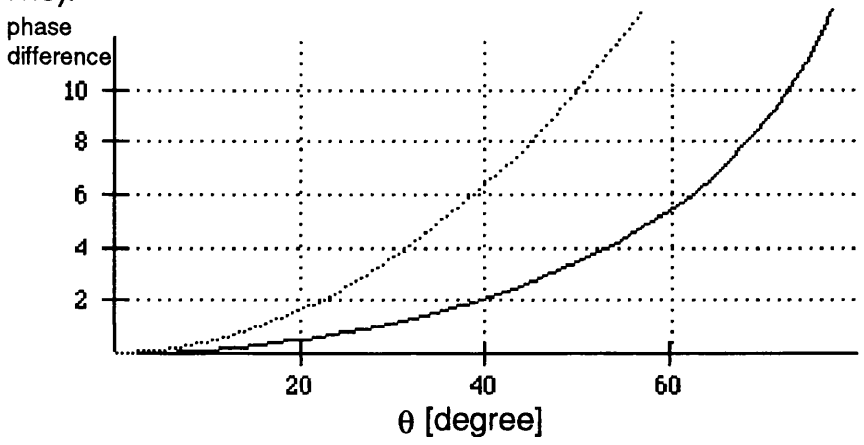

Fig.3.22 Phase difference between copolarised channels for a sea surface at L band (normal line) and a moist soil at Ku band (dotted line)

It appears evident that depending on the imaging geometry, frequency and surface characteristics, the phase difference can have a significant value. In particular, large incidence angles and higher carrier frequency will reflect in larger phase difference [62].(*)

A SAR capable of retrieving the full vectorial content of the backscattered radiation is very useful for discriminating different type of scattering interactions with the reflecting medium. However the complexity introduced by the multipolarisation capability is only justified if the increased information content added to the SAR data is deeply understood and extracted. The purpose of this chapter has been to analyse classical tools for describing the polarisation information. The next chapter will focus on alternative ways to retrieve scattering information from multipolarisation SAR data.

(*) Phase difference is small and probably not significant with present sensors, but may be with future ones.

4. THE COVARIANCE MATRIX IN SAR POLARIMETRY

4.1 *Introduction*

In the previous chapter the necessity to use second order statistical descriptors to properly characterise scattering from random media has been demonstrated. Classical second order descriptors for the modelling of vectorial scattering are the Mueller matrix, the Stokes scattering operator and the Coherence and Covariance matrices. The Mueller matrix and the Stokes scattering operator have often been utilised in SAR polarimetry due to their similarity with the Scattering matrix in relating the transmit and receive radiation characteristics.

The Coherence matrix, introduced by Wolf [63], has found wide applications in optics for the representation of quasi-monochromatic waves. The matrix elements are the ensemble average of the orthogonal components of the electromagnetic field. The Stokes parameters are equal to a linear combination of the Coherence matrix elements and consequently are capable of fully describing partially polarised electromagnetic radiation.

The Covariance matrix contains information directly related to the statistics of the Scattering matrix elements. For the backscatter direction for practically any natural surface even if it is inhomogeneous and anisotropic, the Covariance matrix consists of three real and three complex independent quantities. Being a positive semi-definite Hermitian matrix, its three eigenvalues are never negative and the corresponding eigenvectors are orthogonal. A large set of information such as target randomness, texture, thermal noise

content, polarisation matching capability can be extracted from the Covariance matrix.

The main objectives of this chapter are to present a detailed analysis of Covariance matrix applications in SAR polarimetry and to demonstrate the capability of this second order descriptor in generating useful quantities for the characterisation of the SAR polarimetric data.

4.2 *Covariance matrix theory*

The Covariance matrix for a polarimetric SAR (Σ) in the linear polarisation basis (H,V) can be defined in the following way:

$$\vec{X} = \begin{bmatrix} S_{HH} \\ \sqrt{2}\, S_{HV} \\ S_{VV} \end{bmatrix} \qquad [\Sigma] = \langle \vec{X}\, \vec{X}^{+} \rangle \qquad 4.1$$

where + denotes complex conjugate transpose. It is important to emphasise that in the previous definition of the feature vector X , it is assumed that the reflecting medium is reciprocal, therefore a three dimensional vector is sufficient for the complete characterisation of the Scattering matrix. Expanding the vector multiplication, the Covariance matrix becomes:

$$[\Sigma] = \begin{bmatrix} \langle |S_{HH}|^2 \rangle & \langle \sqrt{2}\, S_{HH} S_{HV}^{*} \rangle & \langle S_{HH} S_{VV}^{*} \rangle \\ \langle \sqrt{2}\, S_{HV} S_{HH}^{*} \rangle & \langle 2|S_{HV}|^2 \rangle & \langle \sqrt{2}\, S_{HV} S_{VV}^{*} \rangle \\ \langle S_{VV} S_{HH}^{*} \rangle & \langle \sqrt{2}\, S_{VV} S_{HV}^{*} \rangle & \langle |S_{VV}|^2 \rangle \end{bmatrix} \qquad 4.2$$

the main diagonal elements represent the mean backscattered power in each polarisation channel (the mean crosspolar power is actually multiplied by a factor of two), the other elements are the interchannel

complex correlations. For simplicity a factor proportional to the transmit power, antenna and receiver gain has been set equal to one.
The Covariance matrix Σ is positive semi-definite Hermitian, therefore its eigenvalues are never negative and it is always possible diagonalize Σ by means of unitary similarity transformation [64].

The presence of the factor $\sqrt{2}$ in the definition of the feature vector is due to the necessity of having invariant eigenvalues for any chosen polarisation basis. It has been demonstrated that selecting a proper unitary polarisation transformation matrix together with the introduction of the factor $\sqrt{2}$ in crosspolar component of the feature vector, it is possible to describe the Covariance matrix in any arbitrary orthonormal basis keeping the eigenvalues invariant [65,66]. It is therefore important to stress the arbitrary nature of the (H,V) polarisation basis choice. Indeed applying the following unitary polarisation transformation matrix [65,66]:

$$[T(\rho)] = \frac{1}{(1+\rho\rho^*)} \begin{bmatrix} 1 & \sqrt{2}\,\rho & \rho^2 \\ -\sqrt{2}\,\rho^* & (1-\rho\rho^*) & \sqrt{2}\,\rho \\ \rho^{*2} & -\sqrt{2}\,\rho^* & 1 \end{bmatrix} \qquad 4.3$$

where ρ is a parameter (i.e. the polarisation ratio) depending only on the orientation angle and ellipticity of the selected polarisation basis according to the following expression:

$$\rho = \frac{\cos(2\tau)\sin(2\varepsilon) + j\sin(2\tau)}{1 + \cos(2\tau)\cos(2\varepsilon)} \qquad 4.4$$

the Covariance matrix can be expressed in any polarisation basis defined by ρ by means of the following unitary similarity transformation:

$$[\Sigma_\rho] = [T(\rho)][\Sigma_{HV}][T(\rho)^+] \qquad 4.5$$

where the subscripts of Σ identify the polarisation basis.

As a consequence of the unitary similarity transformation choice the following equality holds:

$$\text{trace}(\Sigma) = \sum_{n=1}^{3} \lambda_n = \langle \text{span}(S) \rangle \qquad 4.6$$

The property to preserve eigenvalues under any polarisation basis transformation is very important from a physical point of view: the ensemble average of the span of the Scattering matrix is the total backscattered mean power in the four polarisation channels, therefore it should be independent of the polarisation basis choice.

Another important consequence of the previous formulation is to provide polarisation basis-invariant bounds for the copolarised and crosspolarised backscattered powers, indeed the main diagonal elements in a positive semi-definite Hermitian matrix are always bounded to lie between the minimum and maximum eigenvalues as shown in the following inequalities [64]:

$$\lambda_{min} \leq \langle |S_{HH}|^2 \rangle \leq \lambda_{max} \qquad 4.7$$

$$\lambda_{min} \leq \langle |S_{VV}|^2 \rangle \leq \lambda_{max} \qquad 4.8$$

$$\frac{1}{2}\lambda_{min} \leq \langle |S_{HV}|^2 \rangle \leq \frac{1}{2}\lambda_{max} \qquad 4.9$$

It is not always possible to maximise or minimise the copolar or the crosspolar backscattered power in order to obtain the upper or lower bounds (i.e. λ_{max}, λ_{min}), indeed even if the matrix $T(\rho)$ is a unitary transformation, it might not diagonalize the Covariance matrix (in other words it is not guaranteed that one of the columns of $T(\rho)$ is equal to the corresponding eigenvector of Σ).

The ensemble average operator applied to the Covariance matrix elements, indicates spatial averaging and consequently spatial homogeneity of the imaged scene is assumed. In this case, the reduced statistical fluctuation is achieved at the price of decreased spatial resolution. An important application in polarimetric SAR is the utilisation of the polarisation channels to decrease speckle noise without affecting the spatial resolution of the sensor. As will be shown in the following analysis, the overall effect of this technique depends on the nature of the backscattered radiation.

4.3 *Gaussian polarimetric clutter model*

Under the assumptions that the copolarised and crosspolarised components of the Scattering matrix are uncorrelated for an azimuthally symmetric surface, and each component of the feature vector has zero mean because of their predominant incoherent nature, the Covariance matrix in an arbitrary selected polarisation basis (H,V), assumes the following configuration:

$$[\Sigma] = \begin{bmatrix} <|S_{HH}|^2> & 0 & < S_{HH} S_{VV}^* > \\ 0 & 2<|S_{HV}|^2> & 0 \\ < S_{VV} S_{HH}^* > & 0 & <|S_{VV}|^2> \end{bmatrix} \qquad 4.10$$

Let us consider a complex Gaussian model for a statistical homogeneous surface, where the probability density function (PDF) of the feature vector X is [67,68]:

$$F(\vec{X}) = \frac{1}{\pi^3 |\Sigma|} \exp[-\vec{X}^+ \Sigma^{-1} \vec{X}] \qquad 4.11$$

It appears evident that the knowledge of the Covariance matrix is capable of completely characterising the statistical homogeneous surface. An important consequence of having the Scattering matrix elements jointly Gaussian is that zero covariance between two

elements implies statistical independence. Therefore in the presence of azimuthally symmetric surfaces, the crosspolar return is independent of both copolar returns.

It is interesting to calculate the three eigenvalues of Σ in order to analyse the polarisation characteristics of the backscattered radiation. Solving the eigenvalue equation for the matrix (4.10), we obtain:

$$\lambda_1 = 2\langle|S_{HV}|^2\rangle \qquad 4.12$$

$$\lambda_{2,3} = \frac{\langle|S_{HH}|^2\rangle + \langle|S_{VV}|^2\rangle \pm \langle|S_{HH}|^2\rangle\sqrt{(\mu - 1)^2 + 4|\gamma|^2}}{2} \qquad 4.13$$

where μ and γ are respectively the copolarisation ratio and the correlation between the two copolarised channels according to the following definitions :

$$\mu = \frac{\langle|S_{VV}|^2\rangle}{\langle|S_{HH}|^2\rangle} \qquad 4.14$$

$$\gamma = \frac{\langle S_{HH} S_{VV}^*\rangle}{\sqrt{\langle|S_{HH}|^2\rangle\langle|S_{VV}|^2\rangle}} \qquad 4.15$$

The first eigenvalue, being associated with the power in the crosspolarised channel for the horizontal and vertical polarisation basis choice, can be related to target properties. If the individual scatterers in the scene have a Scattering matrix that is a weak function of their orientation or if the scatterers are highly aligned along the transmitting and receiving polarisations, then typically the first eigenvalue will be small with respect to the copolarised received power.

From the analysis of the eigenvalues, it seems that the vertical and horizontal polarisations have a privileged role in the computation of the Covariance matrix. This is due to the preliminary assumption of having copolarised and crosspolarised scattering terms uncorrelated in the chosen orthogonal polarisation basis. It can be demonstrated that to maximise or minimise the mean power scattered into a particular polarimetric channel the following conditions, for the copolar and crosspolar powers have to be satisfied respectively [65]:

$$< S_{AA}(\rho)\, S^{*}_{AB}(\rho) > = < S_{BB}(\rho)\, S^{*}_{AB}(\rho) > = 0 \qquad 4.16$$

$$< S_{AA}(\rho)\, S^{*}_{AB}(\rho) > - < S_{BB}(\rho)\, S^{*}_{AB}(\rho) > = 0 \qquad 4.17$$

where in each case the parameter ρ defines the optimum polarisation. According to the simplified Covariance matrix formulation 4.10, both equations are satisfied for $\rho=0$ (i.e. AB $\equiv$ HV).

It is interesting to relate the eigenvalues to the polarisation characteristics of the backscattered radiation. For this purpose, it is useful to define the Coherence matrix that for a time-varying partially polarised plane wave is described in the following way:

$$[J] = \begin{bmatrix} J_{11} & J_{12} \\ J_{21} & J_{22} \end{bmatrix} = \begin{bmatrix} < E_H E^{*}_H > & < E_H E^{*}_V > \\ < E^{*}_H E_V > & < E_V E^{*}_V > \end{bmatrix} \qquad 4.18$$

where E_H and E_V denote the orthogonal linearly polarised components of the electric field. From this matrix the conditions for completely polarised and unpolarised radiation waves are respectively [69]:

$$|J| = J_{11}J_{22} - |J_{12}|^2 = 0 \qquad 4.19$$

$$J_{12} = J_{21} = 0 \; ; J_{11} = J_{22} \qquad 4.20$$

The first condition states that in order to have a fully polarised backscattered wave the coherence matrix must be singular. The second condition states that for an unpolarised wave, the intensity measured in any direction orthogonal to the propagation direction is the same, and such that this intensity is not affected by any relative delay between the electric field components. Expressing the previous conditions in terms of Scattering coefficients:

$$E_{Hr} = S_{HH} E_{Ht} + S_{HV} E_{Vt} \qquad 4.21$$

$$E_{Vr} = S_{VV} E_{Vt} + S_{HV} E_{Ht} \qquad 4.22$$

where the subcripts t and r denote transmit and reflected electric fields respectively, we obtain the following formulation (maintaining the hypothesis that the copolarised and crosspolarised component of the Scattering matrix are uncorrelated):

$$|J| = 0 \Rightarrow \langle |S_{HV}|^2 \rangle = 0 \; ; \; |\gamma|^2 = 1 \qquad 4.23$$

$$J_{12} = J_{21} = 0 \; ; \; J_{11} = J_{22}$$

$$\Downarrow$$

$$\langle S_{HH} S_{VV}^* \rangle = \langle S_{HH}^* S_{VV} \rangle = -\langle |S_{HV}|^2 \rangle \; ; \; \langle |S_{HH}|^2 \rangle = \langle |S_{VV}|^2 \rangle \qquad 4.24$$

Note in both derivations it is assumed that $\langle |S_{HH}|^2 \rangle$ and $\langle |S_{VV}|^2 \rangle$ are different from zero (a realistic approximation for most natural targets), and only for the unpolarised condition it is assumed $E_{Ht} = E_{Vt}$.

The first formulation above states that in order to have a completely polarised wave regardless of the transmit polarisation, it is necessary that the crosspolarised power is equal to zero and the copolarised

channels are fully correlated. This conclusion can also be reached using the Stokes vector formulation [70].

Forcing the fully polarised condition in the eigenvalue formulation, we obtain that two eigenvalues of the Covariance matrix are equal to zero and the remaining one is equal to $<|S_{HH}|^2> + <|S_{VV}|^2>$ (as we expected in order to maintain the overall backscatter power invariant and equal to the span of the Scattering matrix). Expressing the determinant of the Covariance matrix as the product of its three eigenvalues, it is evident that the singularity of the Covariance matrix is a necessary condition to have a completely polarised return [70].

Strictly speaking this is the case for deterministic targets where in the definition of the Covariance matrix the average operator does not find application. The lower limit of the copolar and crosspolar channel powers has a lower bound equal to zero demonstrating that in the presence of deterministic targets it is always possible to obtain vanishing power returns.

In the case of unpolarised radiation the three eigenvalues of the Covariance matrix are:

$$\lambda_1 = 2 <|S_{HV}|^2> \qquad 4.25$$

$$\lambda_2 = <|S_{HH}|^2> - <|S_{HV}|^2> \qquad 4.26$$

$$\lambda_3 = <|S_{HH}|^2> + <|S_{HV}|^2> \qquad 4.27$$

The lower bound for the backscattered power is always larger than zero unless the crosspolarised term vanishes or the power in the copolar channel is equal to the crosspolarised power. In the most general case, it will not be possible to find any polarisation basis that produces zero return in the polarimetric radar channels. It is important to realise that the unpolarised condition has been found

assuming the transmit electric fields to be identical in both polarisations, as it is the case in most multipolarisation radars. In general, there are no conditions for the unpolarised radiation based only on the Scattering matrix elements.

Experimental results have shown that using the linear polarisation basis, the crosspolar return is often much weaker than the copolarised return. In particular, multipolarisation SAR images of ocean surfaces and bare land have produced very limited contribution of the crosspolarised power. However, for heavily vegetated area the amount of power associated with linear depolarisation is often considerable [71].

An important application of the Covariance matrix is the maximisation problem associated with the Rayleigh quotient. Defining the following linear combination:

$$y = \vec{W}^{+}\vec{X} \qquad 4.28$$

where W is a three dimensional complex weight vector, it is easy to demonstrate the direct relation between W and the transmit and receive complex antenna states. Expressing the received antenna voltage as a function of the Scattering matrix:

$$y = [H_r\, V_r]\begin{bmatrix} S_{HH} & S_{HV} \\ S_{HV} & S_{VV} \end{bmatrix}\begin{bmatrix} H_t \\ V_t \end{bmatrix} \qquad 4.29$$

By direct comparision the following relations are obtained:

$$W^{*}_{HH} = H_t\, H_r \qquad 4.30$$

$$W^{*}_{HV} = \frac{1}{\sqrt{2}}(H_t\, V_r + H_r\, V_t) \qquad 4.31$$

$$W^{*}_{VV} = V_t V_r \qquad 4.32$$

where H and V are the horizontal and vertical complex states of the antenna polarisations and the subscripts t and r denote the transmit and receive antennas respectively. Due to the definition of the feature vector for reciprocal medium, the above equations define the antenna complex states in a reciprocal way as well. The exchange of optimal transmit and receive antenna polarisations will not affect the weight vector components [72,73].

The received power from a target with a feature vector X is:

$$P = |y|^2 = \vec{W}^+ \Sigma \vec{W} \qquad 4.33$$

where a constant factor related to the antenna impedance has been omitted. The above expression demonstrates the direct relation between the Covariance matrix and the target backscattered energy.

The positive semi-definite nature of the Covariance matrix allows us to write the Rayleigh maximisation principle [64]:

$$MAX\left[\frac{\vec{W}^+ \Sigma \vec{W}}{\vec{W}^+ \vec{W}}\right] = \frac{\vec{X}_3^+ \lambda_3 \vec{X}_3}{\vec{X}_3^+ \vec{X}_3} = \lambda_3 \qquad 4.34$$

where λ_3 and X_3 denote the largest eigenvalue and the associated eigenvector respectively. The numerator of the above expression can be interpreted as the power received from a target with covariance matrix Σ for a transmit/receive antenna polarisation of the sensor related to the complex components of W. It is not surprising that the optimisation of an Hermitian form leads to an eigenvalue problem. Indeed, to find the extremum of a quadratic function it is necessary to solve a linear equation.

The maximum received power corresponds to the largest eigenvalue but it is not always possible to obtain it since the eigenvector X_3 can lead to not-unitary antenna polarisation states. Alternatively, the

Rayleigh quotient forces the length of the eigenvector to be constant where an unitary antenna state will demand variation of the eigenvector length. It is trivial to show that for equal transmit and receive polarisation states, under the constraint of unitary antenna states (i.e. $|H|^2 + |V|^2 = 1$), the magnitude of the vector W is always equal to one. It is important to mention that this property is directly related to the chosen definition of the feature vector that allows to preserve the Scattering matrix span. However even if the magnitude of the vector W becomes equal to one, the Covariance matrix optimisation method will only provide upper or lower bounds in general not achievable with unitary antenna polarisation states [72].

The antenna polarisation states associated with X_3, are also capable of maximising the signal-to-noise ratio as can be easily shown applying the Rayleigh quotient to the ratio of the received power to the noise power. In more general terms, the Covariance matrix has a fundamental role in the maximisation of the power backscattered from an area of Covariance matrix Σ_A with respect to the power from an area of Covariance matrix Σ_B [73]. The mathematical formulation of this maximisation problem is:

$$\text{MAX}\left[\frac{\vec{W}^{+}\Sigma_A\,\vec{W}}{\vec{W}^{+}\Sigma_B\,\vec{W}}\right] = r_{AB} \qquad 4.35$$

where r_{AB} is called the maximum contrast ratio between target A and target B. To simplify the problem, it is useful to transform the vector W into a new coordinate system using the following linear transformation:

$$\vec{F} = [P]^{-1}\vec{W} \qquad 4.36$$

If P is the eigenvector matrix of $\Sigma_B^{-1}\Sigma_A$ then the following identities hold [74]:

$$[P^{+}][\Sigma_A][P] = [D] \qquad 4.37$$

$$[P^+][\Sigma_B][P] = [I] \qquad 4.38$$

where D is the eigenvalue matrix of $\Sigma_B^{-1}\Sigma_A$. Substituting the vector F in place of vector W in the maximisation ratio, we obtain:

$$r_{AB} = MAX\left[\frac{\vec{F}^+ P^+ \Sigma_A P \vec{F}}{\vec{F}^+ P^+ \Sigma_B P \vec{F}}\right] = MAX\left[\frac{\vec{F}^+ D \vec{F}}{\vec{F}^+ \vec{F}}\right] \qquad 4.39$$

therefore the original maximisation problem has been converted to the Rayleigh quotient one, of which we already know the solution:

$$r_{AB} = MAX\left[\frac{\vec{F}^+ D \vec{F}}{\vec{F}^+ \vec{F}}\right] = \lambda_3 \qquad 4.40$$

where λ_3 is largest eigenvalue of $\Sigma_B^{-1}\Sigma_A$. The value of F that satisfies the maximisation ratio is independent of any complex scalar factor, therefore choosing the following condition for F:

$$\vec{F}^+ \vec{F} = 1 \qquad 4.41$$

the previous equation can be expressed in the following way:

$$\vec{F}^+ D \vec{F} = \lambda_1 |F_1|^2 + \lambda_2 |F_2|^2 + \lambda_3 |F_3|^2 \leq \lambda_3 |F|^2 \qquad 4.42$$

where the largest value of the above product is obtained by choosing the F vector equal to:

$$\vec{F}^t = [0\ 0\ 1] \qquad 4.43$$

that translates for the vector W, in the eigenvector of $\Sigma_B^{-1}\Sigma_A$ correponding to the largest eigenvalue λ_3. This maximisation problem reduces to the previously analysed single Covariance matrix Rayleigh quotient if Σ_B becomes the identity matrix.

The eigenvalues of the Covariance matrix are not only capable of defining the upper and lower limits of the polarised backscattered power, but are also directly related to the statistical variability of a multipolarised SAR span image. The span image of a multipolarised SAR is constructed in the following way:

$$y = \vec{X}^{+}\vec{X} \qquad 4.44$$

therefore the pixel intensity is the noncoherent summation of the three polarisation channels. In order to generalise the result of the following analysis, it is useful to introduce a weighting matrix A: consequently the pixel intensity of the generalised span image becomes:

$$y = \vec{X}^{+}[A]\vec{X} \qquad 4.45$$

To evaluate the statistical properties of the generalised span image, it is important to calculate the mean and the variance of the previously defined pixel intensity. In the assumption of A being positive semi-definite Hermitian matrix, the following matrix relations hold [74,75]:

$$[M^{+}][A][M] = [\Lambda] \qquad 4.46$$

$$[M^{+}][\Sigma^{-1}][M] = [I] \qquad 4.47$$

where Λ and M are the eigenvalue and eigenvector matrices of Σ A. Using the previous relations, the generalised pixel intensity of the span image can be expressed in the following way:

$$y = \vec{X}^{+}[M]^{-1} + [\Lambda][M]^{-1}\vec{X} \qquad 4.48$$

$$y = \vec{Z}^{+}[\Lambda]\vec{Z} \qquad 4.49$$

where Z is related to X through the linear transformation M^{-1}. Expanding the matrix product the above relation becomes:

$$y = \sum_{i=1}^{3} \lambda_i |z_i|^2 \qquad 4.50$$

The Covariance matrix of Z can be expressed in term of Σ, and applying the relation 4.47 we obtain:

$$<\vec{Z}\vec{Z}^{+}> = [M]^{-1}[\Sigma]\,[M]^{-1+} = [I] \qquad 4.51$$

Consequently the mean of the generalised pixel intensity is:

$$<y> = \sum_{i=1}^{3} \lambda_i \qquad 4.52$$

In order to calculate the variance, it is necessary to determine the average pixel power. Being derived from a linear transformation of X, the components of the vector Z are complex zero mean Gaussian distributed. The average pixel power is expressed in the following way:

$$<y^2> = \sum_{i=1}^{3} \lambda_i^2 <|z_i|^4> + \sum_{i=1}^{3} \sum_{j=1\ (i\neq j)}^{3} \lambda_i \lambda_j <|z_i|^2><|z_j|^2> \qquad 4.53$$

where the fourth order term is calculated expressing z_i through the inphase I_i and quadrature Q_i components:

$$<|z_i|^4> = <(I_i^2 + Q_i^2)^2> = <I_i^4> + 2<I_i^2><Q_i^2> + <Q_i^4> \qquad 4.54$$

For a real Gaussian variable with standard deviation σ, the following relation holds:

$$<I_i^n> = <Q_i^n> = 1 \cdot 3 \cdot\cdot\ (n-1)\sigma^n \ \ (n \text{ even}) \qquad 4.55$$

Since the Covariance matrix of Z is equal to the identity matrix, σ^2 is equal to 1/2, and substituting the above relations in the average pixel power expression, we obtain:

$$< y^2 > = \sum_{i=1}^{3} \lambda_i^2 + \left(\sum_{i=1}^{3} \lambda_i \right)^2 \qquad 4.56$$

Consequently the variance of the pixel intensity of the generalised span image is:

$$\text{var (y)} = \sum_{i=1}^{3} \lambda_i^2 \qquad 4.57$$

It is useful to define the ratio between the variance (var) and the squared average of the pixel intensity as a quantitative measure of the speckle content of the generalised span image:

$$\frac{\text{var (y)}}{<y>^2} = \frac{\sum_{i=1}^{3} \lambda_i^2}{\left(\sum_{i=1}^{3} \lambda_i \right)^2} \qquad 4.58$$

The minimisation of the above ratio with respect to the eigenvalues of ΣA is obtained applying the method of Lagrange multipliers [76]. Due to the independence of the solution from any complex scalar factor, the arbitrary constraint in the Lagrange method can be chosen according to the following condition:

$$\sum_{i=1}^{3} \lambda_i = 3 \qquad 4.59$$

and the minimisation of the above ratio is translated into the minimisation of the functional expressed in the next page:

$$f(\lambda_1,\lambda_2,\lambda_3,\gamma) = \sum_{i=1}^{3} \lambda_i^2 + \gamma\,(9 - \left(\sum_{i=1}^{3} \lambda_i\right)^2) \qquad 4.60$$

where γ is the Lagrange multiplier. Taking the partial derivative of the above expression with respect to λ_i and finding the roots of the resulting equation, we obtain:

$$\lambda_1 = \lambda_2 = \lambda_3 = 1 \qquad 4.61$$

This solution corresponds to a weighting matrix A equal to the inverse of the Covariance matrix Σ. In this case the ratio between the standard deviation (sd) and the mean of the generalised pixel intensity of the span image becomes:

$$\frac{sd\,(y)}{<y>} = \frac{1}{\sqrt{3}} \qquad 4.62$$

The effect of the optimal weighting matrix can be easily understood expressing the pixel intensity in the following way:

$$y = \vec{X}^{+}[A]\,\vec{X} = \vec{X}^{+}[\Sigma]^{+\,-\frac{1}{2}}[\Sigma]^{-\frac{1}{2}}\vec{X} \qquad 4.63$$

therefore the matrix A can be interpreted as equivalent to the linear transformation $\Sigma^{-\frac{1}{2}}$ applied to the feature vector X. This is actually a modification of the polarisation basis of the feature vector capable of representing X in a new polarisation basis where the three polarisation components are uncorrelated and of equal average power. To demonstrate this property of the optimal weighting matrix, it is necessary to calculate the Covariance matrix of the feature vector represented in its new polarisation basis:

$$[\Sigma_{optimal}] = <[\Sigma]^{-\frac{1}{2}}\,\vec{X}\,\vec{X}^{+}\,[\Sigma]^{+\,-\frac{1}{2}}> = [\Sigma]^{-\frac{1}{2}}[\Sigma]\,[\Sigma]^{+\,-\frac{1}{2}} = [\,I\,] \qquad 4.64$$

In the new polarisation basis the average powers of the components of the feature vector act as three ideal looks for the generalised span intensity image.

Since in spaceborne radar applications the implementation of the crosspolar channel is often technologically very challenging (i.e. transmit power, thermal noise floor and antenna polarisation isolation), it is interesting to apply the optimal weighting matrix approach when only the two copolar channels are available. In this case the feature vector becomes bidimensional and consequently the number of eigenvalues is reduced to two. Following the previous derivation, it is trivial to demonstrate that the variance to mean square ratio is equal to 0.5. Therefore, regardless of the intrinsic correlation generated by the scene, the optimal weighting matrix is always capable of obtaining two independent looks.

The case in which the linear operator A is not applied, corresponds to the classical span image, where the pixel intensity is expressed in the following matrix formulation:

$$y = [S_{HH}^{*}, \sqrt{2}\, S_{HV}^{*}, S_{VV}^{*}] \begin{bmatrix} 1 & 0 & 0 \\ 0 & 1 & 0 \\ 0 & 0 & 1 \end{bmatrix} \begin{bmatrix} S_{HH} \\ \sqrt{2}\, S_{HV} \\ S_{VV} \end{bmatrix} \qquad 4.65$$

The ratio between the pixel standard deviation and the average mean power is:

$$\frac{sd\,(y)}{\langle y \rangle} = \frac{\sqrt{\left(\langle |S_{HH}|^2 \rangle\right)^2 + 4\left(\langle |S_{HV}|^2 \rangle\right)^2 + \left(\langle |S_{VV}|^2 \rangle\right)^2 + 2\left(\langle |S_{HH}|^2 \rangle\right)^2 |\mu|^2}}{\langle |S_{HH}|^2 \rangle + 2\langle |S_{HV}|^2 \rangle + \langle |S_{VV}|^2 \rangle} \qquad 4.66$$

The main difference with respect to the optimised solution is that the above formula does not utilise the phase difference between the two

copolarised channels but only the amplitude information of the correlation coefficient. Therefore in order to achieve optimal speckle reduction in the span intensity image, the copolarised channels phase difference should be preserved.

From the previous formula two simple cases can be derived according to the following characteristics of the backscattered radiation:

$$\begin{gathered} \langle |S_{VV}|^2 \rangle = 10 \langle |S_{HH}|^2 \rangle \; ; \; \langle |S_{HV}|^2 \rangle = 0 \; ; \; |\gamma| = 1 \\ \Downarrow \\ \frac{sd\,(y)}{\langle y \rangle} = 1 \end{gathered} \qquad 4.67$$

$$\begin{gathered} \langle |S_{HH}|^2 \rangle = \langle |S_{VV}|^2 \rangle = \langle |S_{HV}|^2 \rangle \; ; \; |\gamma| = 0 \\ \Downarrow \\ \frac{sd\,(y)}{\langle y \rangle} = \frac{\sqrt{6}}{4} \approx 0.6 \end{gathered} \qquad 4.68$$

where the first case can be associated with a strong Bragg scattering behaviour (i.e. ocean surface for large incidence angle) and the second one with highly unpolarised radiation (i.e. forest area at low radar carrier frequency). It is worth mentioning that due to the introduction of the factor $\sqrt{2}$ in the definition of the feature vector, in the second case it is not possible to achieve the same result as for the optimal weighting matrix. Indeed to find the maximum speckle reduction, we shall have set the average crosspolarised power equal to half of the average of the copolarised power.

The main advantage in using the classical polarimetric span processing with respect to the optimal case is due to the necessity of having only the amplitude information of the correlation coefficient. It

can be demonstrated that under the assumption of Gaussian clutter the following relation holds [77]:

$$< (|S_{HH}|^2 - <|S_{HH}|^2>)(|S_{VV}|^2 - <|S_{VV}|^2>) >= |<S_{HH} S_{VV}^*>|^2 \quad 4.69$$

therefore to compute the amplitude of the correlation coefficient only the knowledge of the intensity statistics is necessary. Furthermore, the intensity statistics of the copolarised channels can be estimated accurately independently from cross talk, channel imbalance and deployment of calibration targets [78].

It is interesting to associate the eigenvalue description of the span image with the intrinsic variability of the pixel intensity. In a SAR image, the signal intensity modulation is typically due to three effects: the speckle noise, the scene texture and thermal noise (other noise sources such as saturation noise, quantization noise and processing noise are considered negligible). The speckle noise is directly associated with the coherent nature of the sensor, and under the assumption of having a small signal bandwidth with respect to the radar bandwidth, this term can be characterised as a multiplicative stationary independent zero mean complex Gaussian noise. Exceptions to this classical way to model the speckle contribution are when a dominant elementary scatterer is located in the resolution cell or when the target autocorrelation function is not slowly varying from one pixel to the adjacent one [79,80].

The image texture is associated with the spatial variability of the scattering properties of the scene. It is directly related to the nature of the reflecting medium and carries useful information for characterising the imaged surface. The effect on the pixel intensity variability is of the same nature as the speckle noise (i.e. multiplicative), however it is important to appreciate the following difference: where the speckle noise is due to the variability of the random position of the elementary scatterers for displacement of the

order of the wavelength, the texture is associated with larger scale variations so that the scattering properties of the reflecting surface are modified. Comparing adjacent pixels in a SAR image, the two types of phenomena are observed simultaneously.

It is of fundamental importance to be capable to characterise the speckle and texture statistics in order to properly evaluate their effects on SAR images. The model used to describe the intensity image is [79,81]:

$$P_{i,j,f} = [< I >_f T_{i,j,f} + < n_i >] S_{i,j} \qquad 4.70$$

where P is the intensity associated to a pixel of coordinate i (range), j (azimuth) and from a region f of homogenous scattering characteristics with average reflected power <I>. The independent random variables T and S characterise texture and speckle contributions respectively. They both have unit mean, and the speckle component is independent from any type of imaged scene. Indeed the speckle contribution will result from the statistical nature of the scene provided the surface roughness is capable of producing phase excursions comparable to 2π. An increase in roughness will not modify the statistics of S.

The noise power contribution <n> is described as an additive component modulated by the speckle and only depending on the range coordinate. The range dependence of the noise power is related to the choice of the azimuth correlator reference function. Typically the number of samples in the azimuth correlator will be proportional to the slant range variation and correspondingly the signal-to-noise ratio at pixel level will present a R^{-3} range dependence. In this case, a noise power range variation proportional to R will appear. If noise subtraction is applied, then it is very useful to weight the correlation process in order to compensate the noise power variation. This can be achieved using a normalisation factor

inversely proportional to the square root of the azimuth samples, or just fixing the correlator length at the price of having a variable resolution versus incidence angle (i.e. SEASAT JPL correlator). The assumption in the previous model of the noise term as equivalent to the texture with respect to the speckle effect is justified by the filtering function of the SAR processor on the received echo dictating its correlation property. Alternatively, there is no difference between the statistical properties of the speckle term and thermal noise with the exception of the azimuth antenna pattern weighting of the speckle power spectrum. According to the previously described model, the average pixel intensity is :

$$< P_{i,j,f} > = < I >_f + < n_i > \qquad 4.71$$

This derivation demonstrates the need to estimate the noise contribution to retrieve backscattered properties from a homogenous statistical region.

To compute the variance of the texture variable, it is necessary to utilise the following relation for the variance to mean square ratio of the speckle term:

$$\frac{\text{var (S)}}{< S >^2} = \frac{1}{N} \qquad 4.72$$

where N is the number of effective looks. Typically in SAR images, the independent samples are generated by combining incoherently adjacent pixels. Because of the sampling of data, the adjacent pixels are often correlated due to oversampling of the speckle correlation function. It is therefore necessary to introduce the concept of effective number of looks to properly simulate the averaging process.

A simplified way to estimate N without requiring the knowledge of the speckle second order signal statistics, is:

$$N \approx \text{number of averaged pixels} \times \frac{\text{pixel spacing}}{\text{spatial resolution}} \qquad 4.73$$

It is necessary to notice that the texture itself will generate a correlation between adjacent pixels, however the effect will often be dominated by the speckle. Indeed with the assumption of stationary spatial statistics and negligible noise power, the overall pixel autocorrelation function is [81]:

$$R_P(\Delta_i, \Delta_j, f) \approx \langle I \rangle^2_f R_T(\Delta_i, \Delta_j, f) R_S(\Delta_i, \Delta_j) \qquad 4.74$$

where R_T and R_S are the texture and speckle autocorrelation functions respectively. R_S closely resembles the SAR impulse response function and will rapidly vanish for value of Δ_i and Δ_j larger than the SAR spatial reolution. The texture autocorrelation function will depend on the spatial homogeneity of the imaged scene and unless very high spatial resolution is involved together with the presence of strong dominant elementary scatterers, the overall spatial decay will be dictated by the speckle decorrelation.

Using the previous formulation, the variance of the pixel intensity can be computed:

$$\text{var}(P_f) = \langle P_f^2 \rangle - \langle P_f \rangle^2 = \frac{\text{var}(T_f) \langle I \rangle^2_f (N+1) + \langle P_f \rangle^2}{N} \qquad 4.75$$

and consequently expressing the signal-to-noise ratio as $\frac{\langle I \rangle}{\langle n \rangle}$, the variance of the texture random variable is obtained:

$$\text{var}(T_f) = \frac{N\left(\frac{\text{var}(P_f)}{\langle P_f \rangle^2}\right) - 1}{N+1} \left(1 + \frac{1}{SNR_f}\right)^2 \qquad 4.76$$

The previous expression can be seen as a measure of the difference between the normalised intensity and the speckle variances. The effect of thermal noise on the texture variance estimation is to increase the pixel intensity variability and therefore to overestimate the texture variance. If the noise power is neglected in the calculation of the texture variance, the following error will affect the estimation:

$$E = 20 \log \left(1 + \frac{1}{SNR}\right) \qquad 4.77$$

The diagram in figure 4.1 demonstrates the necessity of operating with high signal-to-noise ratio if the texture variance has to be estimated. Indeed to have an error less than 1 dB (corresponding to a 10 per cent error), it is necessary to operate with signal-to-noise ratio approximately larger than 10 dB

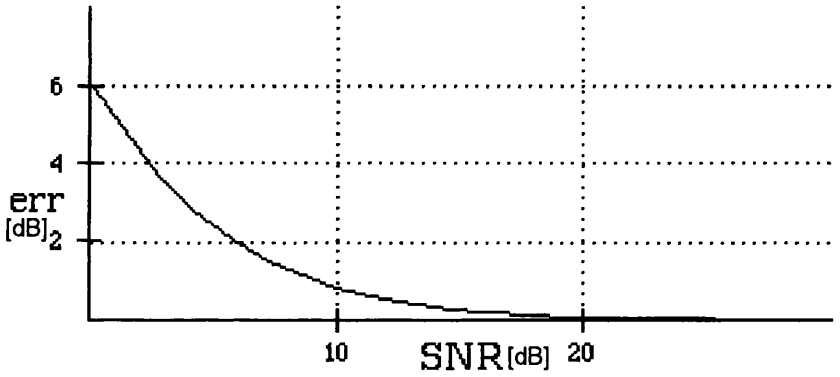

Fig.4.1 Texture variance error as a function of signal to noise ratio

The texture variance is directly related to the target spatial characteristics, and if properly estimated it can improve the scene characterisation. However for having a complete texture description, different incidence angles, spatial resolutions and wavelength should be utilised to sense the largest set of scattering mechanisms associated with the area of interest.

4.4 *Non-Gaussian polarimetric clutter model*

At the heart of Gaussian clutter model there is the assumption that a large number of randomly distributed elementary scatterers exists in the resolution cell with no single scatterer dominating. This is the classical way to model the speckle phenomena. However to be capable of describing the variation of scattering properties of the scene due to the lack of spatial homogeneity, it is necessary to extend the Gaussian model. As it has been previously shown, the product of two random variables (ignoring the additive noise power component) corresponding to the speckle and the texture components, is the most natural way to model the pixel variability. Where the speckle contribution is often described as a vector whose components are jointly complex Gaussian, the texture term can be modelled in several ways depending on the characteristics of the imaged scene and the mathematical complexity of the statistical model applied [82].

The classical ways to describe the texture component of the clutter are: the Lognormal, the Weibull and the Gamma models. In the Lognormal model, the texture term is described utilising a Gaussian random variable. The main advantage of this approach is the simplification of the mathematical complexity due to invariance of the Gaussian distribution under linear transformation.

In the Weibull model the spatial component is simulated as a Weibull random variable. This approach is well suited for describing clutter from quasi-homogenous scene such as region of grass. The main disadvantage is the necessity of numerical techniques required for its statistical analysis.
The Gamma model is often used for the description of clutter in polarimetric SAR applications [67,68]. The main advantages are the capability to express in closed form its statistical distributions (i.e. probability density function and cumulative distribution function) and

at the same time to be capable of describing quasi-homogeneous scene. Indeed for the spatial resolution involved in civilian microwave remote sensing, the radar will often image scene in which the spatial characteristics will gently modulate the Gaussian statistics of the backscattered echo. Applying the Gamma model, the feature vector of a polarimetric SAR is modulated by a random variable g in the following way:

$$\vec{Z} = \sqrt{g}\,\vec{X} \qquad 4.78$$

where the probability density function of g is:

$$F(g) = \frac{1}{\bar{g}}\left(\frac{g}{\bar{g}}\right)^{(v-1)} \frac{1}{\Gamma(v)} \exp\left(-\frac{g}{\bar{g}}\right) \qquad 4.79$$

with Γ being the Gamma function. V and $\bar{g}$ are two parameters of the distribution directly related to the mean and variance of g. Applying the recurrence formulas of the Gamma function, the following results are obtained:

$$< g > = \bar{g}\, v \qquad 4.80$$

$$< g^2 > = \bar{g}^2\, v(v+1) \qquad 4.81$$

In the above multiplicative model, it is intrinsically assumed that the multiplicative factor due to the texture contribution affects in a similar way each components of the feature vectors. A vectorial description of g would seem more general. However the scalar simplification has been often supported from experimental data [83]. In order to compute the probability density function of the vector Z, it is necessary to formulate the conditional probability density function of Z with respect to g.

Since the feature vector X has a joint complex Gaussian probability density function , it follows that:

$$F(\vec{Z}/g) = \frac{1}{(\pi g)^3 |\Sigma|} \exp[-\frac{\vec{Z}^+ \Sigma^{-1} \vec{Z}}{g}] \qquad 4.82$$

Due to the knowledge of F(g), the unconditional probability density function $F(\vec{Z})$ is computed [83]:

$$F(\vec{Z}) = \int_0^\infty F(\vec{Z}/g)\, F(g)\, dg = \frac{2K_{3-v}\left(2\sqrt{\frac{\vec{Z}^+ \Sigma^{-1} \vec{Z}}{\bar{g}}}\right)}{\pi^3 \bar{g}^v \Gamma(v) |\Sigma| \left(\bar{g}\, \vec{Z}^+ \Sigma^{-1} \vec{Z}\right)^{\frac{(3-v)}{2}}} \qquad 4.83$$

where K_{3-v} is the modified Bessel function of order 3-v. The above distribution is also called the generalised K-distribution.

The previous analysis gives an analytical tool to study quasi-homogeneous clutter. It is interesting to calculate the effect of the presence of spatial variability of the scattering properties of the imaged scene on the span image intensity. According to the Gamma model, the intensity y can be expressed in the following way:

$$y = g\,[S_{HH}^*, \sqrt{2}\, S_{HV}^*, S_{VV}^*] \begin{bmatrix} 1 & 0 & 0 \\ 0 & 1 & 0 \\ 0 & 0 & 1 \end{bmatrix} \begin{bmatrix} S_{HH} \\ \sqrt{2}\, S_{HV} \\ S_{VV} \end{bmatrix} \qquad 4.84$$

The variance to mean square ratio of y can be simply calculated under the assumption that g and X are statistically independent:

$$\frac{var\,(y)}{\langle y \rangle^2} = \frac{\langle g^2 \rangle}{\langle g \rangle^2} \frac{var\,(|\vec{X}|^2)}{\langle |\vec{X}|^2 \rangle^2} + \frac{var\,(g)}{\langle g \rangle^2} \qquad 4.85$$

Setting $\bar{g}$ equal to 1/v in order to have unit mean of g in the Gamma model, the variance to mean square ratio becomes:

$$\frac{\text{var}(y)}{\langle y \rangle^2} = \frac{v+1}{v} \frac{\sum_{i=1}^{3} \lambda_i^2}{\left(\sum_{i=1}^{3} \lambda_i\right)^2} + \frac{1}{v} \qquad 4.86$$

where the ratio involving the eigenvalues of the Covariance matrix is associated with the speckle contribution of the polarimetric SAR. In the most general case, for the generalised span image, the eigenvalues will corresponds to the product of the weighting matrix A with the Covariance matrix Σ. It is straightforward to demonstrate using the Lagrange multiplier technique, that also in the case of Gamma model the optimal weighting matrix is Σ^{-1}. The first conclusion to be drawn from the above expression is that the parameter v is now involved in the variability of the pixel intensity. To understand the physical meaning of v, it is necessary to relate it with the log standard deviation of the texture random variable (i.e. σ_t) defined as follow:

$$\sigma_t = \sqrt{\text{var}\,(10\log_{10} g)} \qquad 4.87$$

In the table below, typical values of σ_t applicable to a 33 GHz SAR operating with a single look spatial resolution of 0.3 meters, and the corresponding Gamma parameter v are shown [68]:

Gamma parameter versus log standard deviation of the texture	
σ_t	v
1.0	19.3
1.5	8.9
2.0	5.2
2.5	3.5
3.0	2.6

TABLE 6

The Gamma parameter is therefore an indirect measure of the imaged scene spatial homogeneity. Indeed, large values of v correspond to small log standard deviation of the texture random variable and consequently to a limited spatial variation of scattering properties of the surface, where small values of v are of interest in area with large spatial variation of scattering properties.

In order to estimate the effect of the texture random variable on the pixel intensity variabilty, it is necessary to compute the standard deviation to mean ratio of the span image pixel intensity for the following cases:

1) SAR with single polarisation channel:

$$\frac{sd\,(y)}{\langle y \rangle} = \sqrt{1 + \frac{2}{v}} \qquad 4.88$$

2) multipolarisation SAR with the following clutter properties:

$$\langle |S_{HH}|^2 \rangle = \langle |S_{VV}|^2 \rangle = 2 \langle |S_{HV}|^2 \rangle \; ; \; |\gamma| = 0$$
$$\Downarrow \qquad 4.89$$
$$\frac{sd\,(y)}{\langle y \rangle} = \sqrt{\frac{v+4}{3\,v}}$$

The Gamma parameter plays a strong role in the overall variability of the pixel intensity. A scene with large spatial variation of the scattering properties will generate random variation of the intensity not predictable with the traditional Gaussian clutter model. Furthermore, the effect of averaging polarisation channels, to reduce the statistical fluctuations of the pixel intensity, will not be very beneficial in the presence of scenes characterised by large textural variations.

Plotting the standard deviation to mean ratio of the pixel intensity, we obtain:

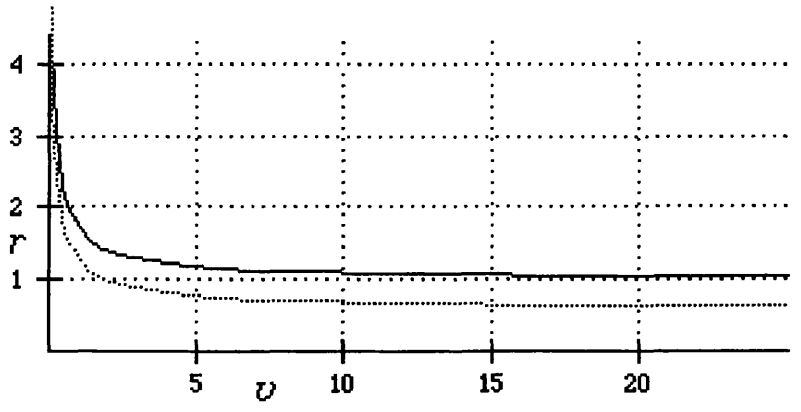

Fig.4.2 Standard deviation to mean ratio of the pixel intensity versus the Gamma parameter for SAR with single polarisation channel (normal line) and multipolarisation SAR (dotted line)

The first conclusion to be drawn from the figure above, is that the texture random variable has a direct impact on the pixel variability. Indeed for the single polarisation channel SAR, unless the imaged area is spatially very homogeneous (i.e. large v), it is not possible to obtain the unitary ratio predicted by the exponential distribution of the intensity. For the multipolarisation case, with the selected clutter assumption (the chosen clutter could be seen as the result of the application of the optimal weighting matrix), the ratio will asymptotically approach the $\sqrt{1/3}$ value corresponding to the merging of the three uncorrelated polarisation channel intensities.

The use of the Covariance matrix in the analysis of multipolarisation SAR data has shown very interesting potentials. In order to verify the validity of the previously developed theory, it is necessary to apply it to existing SAR multipolarisation data. In the next chapter, data obtained from NASA experimental airborne SAR campaigns will be used to demonstrate the suitability of the Covariance matrix in describing polarisation information.

5. EXPERIMENTAL APPLICATIONS OF THE COVARIANCE MATRIX IN SAR POLARIMETRY

5.1 *Introduction*

In the previous chapters, the theoretical background necessary to describe the multipolarisation SAR has been presented. In particular, the Covariance matrix has been demonstrated to be a very useful tool for the interpretation of multipolarisation SAR data. The eigenvalues of the Covariance matrix of a multipolarisation SAR image can be associated with fundamental properties of the imaged area such as the randomness of the scene and the span image texture. The overall backscattered power behaviour versus transmit and receive antenna polarisations is determined by the eigenvalues of the Covariance matrix.

The direct relation between the elements of the Covariance matrix and physical quantities of the backscattered radiation simplify the interpretability of this second order descriptor. The correlations between copolar and crosspolar channels appearing in each matrix element can be related to the capability of the imaged surface in generating polarised or unpolarised backscattered radiation.

In order to properly retrieve the backscattered electromagnetic field, it is important to recognise, and when necessary to estimate, the effect of sensor anomalies such as poor signal-to-noise ratio, limited antenna polarisation isolation, lack of instrument reciprocity and the effect of ambiguity noise on the polarisation channels. Several multipolarisation airborne SAR campaigns have provided useful data in different frequency bands to allow the scientific community to

validate backscattering models and to finalise the definition of multipolarisation spaceborne SARs.

The main objectives of this chapter are to analyse multipolarisation airborne SAR images utilising the Covariance matrix descriptor in order to experimentally demonstrate its usefulness, to show some critical design aspects of spaceborne multipolarisation SARs and to propose an innovative technique to process raw data in order to improve the sensor performances.

5.2 *Analysis of multipolarisation airborne SAR data using the Covariance matrix descriptor*

The role of the eigenvalues of the Covariance matrix in the analysis of multipolarisation SAR images has been clearly demonstrated in the previous chapter. Due to the use of the unitary similarity transformation and to the selected feature vector definition, the trace of the Covariance matrix is invariant under any polarisation basis transformation and the minimum eigenvalue is the lowest bound of the copolarised backscattered power (for the crosspolarised power a factor 1/2 should be introduced). The lowest eigenvalue is therefore an indicator of the potential of the imaged surface to generate a backscattered radiation with minimum polarised content.

In order to demonstrate the physical meaning of the lowest eigenvalue of the Covariance matrix, airborne data were analysed from the JPL SAR airborne campaigns. The relevant sensor specifications of the NASA CV990 were described in TABLE 5. This multipolarisation L-band SAR provided useful data capable to stimulate the interest of the user community. The processing of the four polarisation channels was performed on ground after the raw data were digitally recorded on-board at a rate of 40 MBPS. After simultaneous processing of the four polarisation channels, the synthesis of arbitrarily polarised images was produced. Due to a

compression technique that exploited the properties of the Stokes scattering operator, it was possible to reduce the synthesis time of an image of 1024 x 1024 pixels by a factor of 12 approximately [84].

Unfortunately in July 1985, during an aborted take off, the CV990 was destroyed by fire together with its instrumentation. Due to the large interest shown by the user community and the necessity of realising technology development of direct relevance with future planned spaceborne SAR missions, NASA decided to realise another airborne multipolarisation SAR with multifrequency capability to be flown on a DC-8 aircraft. The sensor had the following specifications [85]:

NASA DC-8 SAR SPECIFICATIONS			
	C-band	L-band	P-band
frequency (MHz)	5300	1250	440
pulse length (us)	11.25	11.25	11.25
bandwidth (MHz)	19	19	19
peak power (W)	1000	6000	1000
altitude (Km)		4.5 - 12.2	
PRF (Hz)		250 - 750	
look angle (degree)		20 - 70	
slant range pixel spacing (m)		6.67	
azimuth pixel spacing (m)		3.03 (single look)	
aircraft velocity (m/s)		257	

TABLE 7

The simultaneous utilisation of three carrier frequencies, together with the fully multipolarisation capability generated an instantaneous data rate of 2.1 Gigabits per second. The overall processing of the twelve polarisation channels was performed on ground with the use of a microcomputer and the help of an array processor. The size of

the four azimuth look image was 750 x 1024 pixels, and at each frequency it was possible to synthesise any desired polarisation with the help of the four coherent channels.

In order to extract the eigenvalues of the Covariance matrix from the airborne SAR images available from JPL in compressed Stokes scattering operator format, it was necessary to develop a software tool capable to obtain the Covariance matrix from a chosen set of pixels and then to compute the associated eigenvalues. Modifying some existing software capable to operate on the JPL data format, the Covariance matrix was calculated for any arbitrary area size.

Few subroutines necessary for calculating the eigenvalues and the eigenvectors of an hermitian matrix, were obtained by NETLIB, a software library from USA. These subroutines calculate the eigenvalues after transforming the Covariance matrix into a real symmetric matrix with the use of an unitary transformation. The lowest eigenvalue obtained was normalised to the overall sum in order to bound its value between zero and one, and with the use of PV-WAVE image processing software, a grey level image was generated of 32 x 32 pixel size. The largest pixel value (one) was associated to white with the lowest one (zero) to black.

Together with the Covariance matrix software, was also utilised a polarisation synthesis software called Poltool, capable to generate copolar and crosspolar polarisation signatures directly from data in the compressed Stokes scattering operator format [84]. The main interest in using polarisation signatures was to validate the information retrieved from the eigenvalues of the Covariance matrix. As consequence of the utilisation of Poltool, the height of the signature pedestal and the coefficient of variation, defined as the ratio between the minimum and maximum received powers, was calculated for each selected signature.

The chosen airborne SAR data for the polarisation analysis were from three different areas: San Francisco bay (containing urban, ocean and vegetation areas), Amazonian rain forest and Flevoland agricultural fields in The Netherlands. The data from San Francisco bay were obtained from the NASA CV990 campaign and therefore only available at L-band. The data were provided in four azimuth look format with a corresponding pixel spacing of about 11 metres both in range and azimuth dimensions. The remaining data were collected by the NASA DC-8 SAR and therefore were available at three different frequencies (i.e. P, L and C-bands) with similar format to the previous ones. Investigation of statistical homogeneous images shown that because of the effect of speckle correlation, the corresponding number of effective looks was 2.6 [86].
The areas of 32 x 32 pixel size were chosen with incendence angles shown in the table below:

type of area	image number	incidence angle [degree]	image coordinate in JPL format
ocean	1	27	(146, 86)
	2	49	(34, 428)
urban	3	28	(361, 145)
	4	49	(113, 426)
rain forest (P-band)	5	24	(176, 44)
	6	51	(175, 317)
rain forest (L-band)	7	25	(164, 60)
	8	51	(167, 307)
rain forest (C-band)	9	24	(184, 38)
	10	51	(151, 305)
agricultural field (P-band)	11	22	(160, 46)
	12	51	(116, 310)
agricultural field (L-band)	13	21	(159, 46)
	14	52	(115, 311)
agricultural field (C-band)	15	22	(158, 46)
	16	52	(116, 310)

TABLE 8

The choice of the area size was driven from the need to preserve fundamental scattering characteristics and to decrease the speckle contribution in the calculation of the polarisation signature. Examples of the utilised SAR images are shown in the following figures for

transmit and receive horizontal polarisations configurations (i.e. HH polarisation).

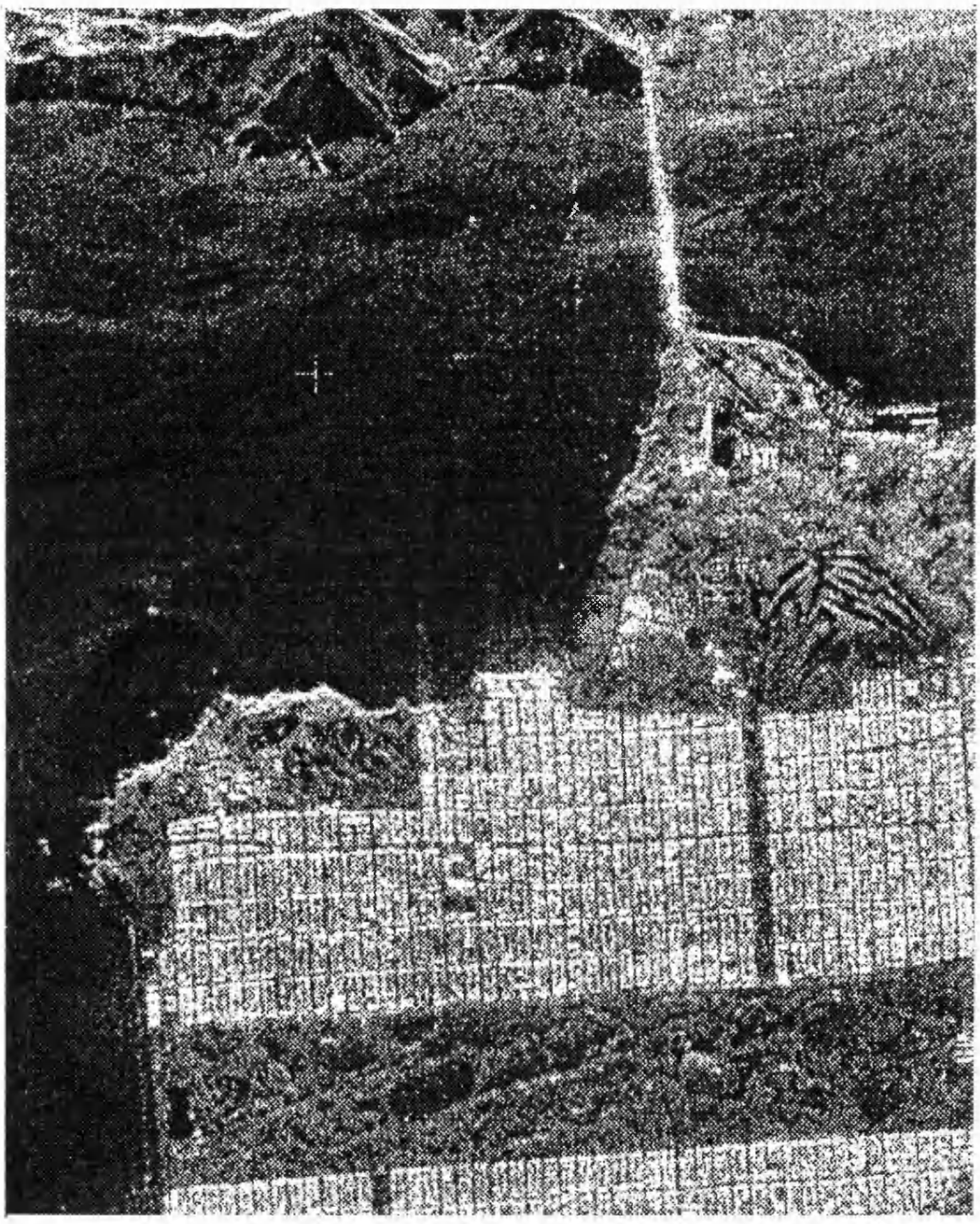

Fig.5.1 SAR image of San Francisco region, L-band, HH polarisation

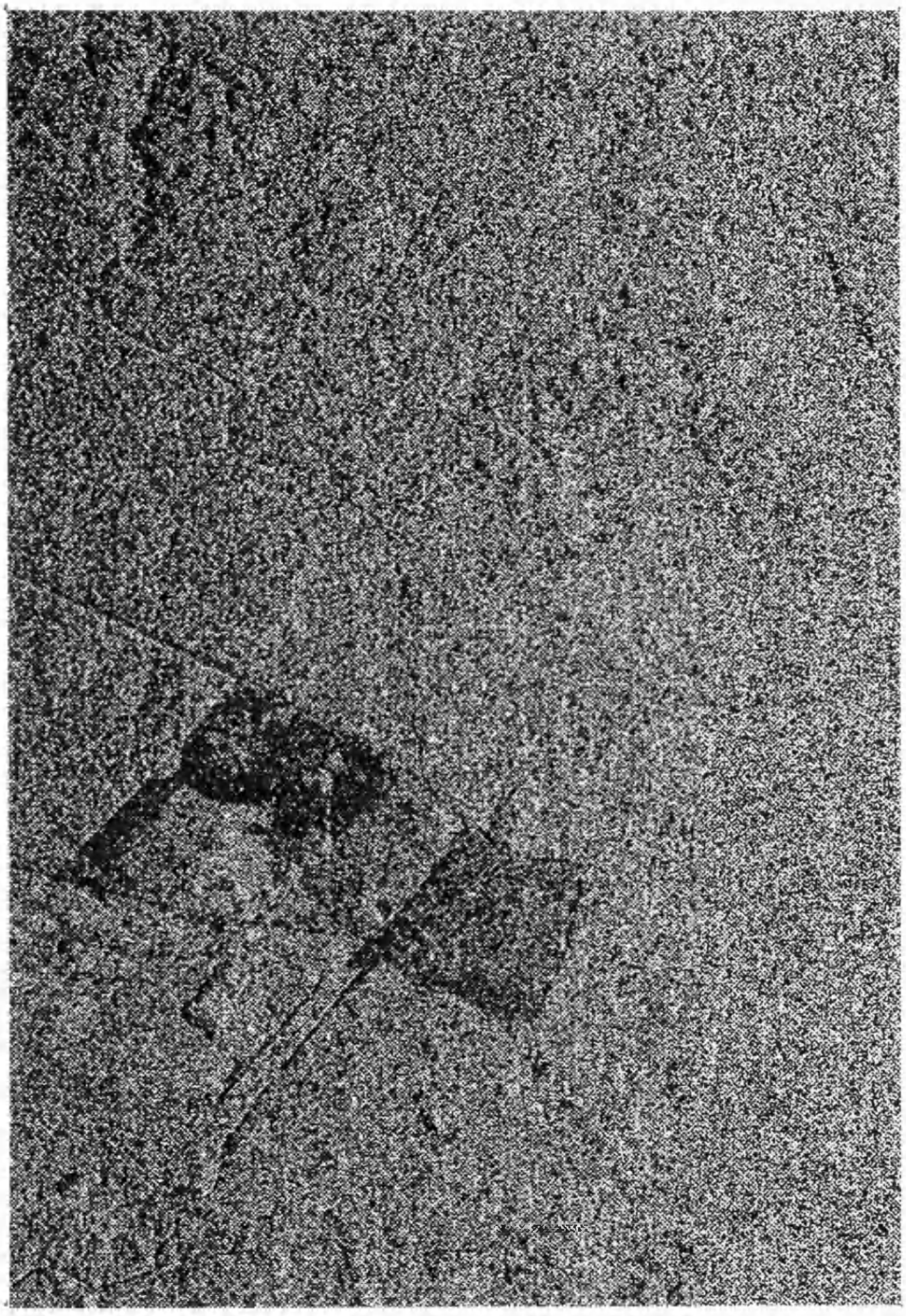

Fig.5.2 SAR image of Amazonian rain forest, C-band, HH polarisation

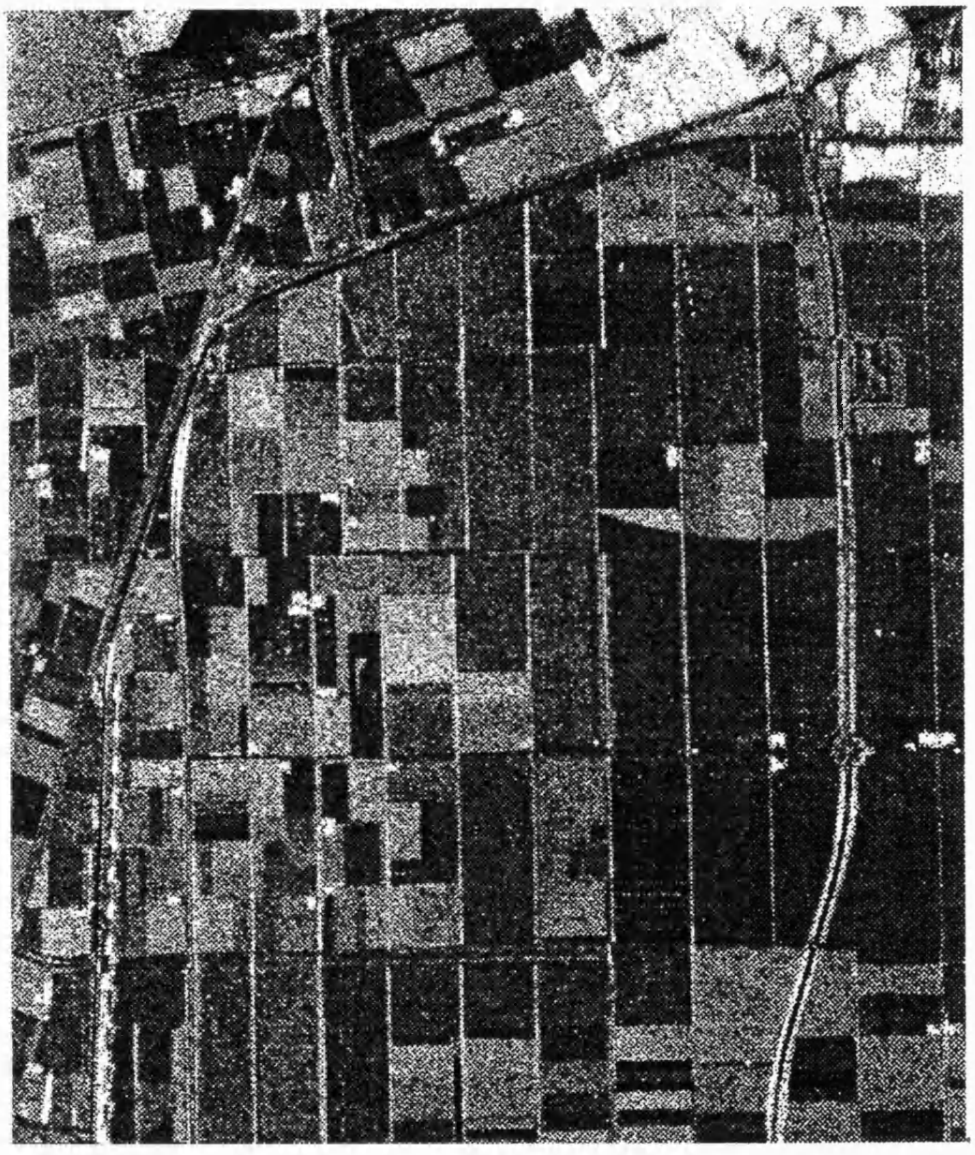

Fig.5.3 SAR image of Flevoland agricultural fields, P-band, HH polarisation

According to the classification shown in Table 8, the grey level images displaying the normalised minimum eigenvalue of the Covariance matrix and the corresponding copolar and crosspolar polarisation signatures are presented in the following figures.

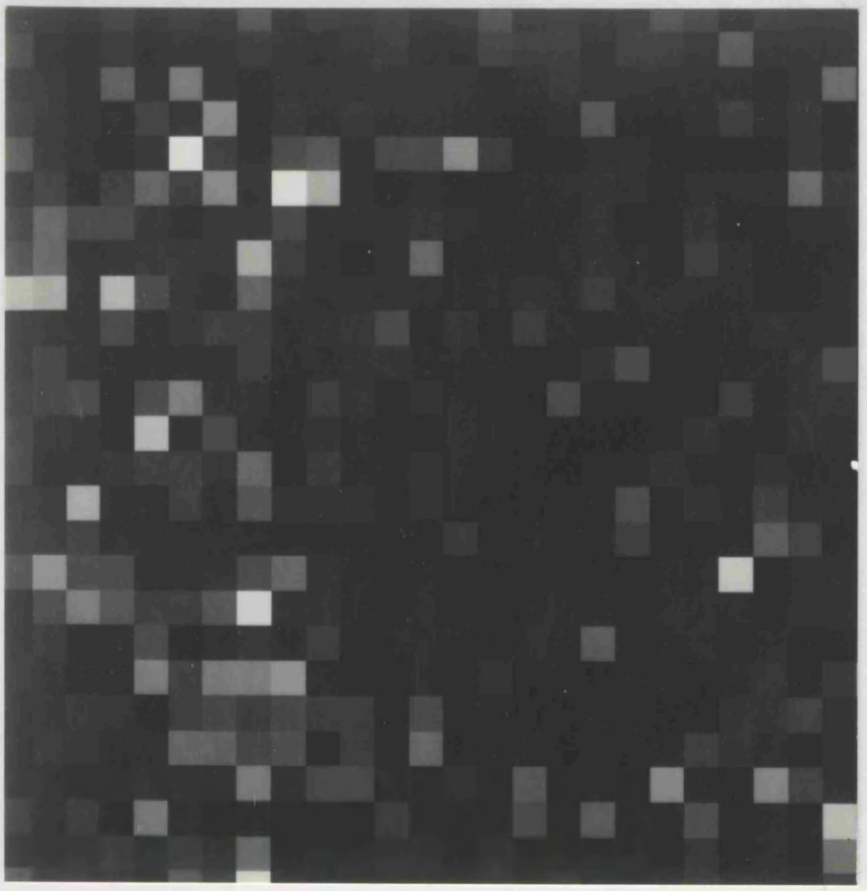

A

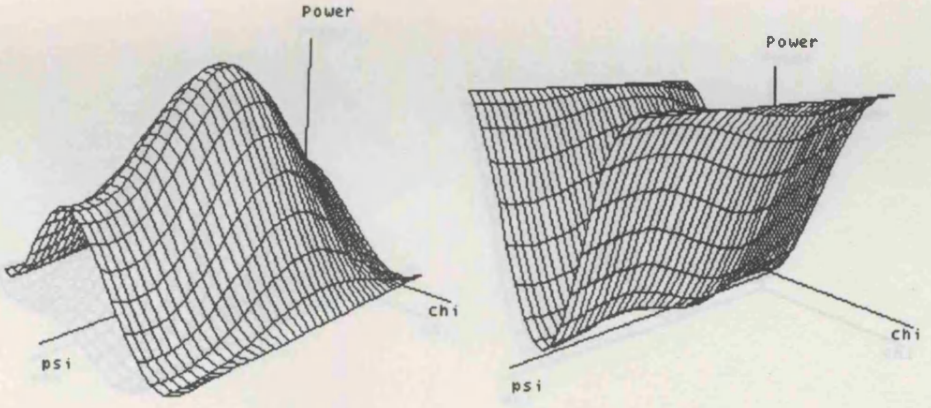

B

Fig.5.4 Minimum eigenvalue (A) and polarisation signatures (B), image 1, ocean region, L-band, 27 degrees incidence angle

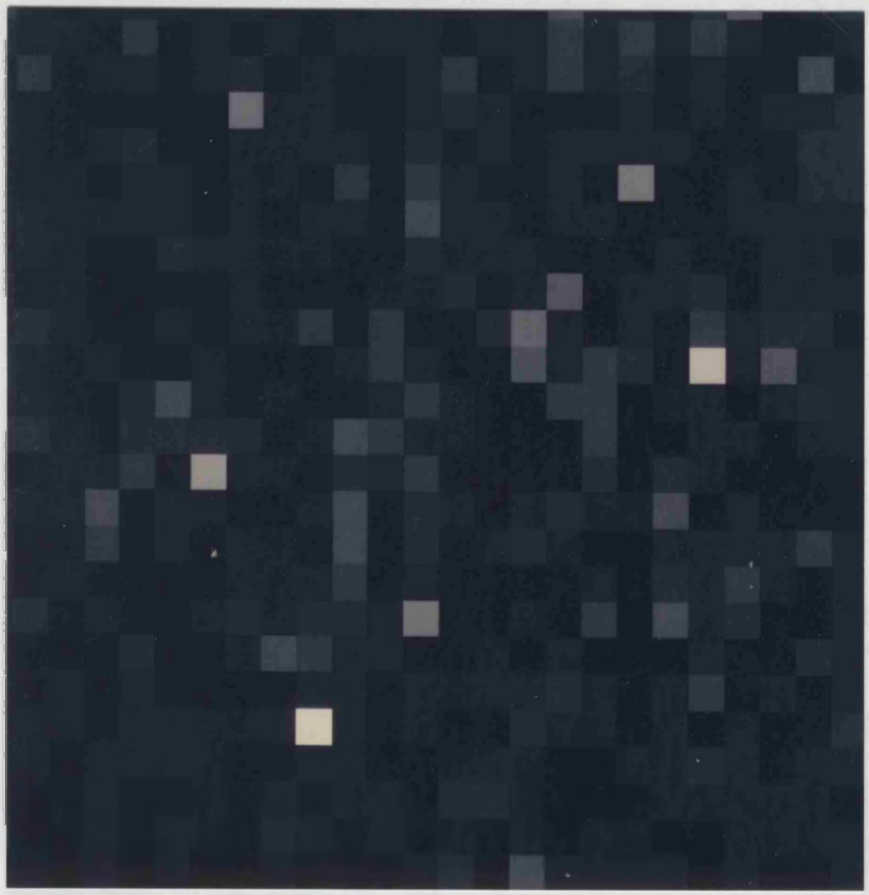

A

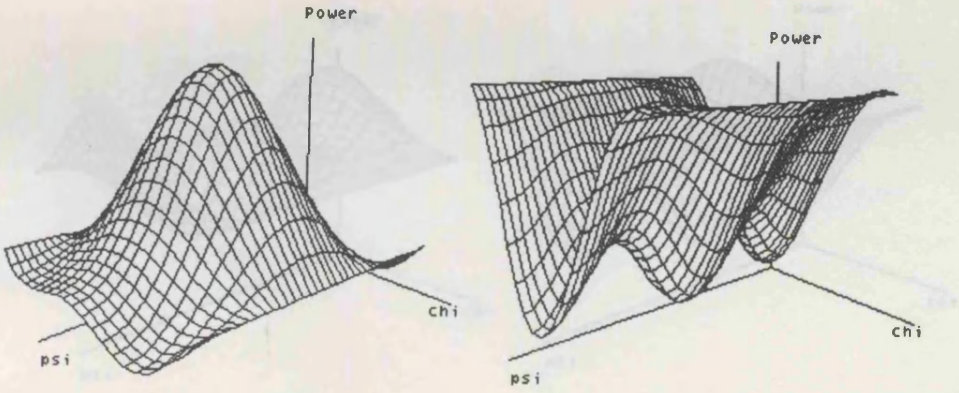

B

Fig.5.5 Minimum eigenvalue (A) and polarisation signatures (B), image 2, ocean region, L-band, 49 degrees incidence angle

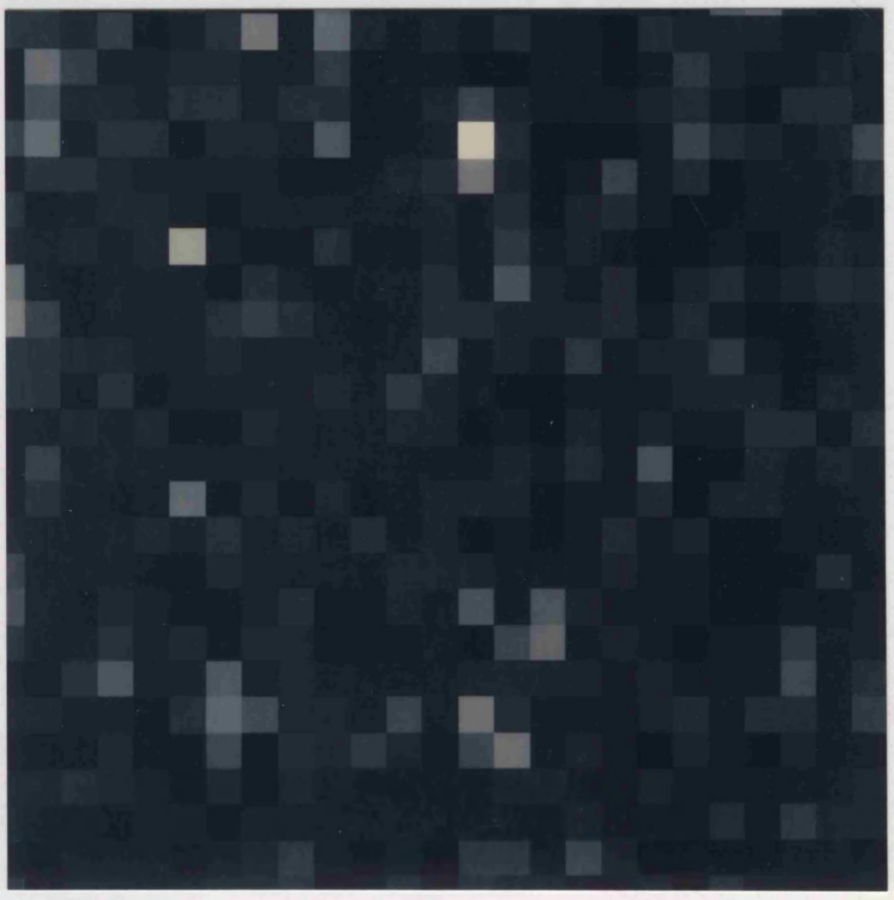

A

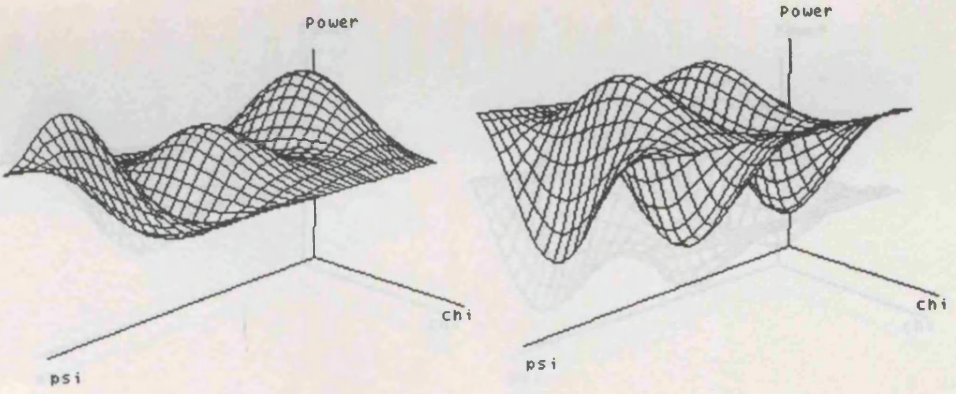

B

Fig.5.6 Minimum eigenvalue (A) and polarisation signatures (B), image 3, urban region, L-band, 28 degrees incidence angle

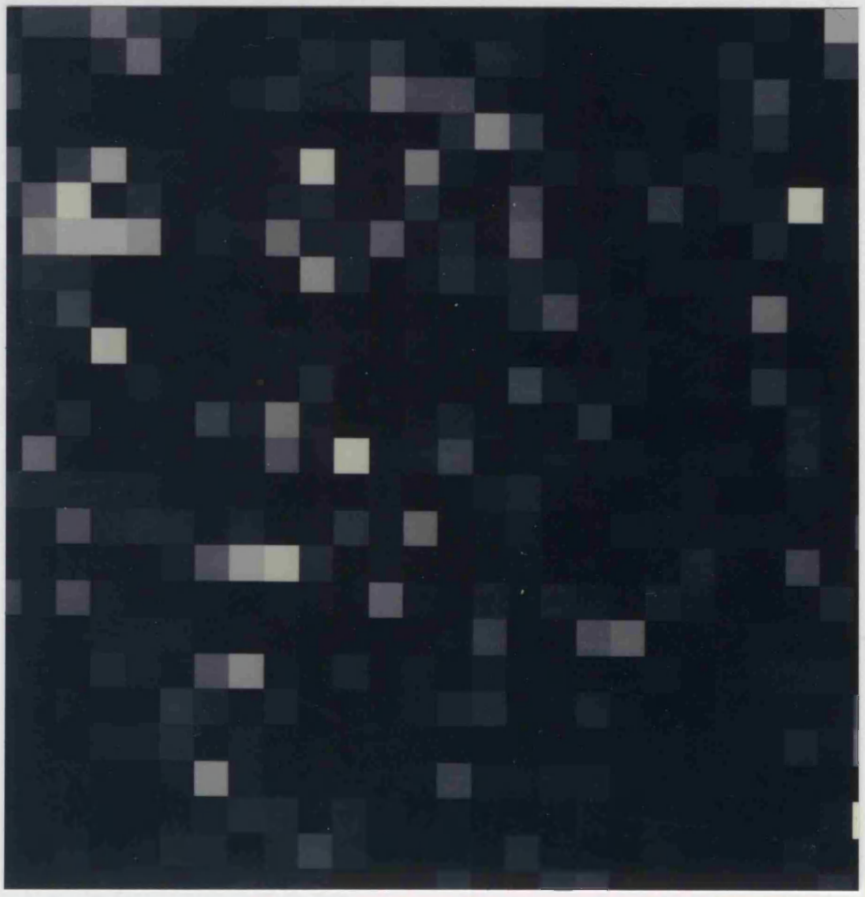

A

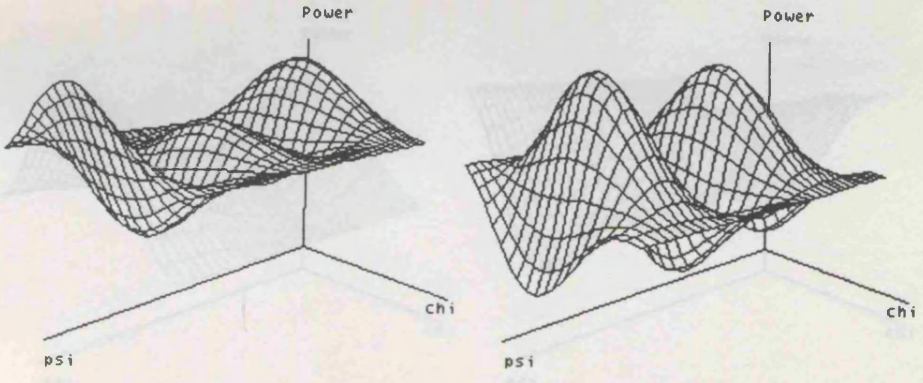

B

Fig.5.7 Minimum eigenvalue (A) and polarisation signatures (B), image 4, urban region, L-band, 49 degrees incidence angle

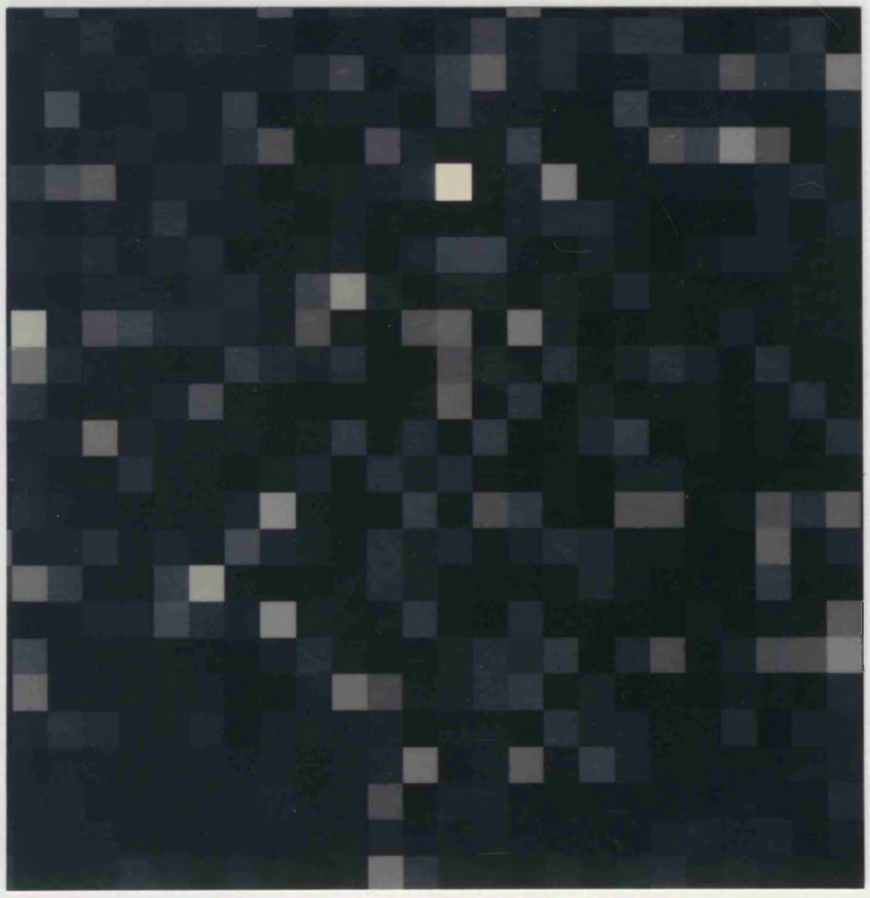

A

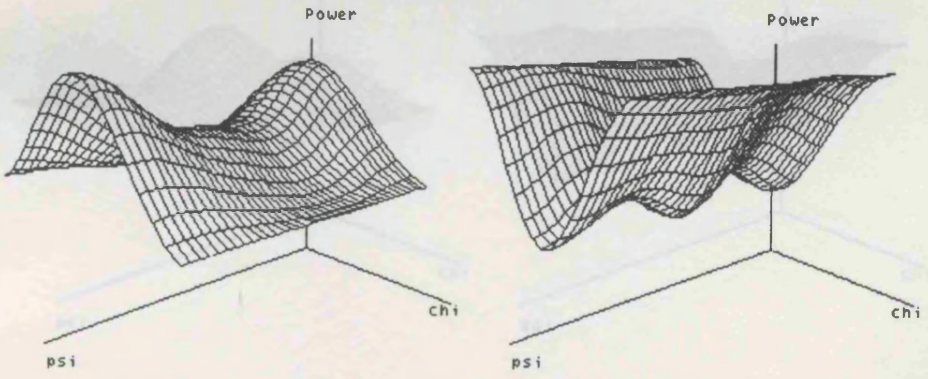

B

Fig.5.8 Minimum eigenvalue (A) and polarisation signatures (B), image 5, rain forest, P-band, 24 degrees incidence angle

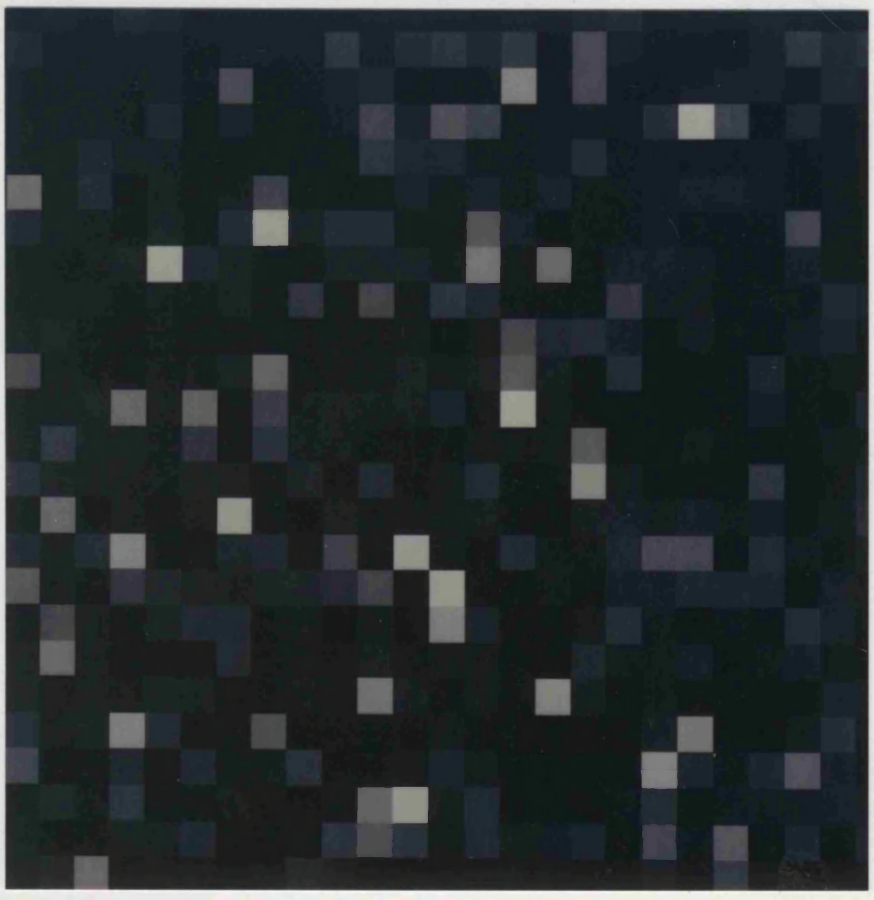

A

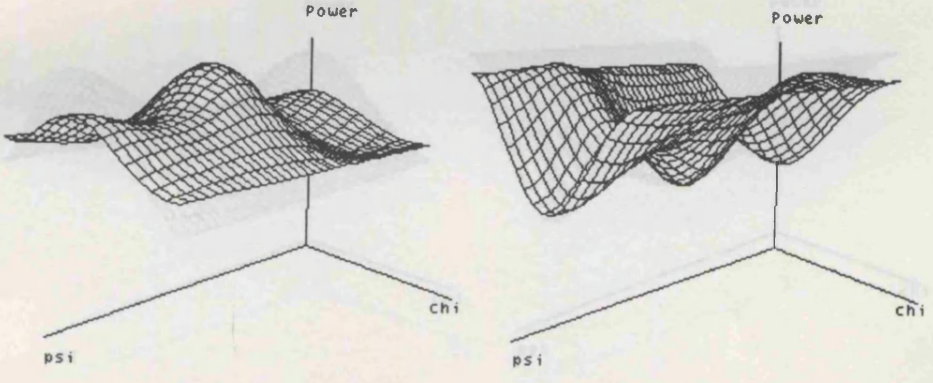

B

Fig.5.9 Minimum eigenvalue (A) and polarisation signatures (B), image 6, rain forest, P-band, 51 degrees incidence angle

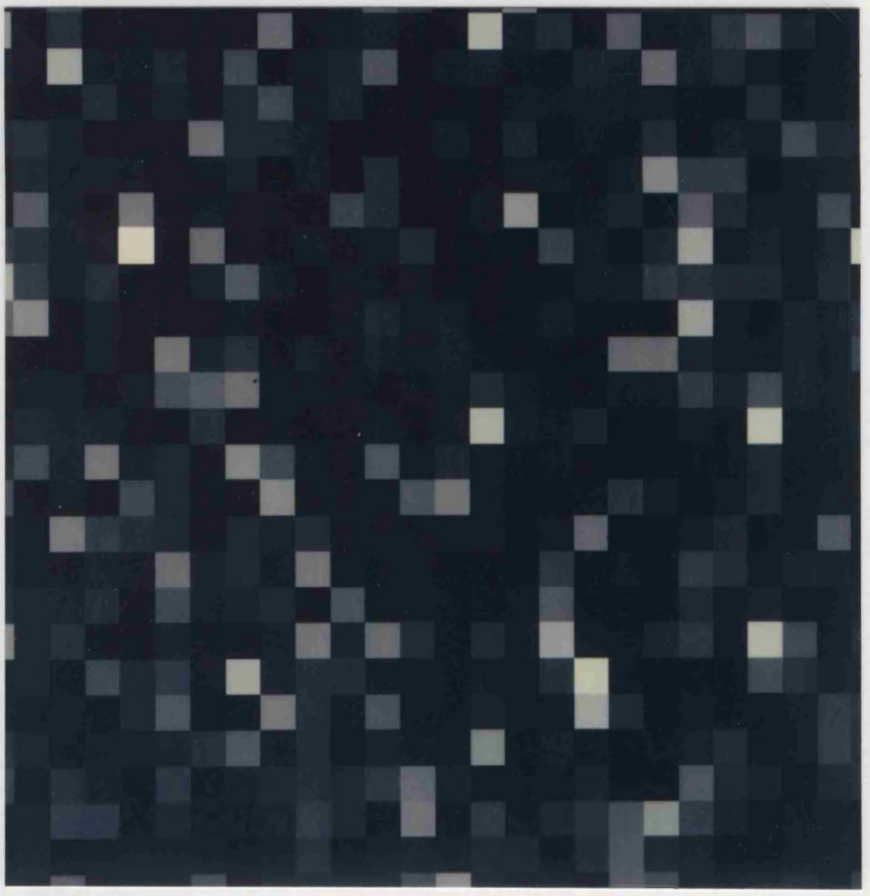

A

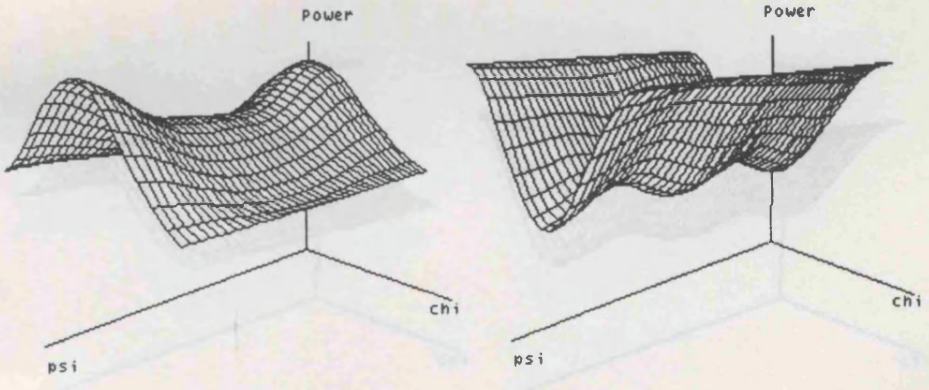

B

Fig.5.10 Minimum eigenvalue (A) and polarisation signatures (B), image 7, rain forest, L-band, 25 degrees incidence angle

A

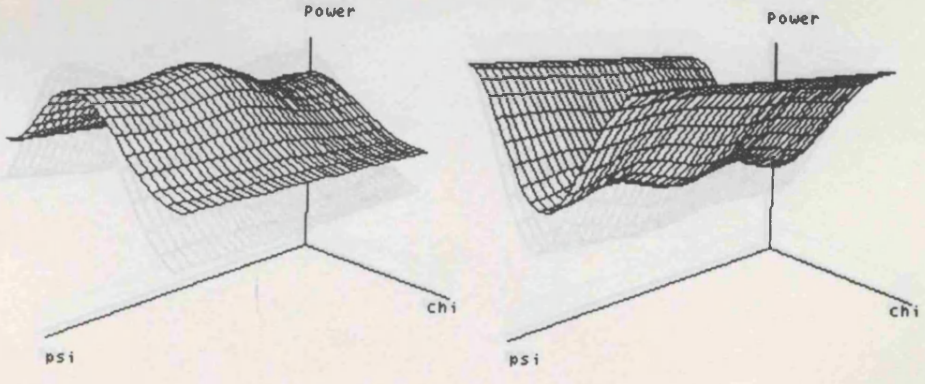

B

Fig.5.11 Minimum eigenvalue (A) and polarisation signatures (B), image 8, rain forest, L-band, 51 degrees incidence angle

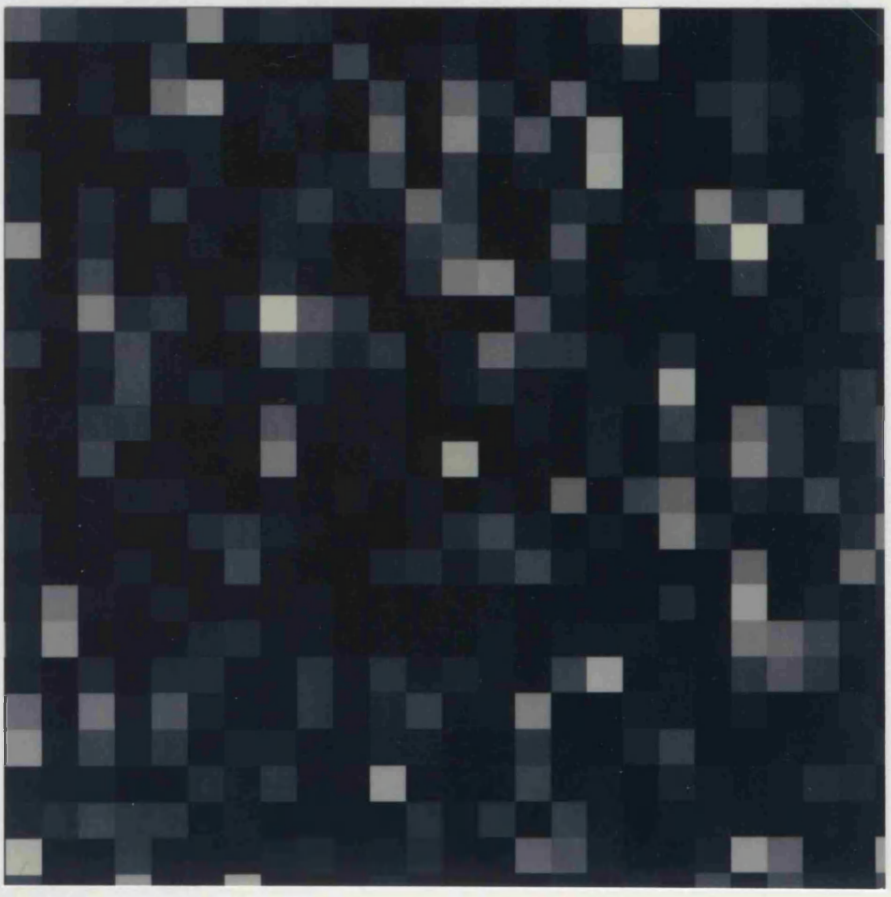

A

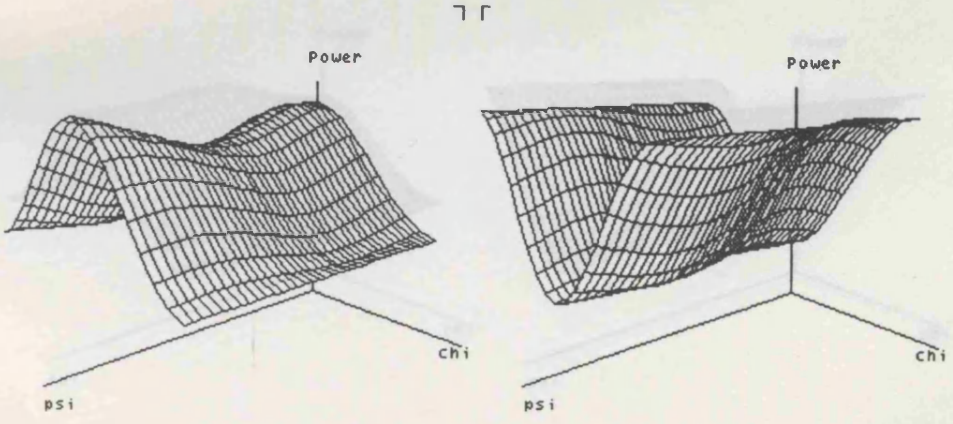

B

Fig.5.12 Minimum eigenvalue (A) and polarisation signatures (B), image 9, rain forest, C-band, 24 degrees incidence angle

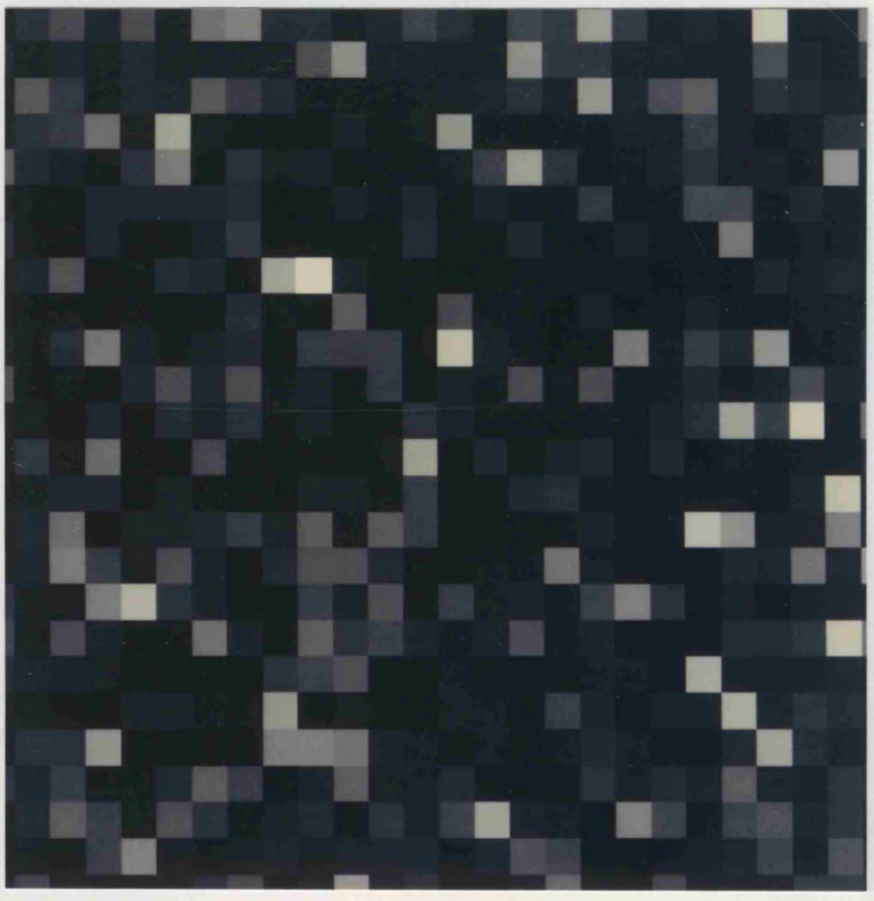

A

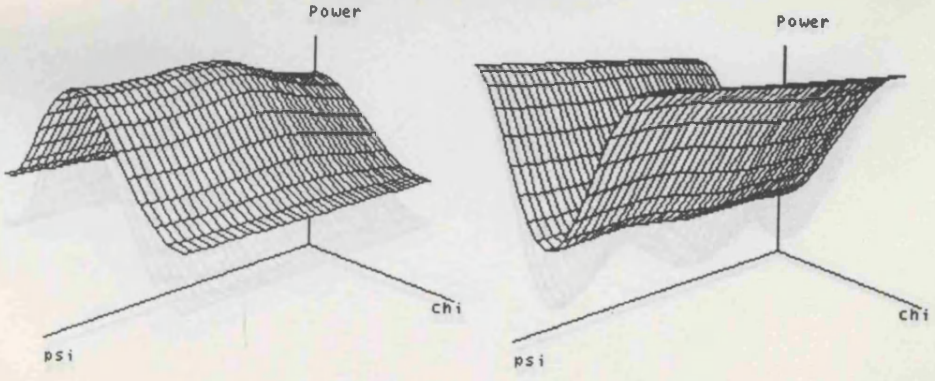

B

Fig.5.13 Minimum eigenvalue (A) and polarisation signatures (B), image 10, rain forest, C-band, 51 degrees incidence angle

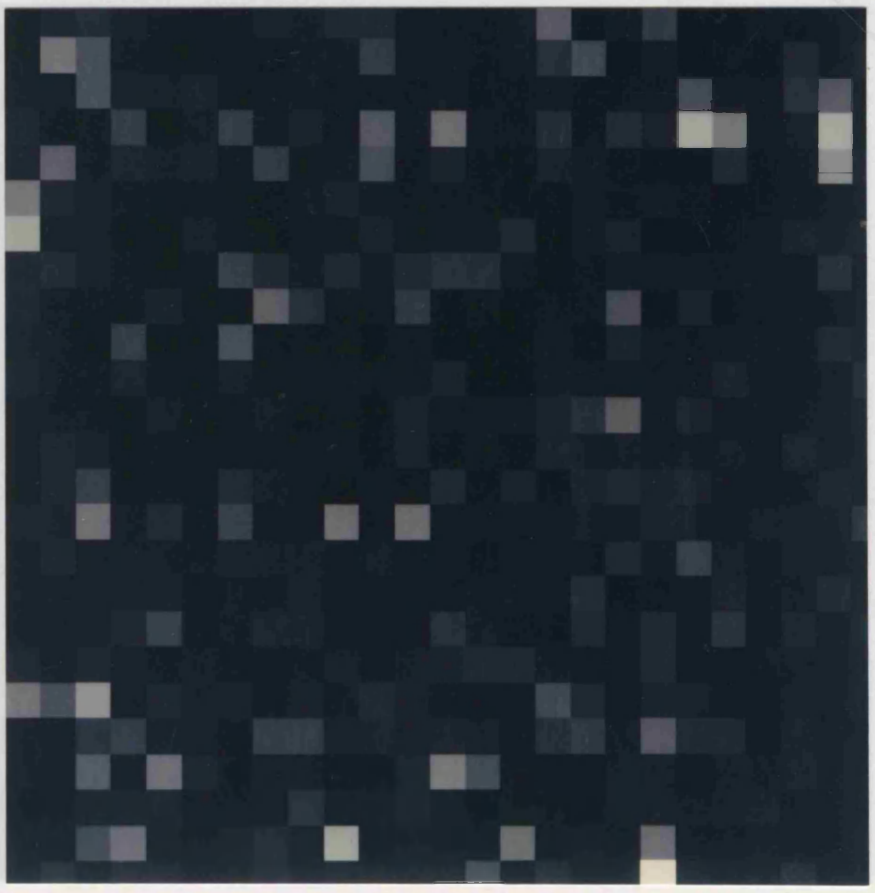

A

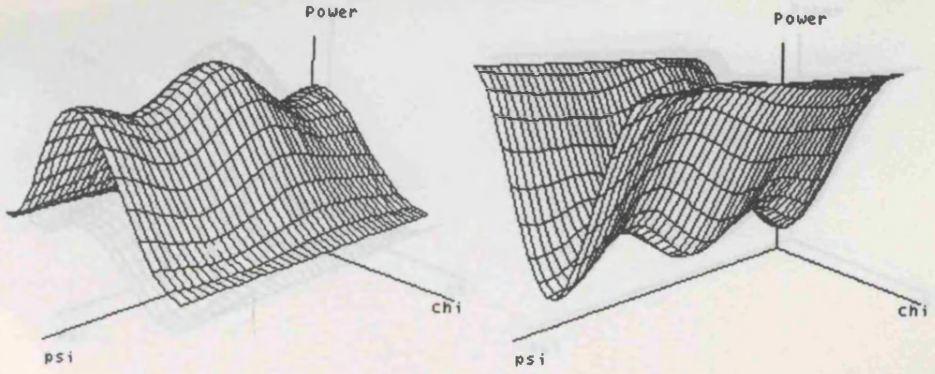

B

Fig.5.14 Minimum eigenvalue (A) and polarisation signatures (B), image 11, agricultural fields, P-band, 22 degrees incidence angle

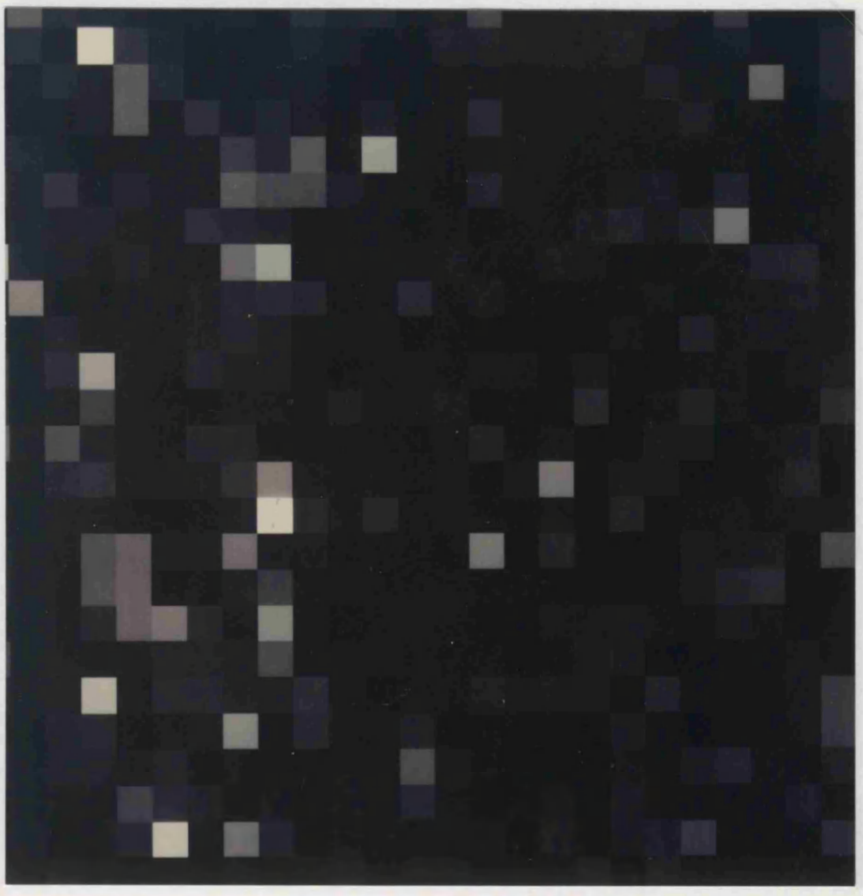

A

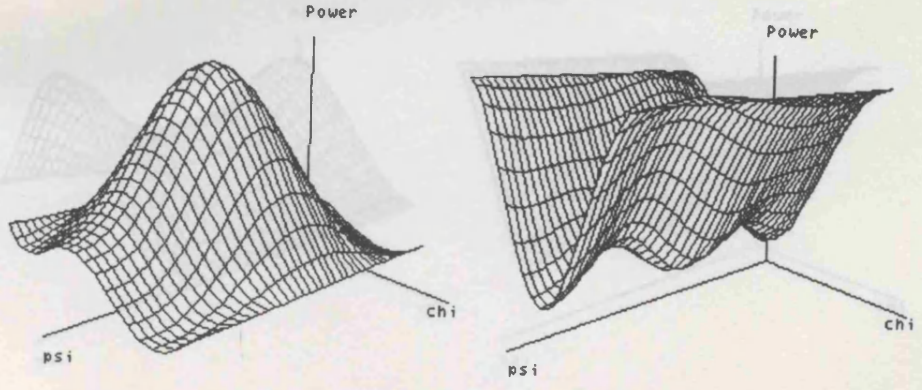

B

Fig.5.15 Minimum eigenvalue (A) and polarisation signatures (B), image 12, agricultural fields, P-band, 51 degrees incidence angle

A

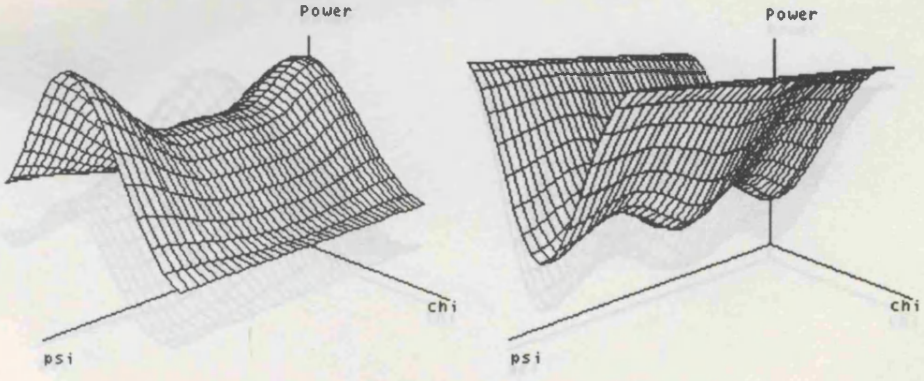

B

Fig.5.16 Minimum eigenvalue (A) and polarisation signatures (B), image 13, agricultural fields, L-band, 21 degrees incidence angle

A

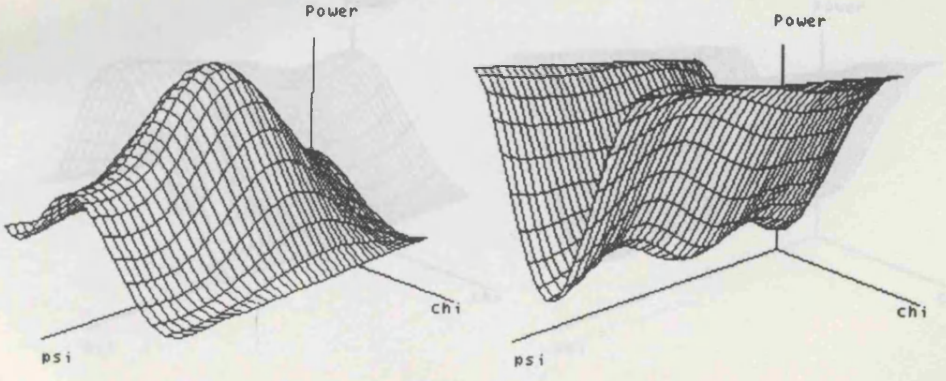

B

Fig.5.17 Minimum eigenvalue (A) and polarisation signatures (B), image 14, agricultural fields, L-band, 52 degrees incidence angle

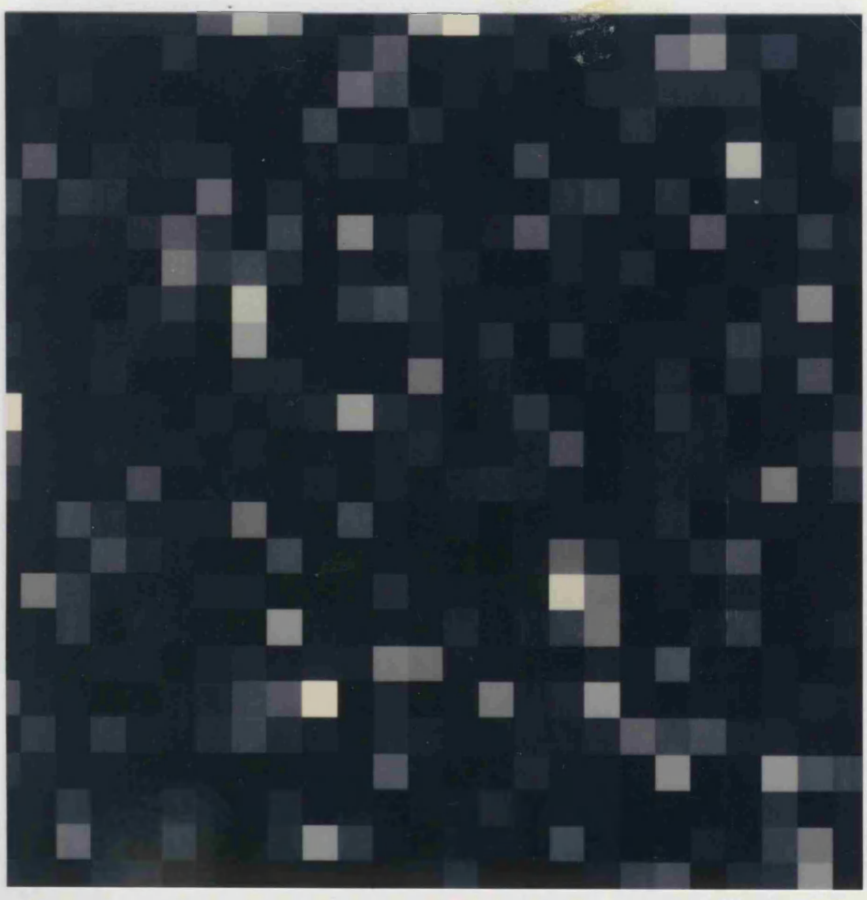

A

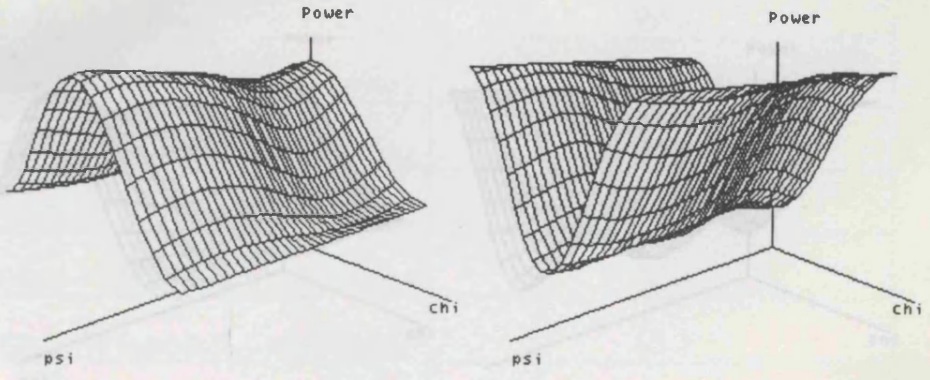

B

Fig.5.18 Minimum eigenvalue (A) and polarisation signatures (B), image 15, agricultural fields, C-band, 22 degrees incidence angle

A

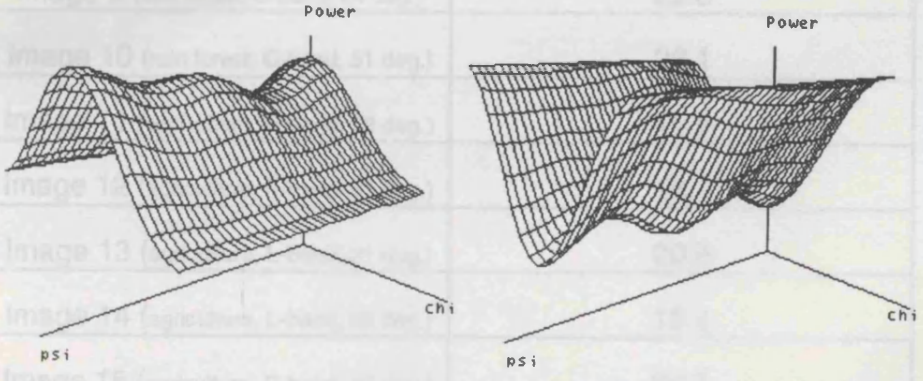

B

Fig.5.19 Minimum eigenvalue (A) and polarisation signatures (B), image 16, agricultural fields, C-band, 52 degrees incidence angle

In order to give a quantitative measure of the grey level images, the sum of the minimum normalised eigenvalue for each selected area is computed. The height of the copolar and crosspolar polarisation signature pedestals together with the coefficient of variation are also calculated to compare the results obtained from the Covariance matrix with the ones of the polarisation signature (i.e. the Stokes scattering operator).

	sum of the minimum eigenvalues
Image 1 (ocean, L-band, 27 deg.)	3.4
Image 2 (ocean, L-band, 49 deg.)	4.0
Image 3 (urban, L-band, 28 deg.)	20.0
Image 4 (urban, L-band, 49 deg.)	14.6
Image 5 (rain forest, P-band, 24 deg.)	26.0
Image 6 (rain forest, P-band, 51 deg.)	30.8
Image 7 (rain forest, L-band, 25 deg.)	23.5
Image 8 (rain forest, L-band, 51 deg.)	30.4
Image 9 (rain forest, C-band, 24 deg.)	22.6
Image 10 (rain forest, C-band, 51 deg.)	28.1
Image 11 (agriculture, P-band, 22 deg.)	15.5
Image 12 (agriculture, P-band, 51 deg.)	16.2
Image 13 (agriculture, L-band, 21 deg.)	20.9
Image 14 (agriculture, L-band, 52 deg.)	16.4
Image 15 (agriculture, C-band, 22 deg.)	24.3
Image 16 (agriculture, C-band, 52 deg.)	21.9

TABLE 9

	copolar signature		crosspolar signature	
	pedestal height	coefficient of variation	pedestal height	coefficient of variation
Image 1	2.22×10^{-2}	2.18×10^{-2}	1.98×10^{-2}	1.94×10^{-2}
Image 2	2.76×10^{-2}	2.68×10^{-2}	3.32×10^{-2}	3.21×10^{-2}
Image 3	6.59×10^{-1}	3.97×10^{-1}	2.45×10^{-1}	1.97×10^{-1}
Image 4	4.42×10^{-1}	3.07×10^{-1}	1.11×10^{-1}	9.98×10^{-2}
Image 5	8.55×10^{-1}	4.61×10^{-1}	5.02×10^{-1}	3.34×10^{-1}
Image 6	1.59	6.15×10^{-1}	8.63×10^{-1}	4.63×10^{-1}
Image 7	1.11	5.26×10^{-1}	6.68×10^{-1}	4.01×10^{-1}
Image 8	1.65	6.23×10^{-1}	8.77×10^{-1}	4.67×10^{-1}
Image 9	6.57×10^{-1}	3.96×10^{-1}	4.00×10^{-1}	2.85×10^{-1}
Image 10	8.42×10^{-1}	4.57×10^{-1}	4.78×10^{-1}	3.23×10^{-1}
Image 11	3.59×10^{-1}	2.64×10^{-1}	1.45×10^{-1}	1.27×10^{-1}
Image 12	1.56×10^{-1}	1.35×10^{-1}	1.43×10^{-1}	1.25×10^{-1}
Image 13	6.25×10^{-1}	3.85×10^{-1}	3.47×10^{-1}	2.57×10^{-1}
Image 14	2.27×10^{-1}	1.85×10^{-1}	1.38×10^{-1}	1.21×10^{-1}
Image 15	5.85×10^{-1}	3.69×10^{-1}	3.02×10^{-1}	2.32×10^{-1}
Image 16	7.91×10^{-1}	4.42×10^{-1}	3.53×10^{-1}	2.61×10^{-1}

TABLE 10

The ocean data for both incidence angles show the smallest sum of lowest eigenvalues. The signature pedestal and the coefficient of variation are also very low, demonstrating a limited unpolarised component in the backscattered radiation. The presence of very low

average crosspolarised power justify the use of the first order small perturbation method for the large incidence angle, therefore due to the use of 24 cm wavelength, the imaged ocean area had a rms height of the order of few centimetres.

The very low coefficient of variation is typical of quasi-deterministic target. Indeed due to the homogeneity of the scattering behaviour among resolution cells and the dominant single reflection mechanism, the resultant average polarisation signatures maintain the nature of the elementary resolution cell before the multilook process. Alternatively, the small value of the coefficient of variation implies that it is possible to select an antenna polarisation such that the received power is practically equal to zero.

It should be emphasised that due to the high difference between copolarised and crosspolarised powers for typical ocean scattering, it is necessary to have a high degree of confidence on the calibration scheme applied. Crosstalk error might induce difference of the order of 90 % between crosspolarised powers before and after calibration [86]. It is believed that the San Francisco image was carefully calibrated by JPL.

The urban data shows an increase of the minimum eigenvalue sum for both incidence angles together with increased signature pedestal heights and coefficients of variation. The dominant scattering mechanism in the urban area is the double-bounce dihedral corner reflector type of scattering as can be seen from the polarisation signatures. However, with respect to the polarisation signature of a single dihedral corner reflector, the presence of a larger pedestal is recognised. This is caused by the increased complexity of the geometry of the reflecting buldings affecting the homogeneity of the scattering behaviour. In particular for image 3, the increased unpolarised component is associated with a relative geometry of the imaged streets oblique to the radar illumination implying a large

number of multiple bounce (i.e. larger than two) for the backscattered radiation, where in image 4 the chosen area has a square-on streets geometry. Cloude has shown that it is possible to model the urban scattering mechanism as the sum of two Covariance matrices: one corresponding to the canonical dihedral corner reflector and another with only the elements of the main diagonal different from zero (i.e. a noise matrix) [87].

Before being analysed, the two data sets corresponding to the Amazonian rain forest and Flevoland agricultural fields were carefully calibrated. The cross talk calibration was performed without relying on the presence of ground targets but only on assumptions on the clutter statistics [58]. The channel imbalance and the absolute calibrations were performed with the help of trihedral corner reflectors deployed on ground.

For the multifrequency data of the Amazonian rain forest, the interpretation of the experimental results is complicated by the increased complexity of the scattering target. Depending on the polarisation, frequency, incidence angle and local structure of the imaged forest, the backscattered radiation properties will strongly vary. In particular it has been shown that at P-band, the reflected VV and HV returns directly come from the large branches of the crown layer (with the exception of young forest where the VV return is associated with the crown-ground reflection mechanism). For the HH return at P-band, the dominant effect is the double-bounce scattering due to the trunk-ground interaction together with a strong correlation of the backscattered signal with the topography of the forest floor [88]. For the L-band case, we have a similar situation with the exception of the HH return, where it exists a component due to direct crown return, crown-ground and trunk-ground interactions. For the C-band all the returns come directly from the crown needles [55,89,90,91].

The sum of the minimum eigenvalues for the rain forest shows two main trends: an increasing contribution versus incidence angle and a reduction for shorter wavelength. The effect with respect to incidence angle has been already observed in other forest data set [90]. The main reason of this behaviour is the increased amount of multiscattering associated with larger incidence angle. The physical interpretation of the second trend is the larger depolarising contribution due to objects of larger size with respect to the illuminating wavelength. Indeed, it should be emphasised that the polarisation properties of the radar return are typically related to scatterer sizes of the order of several wavelengths.

Comparing these results with the corresponding pedestal heights and coefficients of variation, it is evident that for the L-band case there is poor agreement between the two tables. As it will be shown later, the minimum eigenvalue is not always capable to completely characterise the unpolarised component.

It is interesting to recognise how the different scattering mechanisms affect the polarisation signature. It is evident for the P-band case that the dominant double-bounce scattering, together with direct reflections from primary branches, gives a large HH return. Increasing the frequency the signatures lose the typical double-bounce shape and start to be affected from the single reflection type of mechanism.

For the case of the Flevoland agricultural fields, the sum of the minimum eigenvalues shows an increase versus frequency due to larger surface roughness. However the dependency versus incidence angle is rather more difficult to be established since the local physical characteristics of the agricultural fields vary from region to region and consequently the scattering properties as well. Indeed depending on the detailed structure of the vegetation, the water content, the ground roughness, the soil moisture and the surface topography, different

type of scattering phenomena can take place. From the analysis of the shape of the polarisation signatures, the combination of Bragg scattering and double-bounce mechanism appears to be the dominant effects in the overall phenomena.

The comparison of the correspondent pedestal heights and the coefficients of variation with the previous descriptor demonstrates that the minimum eigenvalue is not always capable to fully describe the unpolarised component of the backscattered radiation. Therefore it is necessary to introduce other information associated with the Covariance matrix to improve the characterisation of the unpolarised radiation.

To fully describe the polarisation characteristics, it is necessary to include the correlation between the two copolarised channels. The correlation information and the crosspolarised power cannot be associated with a single eigenvalue. Indeed it has been demonstrated in the previous chapter that a deterministic target will have two eigenvalues equal to zero in order to generate zero unpolarised radiation regardless of the transmit polarisation. To clarify the matter, it is interesting to show the following data taken from the L-band channel of the NASA DC-8 airborne SAR [66]:

area	λ_1	λ_2	λ_3	$\sum_{i=1}^{3} \lambda_i$
grass	0.06	0.14	0.79	3.7 dB
buildings	0.01	0.27	0.72	23.5 dB

TABLE 11

(after E.Luneburg, V.Ziegler, A.Schroth and K.Tragl, 1991)

Each eigenvalue is normalised by the total sum of the corresponding area. For both regions the first eigenvalue has vanishing value, however it is the second eigenvalue which demonstrates the quasi-

deterministic nature of the grass surface. It is interesting to note how the geometrical complexity of the urban area, independently from the selected polarisation basis, reflects in a larger sum of powers injected in the polarisation channels (actually the eigenvalues shall be seen as bounds and not necessarily as powers associated to the polarised radiation). To better characterise the unpolarised radiation content, a new coefficient is defined:(*)

$$\text{unpolarised radiation coefficient} = \frac{<|S_{HV}|^2>}{|<S_{HH}\,S^*_{VV}>|} \qquad 5.1$$

and in the following figures this is displayed for the previously selected regions. In order to obtain a quantitative interpretation, the total unpolarised radiation coefficient is calculated for each region in Table 12. Comparing the results with Table 10, a similar behaviour between the pedestal heights and the coefficients of unpolarised radiation is observed. There is not a major discrepancy between the two descriptors, in particular both for the Amazonian rain forest and the Flevoland agricultural fields the overall tendency is now respected. Therefore it can be concluded that the unpolarised radiation coefficient is capable of improving the characterisation of the signature pedestal with respect to the minimum eigenvalue, and that any kind of alternative descriptor will contain information associated with depolarisation and copolarised channels correlation. In this frame the ratio of minimum to maximum eigenvalue used by JPL is also an effective descriptor [70].

It is important to notice that in several regions, the minimum normalised eigenvalue is capable of describing the unpolarised radiation content because the depolarisation is the main source of existence of the signature pedestal. This role of the average crosspolarised power has been clearly demonstrated through the decomposition of the polarisation signature in weighting functions associated with the different elements of the Covariance matrix [92].

(*) This is not in general basis-invariant, but its validity can be extended if specific medium symmetry is involved [108].

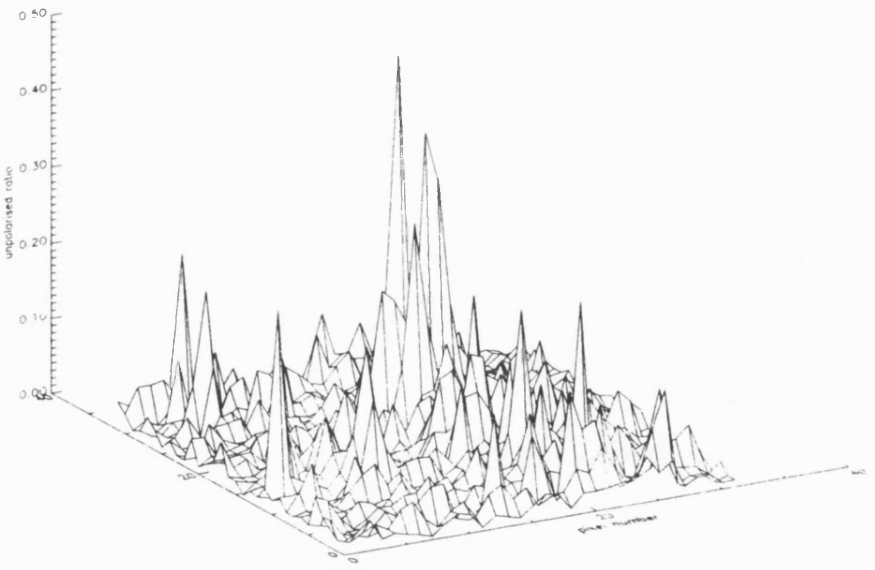

Fig.5.20 Unpolarised radiation coefficient, image 1, ocean region, L-band, 27 degrees incidence angle

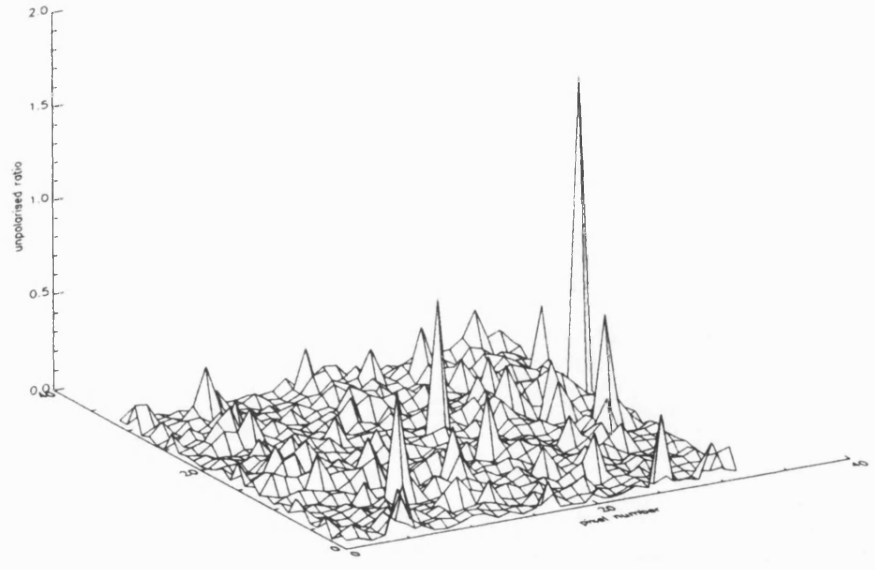

Fig.5.21 Unpolarised radiation coefficient, image 2, ocean region, L-band, 49 degrees incidence angle

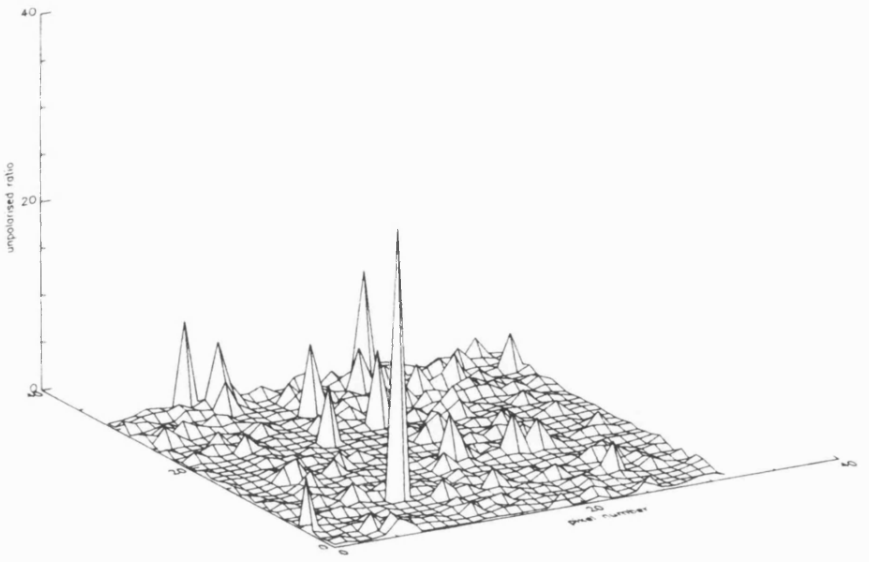

Fig.5.22 Unpolarised radiation coefficient, image 3, urban region, L-band, 28 degrees incidence angle

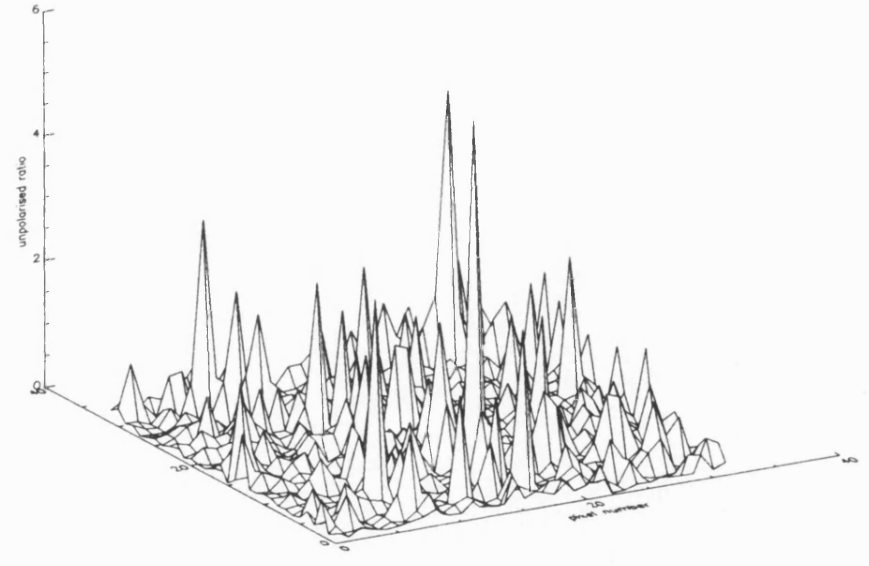

Fig.5.23 Unpolarised radiation coefficient, image 4, urban region, L-band, 49 degrees incidence angle

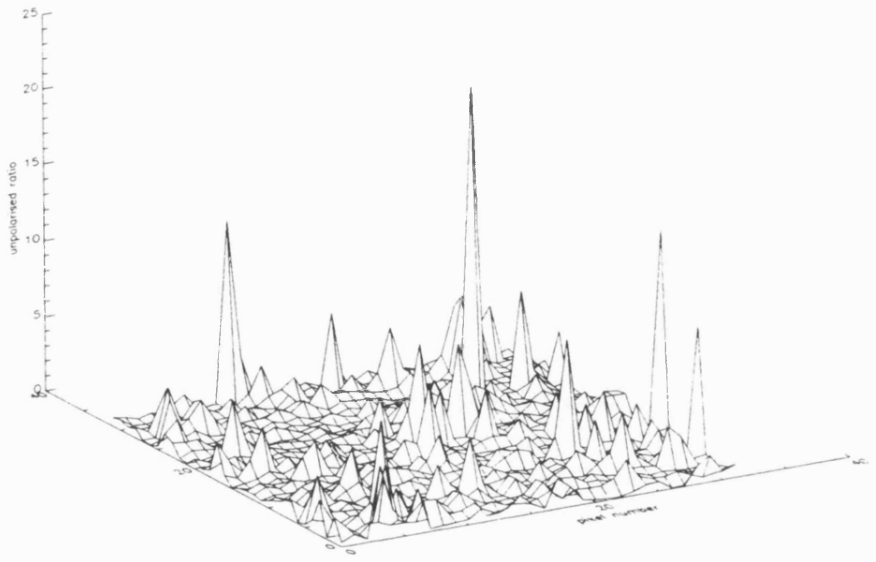

Fig.5.24 Unpolarised radiation coefficient, image 5, rain forest, P-band, 24 degrees incidence angle

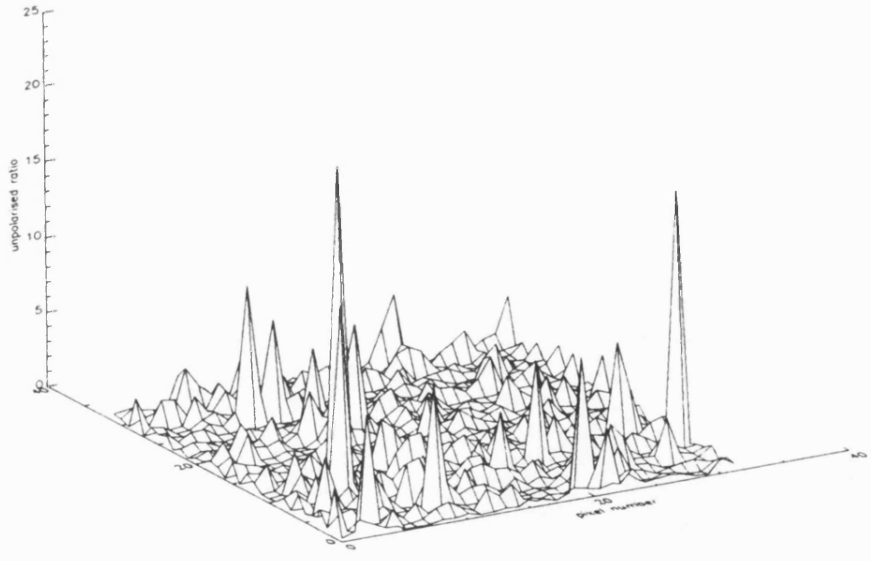

Fig.5.25 Unpolarised radiation coefficient, image 6, rain forest, P-band, 51 degrees incidence angle

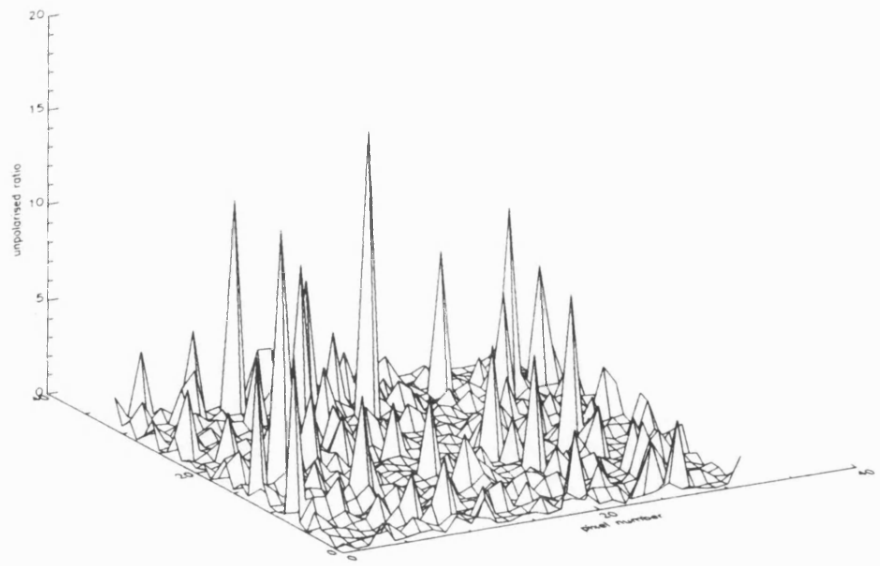

Fig.5.26 Unpolarised radiation coefficient, image 7, rain forest, L-band, 25 degrees incidence angle

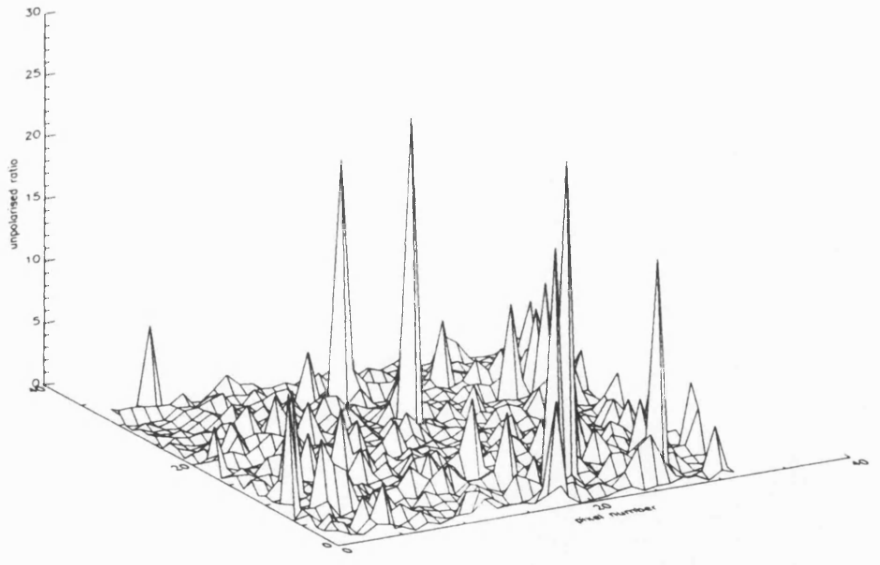

Fig.5.27 Unpolarised radiation coefficient, image 8, rain forest, L-band, 51 degrees incidence angle

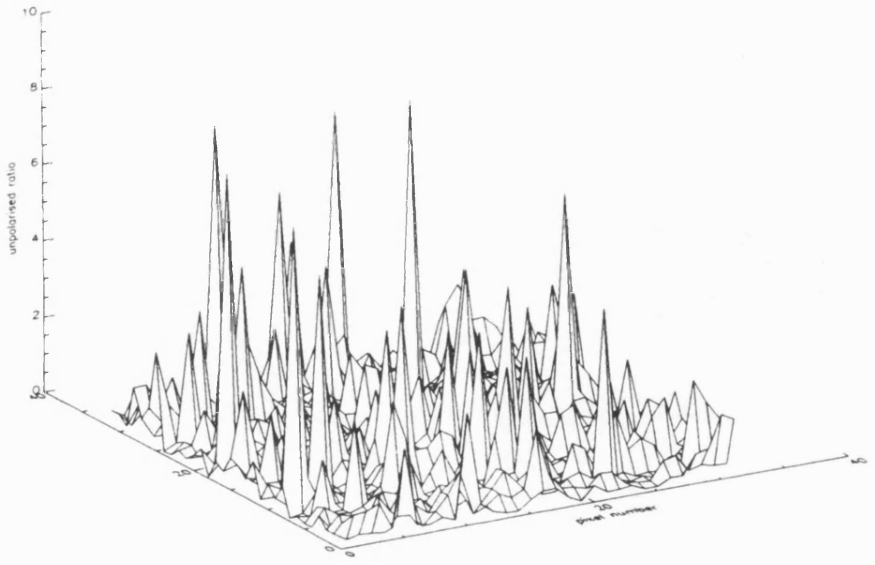

Fig.5.28 Unpolarised radiation coefficient, image 9, rain forest, C-band, 24 degrees incidence angle

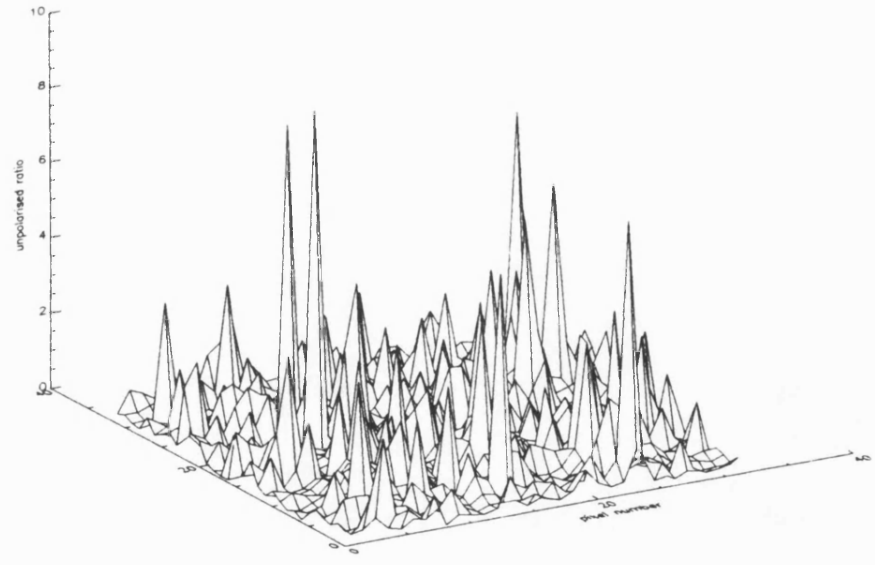

Fig.5.29 Unpolarised radiation coefficient, image 10, rain forest, C-band, 51 degrees incidence angle

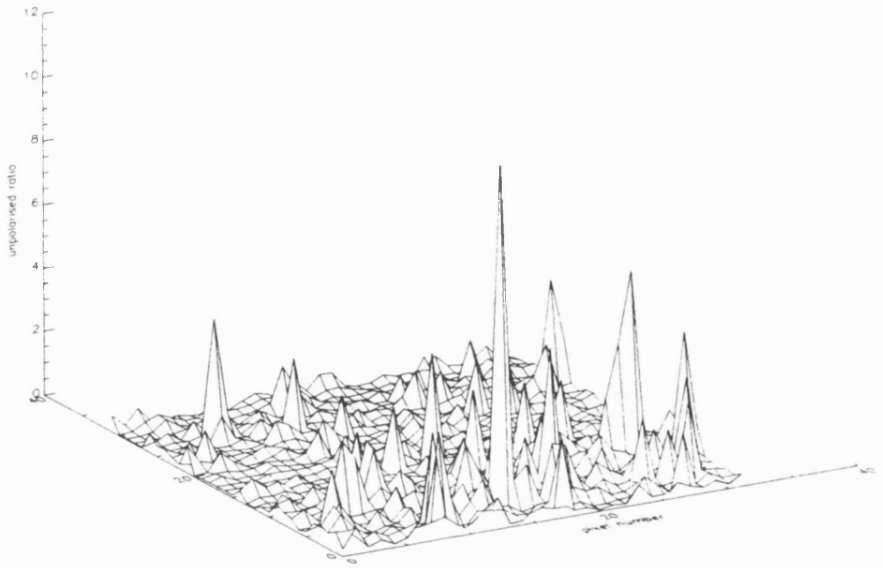

Fig.5.30 Unpolarised radiation coefficient, image 11, agricultural fields, P-band, 22 degrees incidence angle

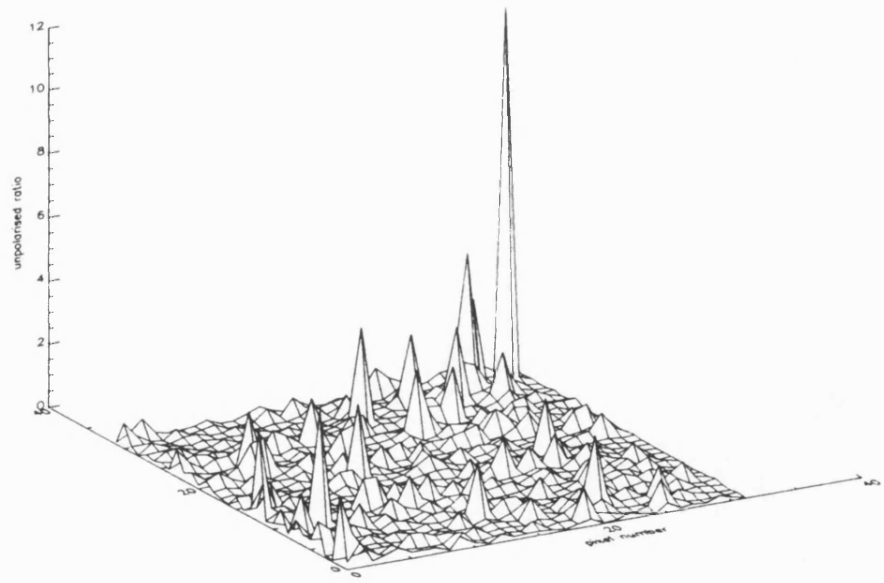

Fig.5.31 Unpolarised radiation coefficient, image 12, agricultural fields, P-band, 51 degrees incidence angle

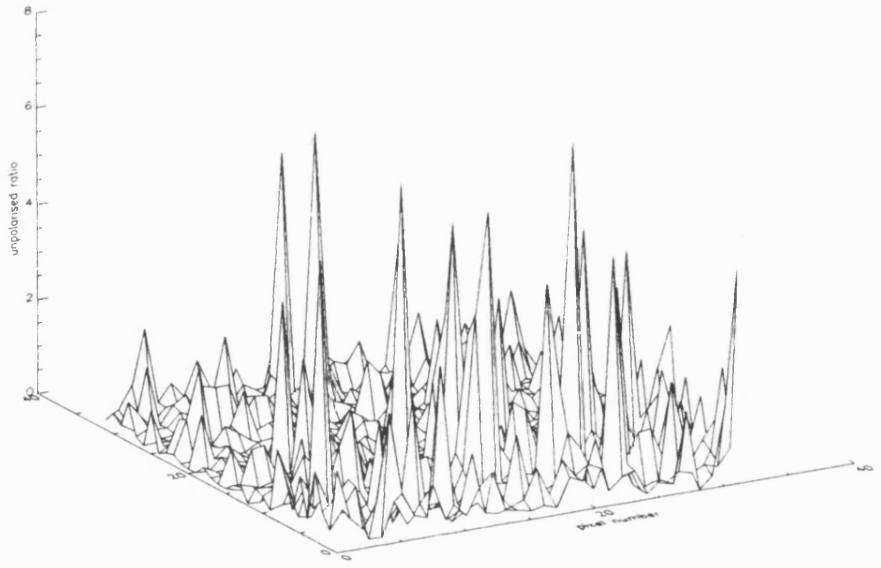

Fig.5.32 Unpolarised radiation coefficient, image 13, agricultural fields, L-band, 21 degrees incidence angle

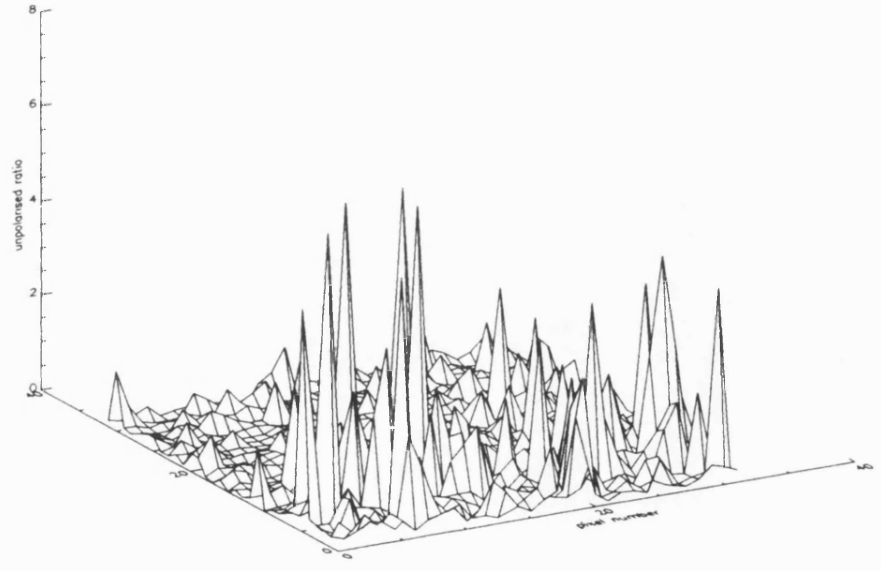

Fig.5.33 Unpolarised radiation coefficient, image 14, agricultural fields, L-band, 52 degrees incidence angle

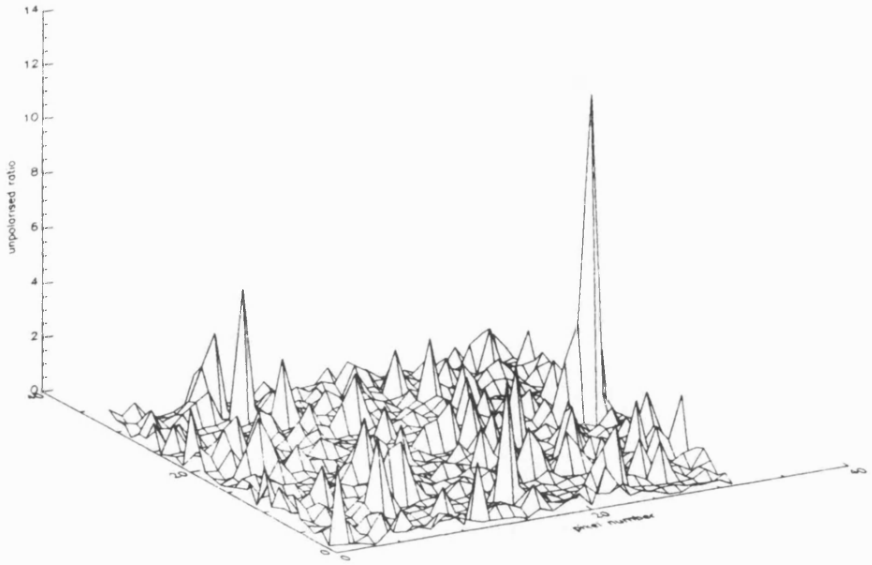

Fig.5.34 Unpolarised radiation coefficient, image 15, agricultural fields, C-band, 22 degrees incidence angle

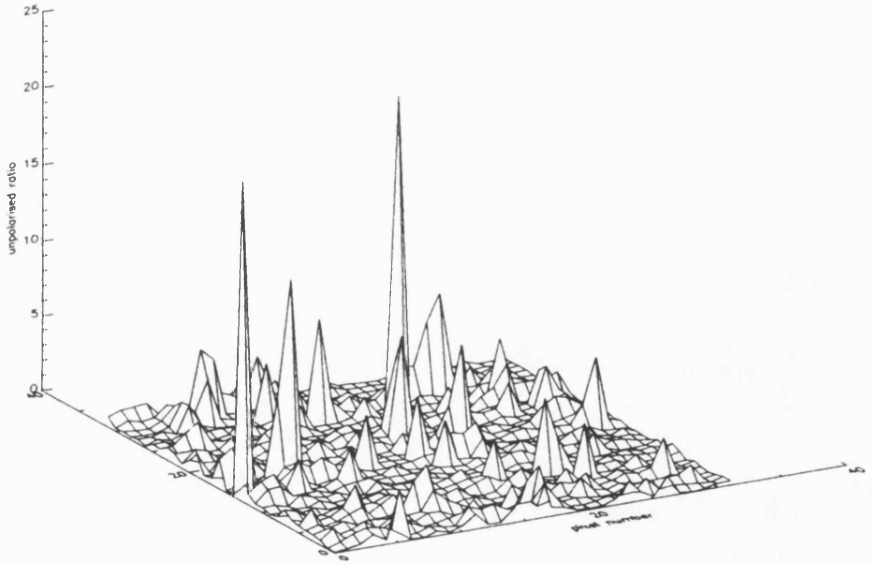

Fig.5.35 Unpolarised radiation coefficient, image 16, agricultural fields, C-band, 52 degrees incidence angle

	unpolarised radiation coefficient
Image 1 (ocean, L-band, 27 deg.)	35.01
Image 2 (ocean, L-band, 49 deg.)	64.71
Image 3 (urban, L-band, 28 deg.)	639.96
Image 4 (urban, L-band, 49 deg.)	318.31
Image 5 (rain forest, P-band, 24 deg.)	733.63
Image 6 (rain forest, P-band, 51 deg.)	839.41
Image 7 (rain forest, L-band, 25 deg.)	796.53
Image 8 (rain forest, L-band, 51 deg.)	1083.46
Image 9 (rain forest, C-band, 24 deg.)	645.24
Image 10 (rain forest, C-band, 51 deg.)	645.39
Image 11 (agriculture, P-band, 22 deg.)	354.61
Image 12 (agriculture, P-band, 51 deg.)	256.02
Image 13 (agriculture, L-band, 21 deg.)	526.51
Image 14 (agriculture, L-band, 52 deg.)	341.32
Image 15 (agriculture, C-band, 22 deg.)	470.17
Image 16 (agriculture, C-band, 52 deg.)	604.66

TABLE 12

5.3 *Characterisation of texture information in polarimetric span images*

The interest in analysing polarimetric span image texture is justified by the advantage of exploiting the polarisation channels to decrease the speckle noise without affecting spatial resolution, together with the wide vectorial information associated with the span image.

Textural features retrieved from images at different spatial resolution cannot be directly compared, indeed as in optical images a scene might show decreasing roughness when the spatial resolution is lowered. Therefore it is necessary for texture analysis to utilise high spatial resolution data.

Another factor to be considered is the effect of thermal noise on the estimation. In the previous chapter has been demonstrated the necessity to operate with large signal-to-noise ratio in order to properly estimate texture characteristics. In the following analysis, data of NASA SAR airborne campaigns will be studied. Since the sensor were functioning with a noise equivalent sigma zero exceptionally low (i.e. around -40 dB), it is believed that for most natural targets the thermal noise contribution can be neglected.
The texture variance can be expressed in the following way:

$$\text{var}(T) = \frac{\left(\frac{\text{var}(P)}{\langle P \rangle^2}\right) - \sigma_s^2}{1 + \sigma_s^2} \qquad 5.2$$

In the case of span images, the speckle contribution should not only include the effective number of looks but also the polarisation looks. In the assumption of azimuthally symmetric surfaces, we can use the following empirical expression to estimate the effects of the three polarisation channels on the speckle variance of the span image :

$$\sigma_s^2 = \frac{1}{[\,2 + (\,1 - \gamma_{HH\,VV}\,)\,]\,N} \qquad 5.3$$

where $\gamma_{HH\,VV}$ is the correlation coefficient between the two copolarised channels and N the number of effective looks. If the target does not present a negligible correlation between copolarised and crosspolarised channels (for instance urban areas with square-on street orientation relative to the radar illumination direction, where a strong dihedral type of scattering mechanism appears to be

dominant), then the formula below can be used to include the extra correlation in the polarisation looks [93,94]:

$$\sigma_s^2 = \frac{1}{[\,2+(\,1-\gamma_{HH\,VV}\,)+(\,1-\gamma_{VV\,HV}\,\gamma_{HH\,HV}\,)\,]\,N} \qquad 5.4$$

In order to compare our theoretical results with experimental data, we have analysed multipolarisation and multifrequency calibrated datasets of the NASA airborne SAR campaigns. The Shasta-Trinity (forest) and Goldstone (bare land) images are four look data from an area of 100 x 100 pixels. The Californian costal images (ocean) are also four look format but from an area of 20 x 20 pixels. The North sea images have the same characteristics as the first two datasets. Where the previous images are obtained from the NASA DC-8 multifrequency SAR, the urban areas are from the NASA CV990 and therefore single frequency (L-band), four look format from approximately an area of 100 x 100 pixels and for two different street orientations with respect to the radar illumination. The effective number of looks is 2.6 for all the available data due to similar processing characteristics of the two sensors. For each dataset, the normalised intensity variance of the span image pixel is computed using the eigenvalues of the Covariance matrix averaged over the available region. It has been shown that in order to estimate the normalised pixel intensity with an error less than 10 per cent, it is necessary to use window size larger than 20 x 20 pixels [79]. This requirement implies that for each chosen area the texture features are spatially homogenous. The experimental results are summarised in Tables 13 - 17.

From Table 13, the Shasta-Trinity vegetation area shows an increase in texture variance of the polarimetric span image versus frequency. The reason is that even if speckle is better suppressed at longer wavelength due to the higher decorrelation in the polarisation looks because of multiscattering mechanism, the upper part of the canopy

at C-band has a less random structure than in the lower frequency case (i.e. there is a predominant eigenvalue), therefore with an increased normalised intensity variance of the span image pixel (from a polarimetric point of view a fully polarised return will generate a unitary normalised intensity variance). In the Goldstone area, Table 14, the increased surface roughness at C-band generates more efficient polarisation looks and at the same time a smaller normalised variance of the span image pixel intensity. The latter effect is dominant and consequently the texture variance decreases for larger frequencies.

The two ocean images from Tables 15 and 16, show a comparable amount of texture. From the analysis of the normalised intensity variance, is evident a strong deterministic behaviour except for the C-band near and far range of the North Sea images. Indeed due to a very poor signal-to-noise ratio, the polarisation looks are extremely efficient (for the far range case the speckle variance is reduced to its theoretical limit as the three polarisation looks were completely uncorrelated) and the scene appears to have a significant random behaviour. The decrease of signal-to-noise ratio for larger incidence angle can be appreciated also in the other data sets (improved speckle suppression and increased random nature of the scene) with the exception of the Shasta-Trinity. In the latter case due to volume scattering, mainly affecting the P and L-bands, the reflectivity of the scene shows a limited dependence versus incidence angle [91].

For the urban areas, Table 17, the square-on streets image shows a stronger deterministic type of scattering with respect to the oblique geometry. The dihedral type of scattering is the dominant contribution for the square-on case generating a strong correlation between copolarised and crosspolarised channels as it is reflected in the large normalised speckle variance.

	Shasta-Trinity (forest)					
incidence angle [degree]	43.1			53.6		
frequency	P	L	C	P	L	C
normalised intensity variance	0.417	0.436	0.489	0.416	0.429	0.490
normalised texture variance	0.247	0.257	0.295	0.246	0.256	0.296
normalised speckle variance	0.136	0.142	0.150	0.136	0.138	0.150

TABLE 13

	Goldstone (bare land)					
incidence angle [degree]	47.4			56.3		
frequency	P	L	C	P	L	C
normalised intensity variance	0.779	0.752	0.620	0.739	0.714	0.554
normalised texture variance	0.513	0.496	0.393	0.484	0.471	0.343
normalised speckle variance	0.176	0.171	0.163	0.172	0.165	0.157

TABLE 14

	Californian coast (ocean)					
incidence angle [degree]	38			51		
frequency	P	L	C	P	L	C
normalised intensity variance	0.908	0.928	0.927	0.872	0.874	0.796
normalised texture variance	0.611	0.626	0.627	0.597	0.588	0.540
normalised speckle variance	0.184	0.186	0.184	0.172	0.180	0.166

TABLE 15

	North Sea					
incidence angle [degree]	38.1			48.75		
frequency	P	L	C	P	L	C
normalised intensity variance	0.935	0.937	0.579	0.786	0.893	0.433
normalised texture variance	0.630	0.632	0.392	0.533	0.604	0.270
normalised speckle variance	0.187	0.187	0.134	0.165	0.180	0.128

TABLE 16

Urban area		
incidence angle [degree]	38	
frequency	L	
geometry	square-on	oblique
normalised intensity variance	0.523	0.503
normalised texture variance	0.322	0.325
normalised speckle variance	0.152	0.134

TABLE 17

From the previous table is evident the direct impact of the normalised intensity variance on the texture variance. This is a similar effect to a single polarisation channel SAR [81]. However in multipolarisation SAR the large normalised intensity variance corresponds to highly deterministic target (i.e. ocean), where the same target in single channel SAR will appear of very limited texture content [81]. This is due to intrinsic average nature of the span image being more effective when the polarisation channels have similar intensities.

It is interesting to include the Gamma model in the analysis of the texture variance of the span image: in particular for the Shasta-Trinity and Goldstone datasets the Gamma parameter suggested in reference [68] will be applied. However the analysis results will only be seen on a qualitative basis since the data displayed in Table 6 were retrieved from measurements at much higher frequency and resolution (i.e. 33 GHz and 0.3 metres). From Tables 18 and 19, is evident the increased texture variance due to the application of the Gamma model. The texture variance seems to resemble much closer the scene roughness. Indeed in this case, a term of the intensity variance (i.e. 1/v) is independent from the polarimetric channels

	Shasta-Trinity (forest), v=2.6					
incidence angle [degree]	43.1			53.6		
frequency	P	L	C	P	L	C
normalised intensity variance	0.955	0.982	1.055	0.954	0.972	1.056
normalised texture variance	0.721	0.735	0.787	0.720	0.733	0.788
normalised speckle variance	0.136	0.142	0.150	0.136	0.138	0.150

TABLE 18

	Goldstone (bare land), v=19.3					
incidence angle [degree]	47.4			56.3		
frequency	P	L	C	P	L	C
normalised intensity variance	0.871	0.843	0.704	0.829	0.803	0.635
normalised texture variance	0.591	0.574	0.465	0.560	0.548	0.413
normalised speckle variance	0.176	0.171	0.163	0.172	0.165	0.157

TABLE 19

It is necessary to mention that the previous analysis, due to the data format provided by JPL, has been carried out using four-look data. Strictly speaking the relation between the normalised intensity variance of the span image pixel and the eigenvalues of the Covariance matrix according to (4.58), has been demonstrated under the assumption of the feature vector being three dimensional, zero mean complex Gaussian vector (i.e. single look). It is also believed, in particular for agricultural area, that for a texture analysis a much higher spatial resolution of the order of 1-2 metres will be necessary [95].

5.4 *Critical design aspects of a multipolarisation SAR*

To be able to perform polarisation imaging, the SAR will alternatively transmit two orthogonal linear polarisations and will receive for each transmitted pulse the corresponding copolar and crosspolar echoes as shown in the next figure:

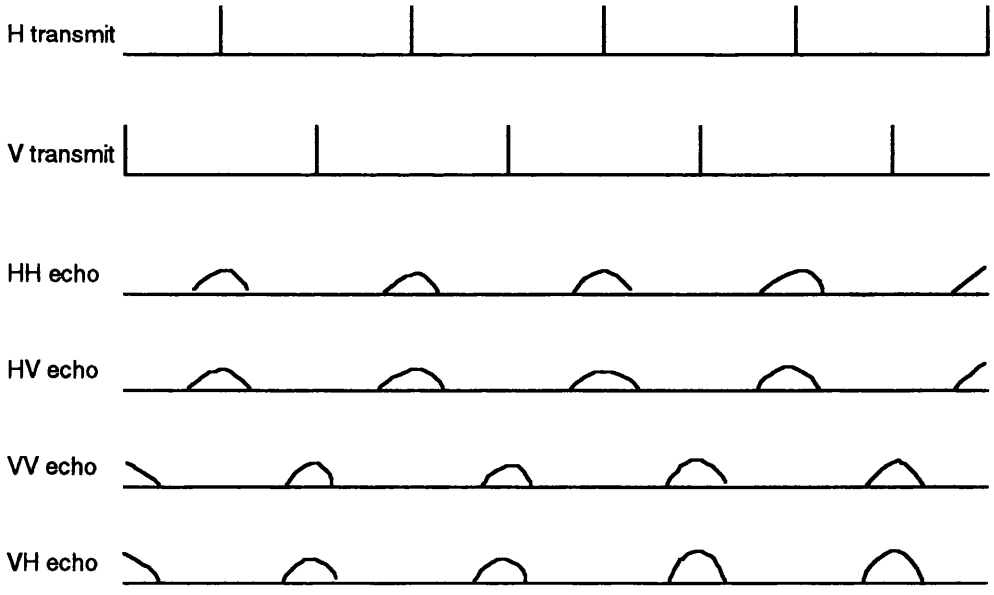

Fig.5.36 Transmit and receive multipolarisation SAR configuration

Essentially these are two synthesised antennas shifted in the azimuth direction by half of the interpulse period. The consequence of this spatial shift is a partial decorrelation between the retrieved Scattering matrix elements corresponding to the two orthogonal transmitted polarisations. In spaceborne SARs due to the stringent ambiguity suppression constraints, azimuth oversampling cannot be implemented and it is necessary to resample one channel with respect to the other to correct this effect.

The main problem in the retrivial of the crosspolar backscattered information is to achieve the necessary polarisation isolation in order to guarantee the required accuracy in the determination of the crosspolarised sigma zero. Expressing the received power in the following way [96,97]:

$$[P_r] = \frac{P_t G^2 \lambda^2}{(4\pi)^3 R^4} \int_{\Omega} [F]\,[\sigma^0]\,[F]^T \, d\Omega \qquad 5.5$$

where F is the normalised vectorial power patterns defined below:

$$[F] = \begin{bmatrix} F_{HH} & F_{HV} \\ F_{VH} & F_{VV} \end{bmatrix} \qquad 5.6$$

It is important to realise that forcing the radar to be reciprocal implies that the polarisation cross talks are mainly due to contributions from the antenna. The sigma zero matrix, being directly related to the scattering medium, is defined in a symmetrical form:

$$[\sigma^0] = \begin{bmatrix} \sigma^0_{HH} & \sigma^0_{HV} \\ \sigma^0_{HV} & \sigma^0_{VV} \end{bmatrix} \qquad 5.7$$

The basic simplifying assumption in this model is that the imaged surface, assumed statistically homogeneous, has reflectivity equal to σ^0 A, where A is the area illuminated. Such an equivalence is in

general not correct since the reflectivity (i.e. sigma) is a deterministic quantity and sigma zero is a statistical averaged quantity.

For the sake of simplicity the slant range R is assumed constant over the angular region Ω. The received power for horizontally polarised transmitted pulse is for the copolar and crosspolar channels respectively:

$$P_{r\,HH}=\frac{P_t\,G^2\,\lambda^2}{(4\pi)^3\,R^4}\int_{\Omega} F_{HH}\sigma^0_{HH}F_{HH}+F_{HH}\sigma^0_{HV}F_{HV}+F_{HV}\sigma^0_{HV}F_{HH}+F_{HV}\sigma^0_{VV}F_{HV}\,d\Omega \qquad 5.8$$

$$P_{r\,HV}=\frac{P_t\,G^2\,\lambda^2}{(4\pi)^3\,R^4}\int_{\Omega} F_{VV}\sigma^0_{HV}F_{HH}+F_{VV}\sigma^0_{VV}F_{HV}+F_{VH}\sigma^0_{HH}F_{HH}+F_{VH}\sigma^0_{HV}F_{HV}\,d\Omega \qquad 5.9$$

In both expressions the first term is essentially the desired contribution that we want to estimate from the received power, while the other terms are errors due to non-ideal polarisation isolation. From the first expression, we observe that all the error terms have two crosspolarised factors while the first term is only composed by copolarised factors, therefore the estimation of σ^0_{HH} will not be strongly affected. In the latter expression, the second and third errors terms have only one crosspolarised factor as the required first term, therefore their contribution will be of the same order of magnitude and consequently the relative error on the estimation of σ^0_{HV} will be considerable.

Since the depolarisation measurement involves extended target of area A, we need to consider the polarisation isolation requirements to be met over the area of interest. This is a critical point since often the antenna polarisation isolation rapidly deteriorates for angle away from antenna boresight. A useful rule of thumb for depolarisation

measurement, is that to obtain an accuracy of 0.5 dB in the estimation of a crosspolarised sigma zero lying x dB beneath the copolarised one, a one-way antenna polarisation isolation of x+16 dB is required [96]. In case this requirement is not satisfied and in the presence of moderate cross talk leakage, calibration techniques based on clutter statistics and applicable on processed data can be utilised [58].

Another important effect to be considered in multipolarisation SAR is the isolation of azimuth and range ambiguities. Due to the poor antenna polarisation isolation for angle away from antenna main beam, ambiguities are potential threats for the estimation of crosspolarised signal. In particular depolarised echoes can be strongly contaminated by large copolarised power feeding through the sidelobes of the aliased azimuth bandwidth. Due to the different Doppler centroid frequencies, azimuth ambiguities will also appear space shifted with respect to the their original positions and attenuated due to the mismatch with the azimuth reference function. Unless the mismatch is very large (i.e. azimuth antenna sidelobes and crosspolarised isolation over the ambiguous azimuth regions are well controlled), the correct retrievial of the weak crosspolarised return will not be accomplished.

For spaceborne SARs operating with moderate swath width at low incidence angle such as SEASAT and ERS-1, azimuth ambiguities are of major concern since they usually correspond to larger values of ground reflectivity and antenna sidelobes with respect to range ambiguities [26,98,99]. However for applications where large swath width are required, range ambiguity suppression becomes very critical mainly due to the increasing number of near range ambiguities (i.e. ambiguities lying between the imaged swath and nadir). To further complicate the matter, the need to operate in multipolarisation mode requires a careful control of antenna sidelobes and polarisation isolation in order to prevent leakage in the

crosspolarised channel of powerful copolar near range ambiguities [100].

To investigate this problem a practical example is shown using the selected subswaths of the advanced SAR, ASAR, of the ENVISAT project [100]. The ASAR itself will not provide a fully polarimetric mode, however due to its operation at high incidence angle, it provides a realistic example. The chosen radar geometry is described in the table below for three subswaths of the Scansar wide swath mode:

orbit height [km]:	824	PRF [Hz]:	2001
subswath:	W2	W4	W6
mean incidence angle [degree]:	25.2	32.8	38.0
swath width [km]:	84	67	59

TABLE 20

The three subswaths W2, W4 and W6 have one, two and three near range ambiguities respectively. The chosen PRF is related to a dual channel polarisation mode (i.e. ASAR), and strictly speaking to mantain the same azimuth ambiguity performances in a fully polarimetric mode the PRF shall be doubled [100].

To estimate the ambiguity ratio, it has been necessary to extend the ERS-1 ambiguity ratio definition. Indeed in the original ERS-1 approach, the strongest point ambiguity is considered as a measure of the overall system immunity to ambiguous returns. Due to the presence of more than one critical ambiguity, the overall near range and far range contributions (including reverse subswaths with respect to nadir) weighted by the sigma zero curve are considered.(i.e. DRAR)

The measured Scattering matrix is contaminated by ambiguous returns corresponding to transmitted polarisations parallel and orthogonal to the one reflected from the subswath of interest. The former are denoted as even and the latter as odd ambiguities. After balancing the off-diagonal terms, and under the assumption of equal cross talks leakage, δ, in the antenna sidelobes between the two polarisation channels (the mainlobe cross talk is corrected during calibration [58]), the retrieved Scattering matrix takes the following form:

$$[S] = \begin{bmatrix} S_{HH} & S_{HV} \\ S_{HV} & S_{VV} \end{bmatrix} + \sum_{j=even} A_j \begin{bmatrix} S_{HH} + 2\delta S_{HV} & S_{HV} + \delta (S_{HH}+S_{VV}) \\ S_{HV}+\delta (S_{HH}+S_{VV}) & S_{VV} + 2\delta S_{HV} \end{bmatrix}_j +$$

$$\sum_{j=odd} A_j \begin{bmatrix} S_{HV}+\delta (S_{HH}+S_{VV}) & \frac{S_{HH}+S_{VV}}{2} + 2\delta S_{HV} \\ \frac{S_{HH}+S_{VV}}{2} + 2\delta S_{HV} & S_{HV}+\delta (S_{HH}+S_{VV}) \end{bmatrix}_j \qquad 5.10$$

where A_j represents the isolation term depending on the ambiguity locations and the related instrument parameters. The selected sigma zero model for ocean scattering derived from the ERS-1 wind scatterometer and the JPL SAR airborne campaign is displayed in the figure below:

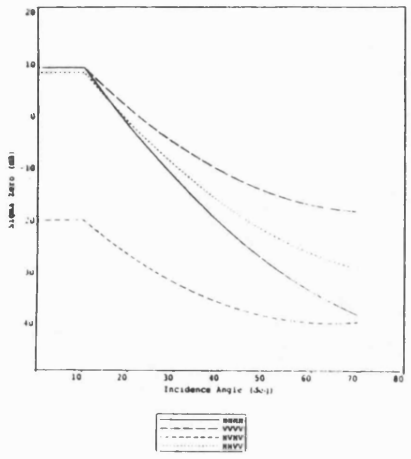

Fig.5.37 Ocean polarimetric backscatter model (after R.Cordey and P.Mancini, 1992)

A second type of polarimetric backscatter model is selected to represent forest regions. In this case the dependence versus incidence angle is negligible and copolarised power is 5.2 dB larger than crosspolarised power. The antenna pattern is chosen constant across the imaged swath with a sidelobe level set to -20 dB. Different cross talk levels are also tested in order to verify the instrument sensitivity. The simulation results are shown in the following figures, the total ambiguity levels together with the first three near (N1, N2, N3) and far range (F1, F2, F3) ambiguities are displayed versus ground range.

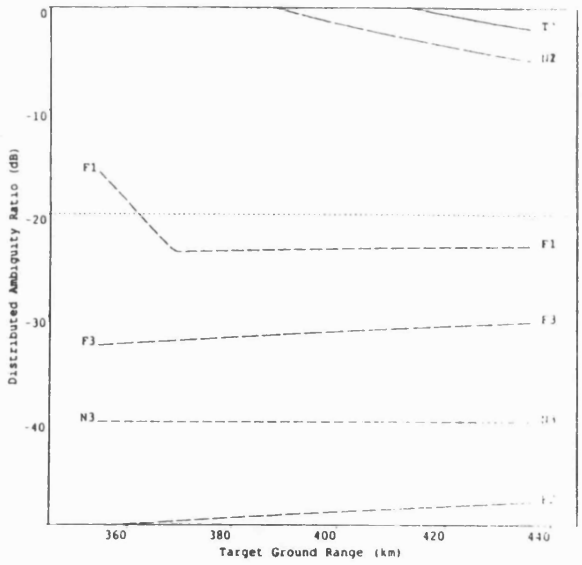

Fig.5.38 DRAR for crosspolarised power, subswath W2 (ocean), cross talk = 0, (after R.Cordey and P.Mancini, 1992)

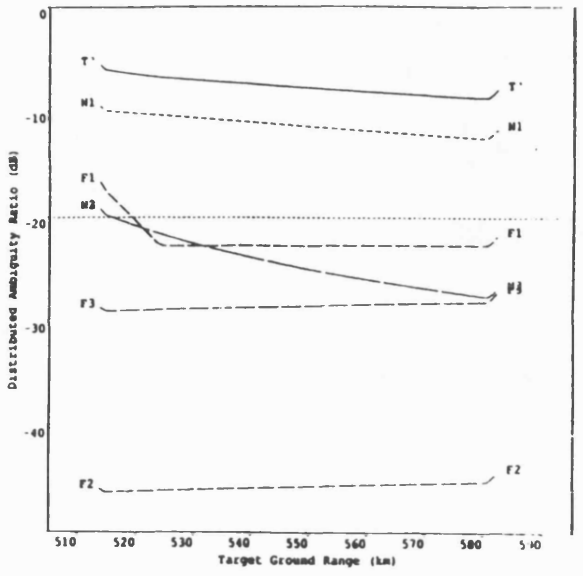

Fig.5.39 DRAR for crosspolarised power, subswath W4 (ocean), cross talk = 0, (after R.Cordey and P.Mancini, 1992)

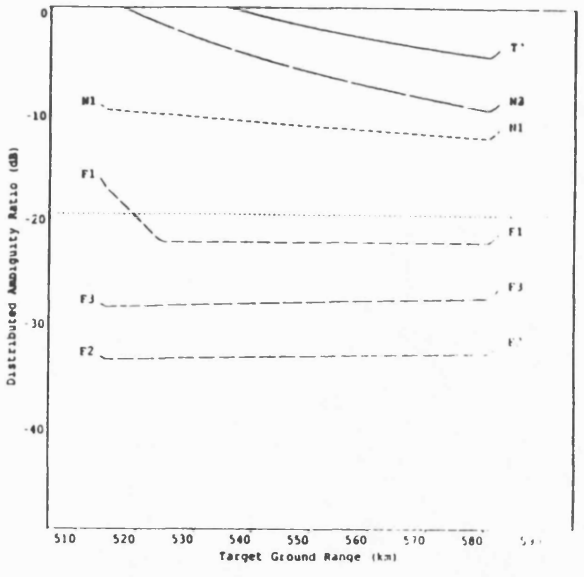

Fig.5.40 DRAR for crosspolarised power, subswath W4 (ocean), cross talk = 0.2, (after R.Cordey and P.Mancini, 1992)

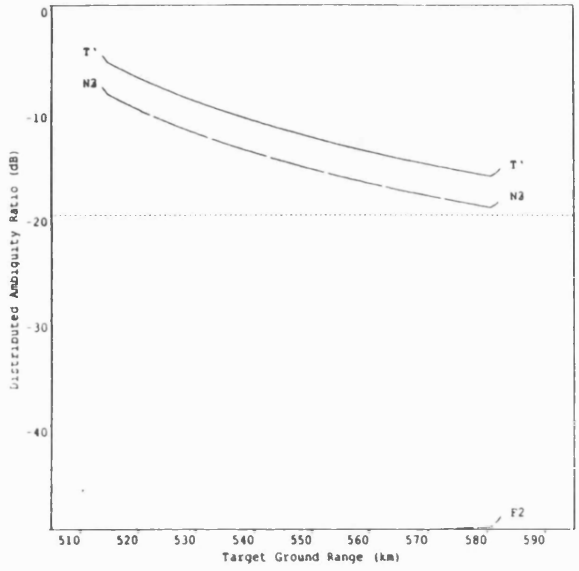

Fig.5.41 DRAR for horizontally polarised copolar power, subswath W4 (ocean), cross talk = 0, (after R.Cordey and P.Mancini, 1992)

For the subswath W2 (ocean), the distributed range ambiguity ratio (DRAR) for the crosspolar power is well above zero dB in most of the swath extent. This is mainly due to the first two near range ambiguities, the second located at the other side of the nadir, strongly affecting the total contribution. The large copolar to crosspolar ratio in the ocean model at low incidence angle is the main reason of the large N1 and N2 leakages (indeed they both corresponds to odd ambiguities) (fig.5.38). The presence of cross talk will further deteriorate the DRAR mainly due to the even ambiguities.

For the subswath W4 (ocean), the DRAR for the crosspolar power is above -10 dB, the main reason being the first odd near range ambiguities due to the model behaviour at low incidence angle (fig. 5.39). As the cross talk is introduced, the effect of even ambiguities become dominant allowing a large leakage from the copolar channels (fig.5.40). It is also interesting to verify that the horizontal copolar power is strongly contaminated from the even ambiguities as in single polarisation SAR (fig.5.41). This is due to the steepest behaviour of the reflectivity for horizontal polarisation.

For the subswath W6 (ocean), the situation is very similar with the only difference of the presence of an extra near range odd ambiguity N3, strongly affecting the crosspolar power even before the effect of cross talk is introduced. For all three subswaths, in the case of forest imaging, the DRAR remains below -20 dB, mainly due to the flatness of the selected sigma zero model.

The previous example outlines the difficulties of SARs to operate in a multipolarisation mode when the imaged surface has a large copolar to crosspolar power ratio, a strong dependence of reflectivity versus incidence angle and the instrument itself has poor antenna sidelobe levels and polarisation isolation.

5.5 *On-board polarimetric processing for SAR*

The coherent backscattered radiation can be described using the Scattering matrix via the relation:

$$\begin{bmatrix} E_{1s} \\ E_{2s} \end{bmatrix} = K \begin{bmatrix} S_{11} & S_{21} \\ S_{21} & S_{22} \end{bmatrix} \begin{bmatrix} E_{1t} \\ E_{2t} \end{bmatrix} \qquad 5.11$$

where E_1 and E_2 denote the orthogonal linearly polarised components of the electromagnetic field, and the subscripts t and s stand for the transmitted and scattered radiation respectively. The

constant K depends on the propagation distance and the carrier frequency. Clearly, a knowledge of the Scattering matrix allows us to predict the backscattered radiation. In the monostatic case the Scattering matrix is assumed to be reciprocal (this is true in practice for any natural target), and neglecting an absolute phase term, five independent quantities (three amplitudes and two phases) are necessary to completely specify the Scattering matrix. We will use the assumption that the copolarised and crosspolarised components of the Scattering matrix are uncorrelated for an azimuthally symmetric surface. Physically this means that the cross-polarised component comes from higher order scattering: the two contributions in a random medium are essentially uncorrelated. In practice this assumption does not always hold, because of the different scattering mechanisms involved and the preferred symmetry direction of the scatterers.

Very often in SAR applications the Stokes scattering operator is used to describe the polarisation behaviour of a target, indeed since it is capable of describing incoherent scattering it can always be applied to N-look SAR images. The Stokes scattering operator will correspond to an equivalent Scattering matrix only if there exists a dominant scattering mechanism with uniform properties over the scene.

Therefore, since the Scattering matrix is a coherent descriptor of the polarisation state, it is not capable of analysing partially polarised radiation typically generated from random media. However, if we are observing the backscattered radiation for very short time and space intervals such that the reflected electromagnetic field from any target can be considered fully polarised, the Scattering matrix approach is still well justified.

For several distributed targets, the polarisation characteristics are quite uniform over different resolution cells. Typically for an ocean

region where for large incidence angles Bragg scattering is the dominant mechanism, or an urban area with the streets normal to the radar direction where two-bounce dihedral type scattering is the main contribution to the backscattered radiation, it is possible to extract information on the polarisation properties of the scene directly using the raw SAR data.

In order to measure the Scattering matrix, the multi-polarisation SAR transmits alternate orthogonal polarisations. This technique has the drawback that there is a time delay between the measurement of the two complex couples $\{S_{11}, S_{21}\}$ and $\{S_{21}, S_{22}\}$. Indeed, if each resolution cell consists of several scattering centres, the coherent interference of these random scattering elements will essentially create the speckle phenomenon. Since the speckle correlation length is of the order of half the antenna length in the azimuth dimension, and the distance travelled between two transmitted pulse in a spaceborne polarimetric SAR is of the order of half this quantity, measurable decorrelation will occur between scattering elements of the same resolution cells. Clearly, if we want to estimate the low resolution Scattering matrix this decorrelation effect should be avoided.

An alternative technique based on the simultaneous transmission of orthogonal waveforms has been proposed by Giuli [101,102]. The simultaneous transmission of orthogonal waveforms satisfying the following properties:

$$\int_{-\infty}^{\infty} e_i(t)\, e_i^*(t+\tau)\, dt = \begin{cases} 1 & \tau = 0 \\ 0 & \tau \neq 0 \end{cases} \quad i = 1, 2 \qquad 5.12$$

$$\int_{-\infty}^{\infty} e_i(t)\, e_j^*(t+\tau)\, dt = 0 \quad \text{for any } \tau \qquad 5.13$$

together with a receiver of the form shown in figure 5.42, will permit real-time estimation of the low resolution Scattering matrix elements.

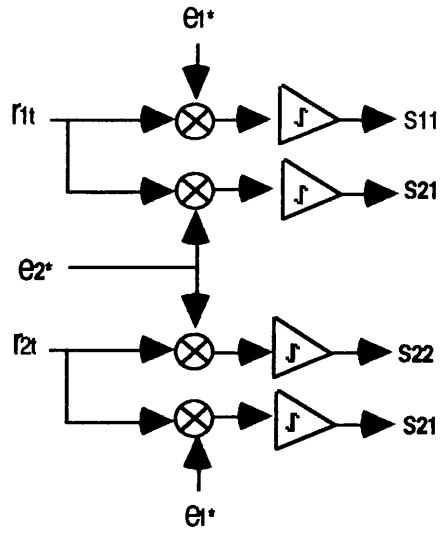

Fig.5.42 Receiver block diagram (after D.Giuli, L.Facheris, M.Fossi and A.Rossettini, 1990)

Let us investigate the condition for fully polarised backscattered radiation using the Coherence matrix conditions 4.19 and 4.20. For the orthogonal waveform transmission, the Coherence Matrix elements for the orthogonal waveform transmission become:

$$J_{11} = |S_{11}|^2 + |S_{21}|^2 \qquad 5.14$$

$$J_{22} = |S_{22}|^2 + |S_{21}|^2 \qquad 5.15$$

$$J_{12} = S_{11}\, S_{21}^* + S_{21}\, S_{22}^* \qquad 5.16$$

$$J_{21} = S_{21}\, S_{11}^* + S_{22}\, S_{21}^* \qquad 5.17$$

In order to have an accurate estimate of the mean of the Coherence Matrix elements, under the assumption of ergodicity, it is necessary to time average the 'instantaneous' samples for a time longer than

the speckle correlation length. This operation will destroy the phase information carried by J_{12} and J_{21} Using the previous scattering assumptions the Coherence Matrix elements become:

$$J_{11} = \langle |S_{11}|^2 \rangle + \langle |S_{21}|^2 \rangle \qquad 5.18$$

$$J_{22} = \langle |S_{22}|^2 \rangle + \langle |S_{21}|^2 \rangle \qquad 5.19$$

$$J_{21} = J_{12} = 0 \qquad 5.20$$

and the condition for a fully polarised backscattered wave becomes:

$$\langle |S_{22}|^2 \rangle \langle |S_{11}|^2 \rangle + \langle |S_{21}|^2 \rangle \left(\langle |S_{11}|^2 \rangle + \langle |S_{22}|^2 \rangle + \langle |S_{21}|^2 \rangle \right) = 0 \qquad 5.21$$

Neglecting the trivial solution for which the average power of each polarisation channel is zero, the other solutions are:

$$\langle |S_{21}|^2 \rangle = 0 \quad \text{and} \quad \langle |S_{11}|^2 \rangle = 0 \qquad 5.22$$

$$\langle |S_{21}|^2 \rangle = 0 \quad \text{and} \quad \langle |S_{22}|^2 \rangle = 0 \qquad 5.23$$

In order to have a fully polarised radiation regardless of the transmit polarisation, the two conditions below must be satisfied [70]:

$$\langle |S_{21}|^2 \rangle = 0 \qquad 5.24$$

$$|\gamma| = \frac{|\langle S_{11} S_{22}^* \rangle|}{\left(\langle |S_{11}|^2 \rangle \langle |S_{22}|^2 \rangle \right)^{1/2}} = 1 \qquad 5.25$$

Conditions 5.24 and 5.25 include conditions 5.22 and 5.23, as can be demonstrated by applying Schwartz's inequality. This confirms the fact that 5.24 and 5.25 are true for any transmitted polarisation.

To verify these concepts we have analysed four airborne SAR images, corresponding to different types of scattering mechanisms. The data were acquired by the NASA/JPL SAR airborne campaigns. The areas considered are of 100 x 100 pixels size and the results of the analysis are shown in Table 21 [101].

frequency	forest		bare terrain		urban area		ocean	
	$\|\gamma\|$	$<\|S_{21}\|^2>$	$\|\gamma\|$	$<\|S_{21}\|^2>$	$\|\gamma\|$	$<\|S_{21}\|^2>$	$\|\gamma\|$	$<\|S_{21}\|^2>$
P	0.18	20.1	0.8	4.7	0.3^{*1}	2.47^{*1}	$0.94^{\#1}$	$0.32^{\#1}$
L	0.3	14.0	0.73	5.0				
C	0.44	11.5	0.64	8.0	0.12^{*2}	4.92^{*2}	$0.89^{\#2}$	$0.11^{\#2}$

TABLE 21

* both at L-band with *1 having streets parallel and perpendicular to the radar propagation direction, while in *2 the streets are at an oblique angle.
# both at L-band, with #1 at 32.8° and #2 at 48.8° incidence angles.

For the forest area, the unpolarised component tends to diminish with increasing frequency. This is because the penetration depth will decrease, as will the multiscattering phenomena associated with the branches, trunk and soil surface. For bare terrain the behaviour with frequency is opposite, due to the increased surface roughness and consequently a less specular type of reflection. For the case of normal geometry, the urban area has a lower unpolarised component, indeed a very large two-bounce type of scattering mechanism is dominant, and correspondingly a strong correlation between the copolar components of the backscattered radiation with respect to the oblique geometry demonstrating a larger deterministic behaviour. In the case of ocean surface we have a correlation coefficient close to unity, with very low crosspolarised power. We are not able to demonstrate a tendency versus incidence angle due to a dominant Bragg scattering contribution in both cases.

Since the Scattering matrix elements shown previously were generated from a region of 100 x 100 pixels, we expect that the low resolution Scattering matrix estimates can carry useful information about the vectorial scattering behaviour of the scene. The simultaneous transmission of two orthogonal waveforms and the use of a receiver as shown in figure 5.42 will make available the low resolution Scattering matrix elements directly on-board (note that the data will only be 'low resolution' in azimuth, since range compression will have been carried out in the receiver). Knowledge of S_{21} differences in the two receiver channels, will allow the degree of non-reciprocity in the transmit and receive paths to be estimated and calibrated, giving an increase of 3 dB in signal-to-noise ratio after the two crosspolar channels merging [60].

The orthogonal waveform generation capability could also be used in the traditional multipolarisation mode (i.e. alternate orthogonal waveform transmission), to reduce the crosspolar contamination and to differentiate horizontal from vertical polarised data. In the former application, the improvement will be obtained only for the imaging of point targets such as calibration reflectors.

It appears from Table 21, that the correlation coefficient between the two co-polarised channels carries very useful information about the vectorial backscatter nature of the imaged scene, its estimation will be capable of identifying the type of natural target on a qualitative basis. For the accurate estimation of the low resolution Scattering matrix elements, it is necessary to decrease the amount of associated speckle noise. Typically the ensemble average at image level is performed as a power average over adjacent pixels. In our case, however, the lack of azimuth processing will permit averaging on a shorter time basis, of the order of the uncompressed pulse length. Since we are interested in a coherent estimate of the Scattering matrix elements, multiple samples in the complex vector domain should be added in order to reduce the effect of fading [103].

Polarimetric Synthetic Aperture Radar is capable of estimating the full vectorial scattering behaviour of each pixel. In this chapter we have shown the possibility of deriving useful polarimetric information from the eigenvalues of the Covariance matrix. A new polarisation descriptor for the characterisation of the unpolarised radiation component has been introduced (i.e. the unpolarised radiation coefficient) and validated using multipolarisation and multifrequency airborne SAR data. The Covariance matrix eigenvalues has also demonstrated to occupy an important role in the description of the texture of polarimetric span images. Critical design aspects of a multipolarisation SAR have been presented with a particular emphasis to the problem of measuring the weak depolarised return in the presence of large copolar ambiguous power. The potentials of using orthogonal waveforms techniques to exploit raw data directly on-board in order to improve the instrument performances has been demonstrated. At the price of an increased complexity of the radar transmit and receive chains, significant gain in signal-to-noise ratio for the crosspolarised channel can be achieved.

6. CONCLUSIONS

6.1 *Summary of the main ideas and conclusions of the thesis*

The main objectives of this thesis have been to show the usefulness of the polarimetric information in SARs and in particular the use of the Covariance matrix, as a second order descriptor for multipolarisation SAR images.

In order to outline the benefits of having a complete vectorial description of the imaged scene, a review of the main application areas has been presented. In particular, for land application the multipolarisation capability has shown interesting potentials in the separation and measurement of soil and vegetation moisture and in the ability in classifying forest canopy using the crosspolarised channel information.

In oceanography, polarisation information has been shown to improve the understanding of different type of scattering mechanisms. The importance of tilt modulation with respect to orbital or roughness modulation will certainly be explored with future advanced sensors due to their multifrequency, multiangle and multipolarisation capabilities. In glaciology, the unique capability of multipolarisation SARs in distinguishing between surface scattering and volume scattering has resulted in an improved ability in ice modelling and classification.

After a review of the application areas, in the second chapter the basic principles of SAR theory have been presented. The radar equation, azimuth and range ambiguities, bidimensional matched

filter theory and error analysis have been described. An alternative spatial frequency description of the Doppler imaging mechanism has been introduced in order to show the direct implication of the antenna taper on the speckle filtering. The role of the antenna pattern as a spatial speckle filter has been theoretically demonstrated and the exploitation of a reconfigurable antenna capable of generating a non-reciprocal pattern has been proposed as an alternative way to filter speckle noise.

Different SAR processing techniques such as time-domain correlation, range-doppler, spectral-analysis and two-dimensional fast correlation have been reviewed in order to demonstrate their suitability for different sensor specifications. For a swath width of modest dimensions, the spectral analysis approach based on the concept of deramp processing, has shown interesting potentials to decrease the instrument data rate.

In the third chapter, the basis of radar polarisation theory have been presented. Classical descriptors such as the Scattering matrix, the Stokes scattering operator, the Mueller matrix and the polarisation signature together with their physical interpretations have been analysed. For classical scattering models, the polarisation signature were derived and compared with experimental results obtained from airborne multipolarisation SAR campaigns. The ocean data demonstrated that multipolarisation SARs allow the validation of the classical scattering model that considers dominant specular reflection for small incidence angles and Bragg scattering for large incidence angles.

From the data of urban regions, a similarity was evident with the signatures of an ideal dihedral corner reflector. The main difference with the theoretical case was the presence of a large pedestal in both copolar and crosspolar signatures that was related to the amount of unpolarised radiation generated during the incoherent averaging

process necessary to filter signal statistical variations. In the case of vegetation area, the polarisation signatures showed the largest pedestal among the experimental data due to an increased amount of multiple scattering and consequently a very poor polarisation discrimination capability.

The impact of thermal noise in the overall polarimetric SAR performances has been assessed together with calibration techniques capable of estimating the noise power on the basis of assumption on clutter statistics.

In the fourth chapter, the Covariance matrix descriptor for multipolarisation SAR data has been introduced. Its important role in the maximisation of the power backscattered from two areas characterised by different scattering properties has been demonstrated through the use of the Rayleigh maximisation principle. The role of the eigenvalues of the Covariance matrix in the analysis of the polarimetric span image has been outlined. The potentials to obtain texture information from the knowledge of the eigenvalues both for Gaussian and Gamma clutter models have been described. The effect of a decreased spatial homogeneity of the Gamma model resulted in a larger normalised standard deviation of the span image pixel intensity with respect to the Gaussian clutter model.

The impact of thermal noise on the estimation process has also been analysed, showing the need to operate with signal-to-noise ratio larger than 10 dB if texture information is of interest.

The use of combining the polarisation channels to obtain extra polarisation looks has also been analysed. The optimal weighting matrix, even if it were always capable to obtain the best polarimetric channel averaging efficiency, required the knowledge of the amplitude and phase of the correlation coefficient. The simpler span processing at the expense of an averaging efficiency depending on

clutter statistics, only required the knowledge of correlation amplitude independently of accurate polarimetric calibration.

The main objectives of the fifth chapter have been to analyse multipolarisation airborne SAR images utilising the Covariance matrix descriptor in order to demonstrate its usefulness experimentally. The unpolarised radiation content has been characterised using the minimum eigenvalue of the Covariance matrix and the unpolarised radiation coefficient. The former descriptor was not always capable of fully representing the unpolarised radiation content, while the latter, due to its intrinsic capability of containing information related to the average crosspolarised power and the amplitude of the copolarised channel correlation demonstrated a larger agreement with the results obtained using the measurement of the pedestal height of the polarisation signatures.

The analysis of texture of polarimetric span images has been carried out utilising experimental data. The results obtained both for the Gaussian and Gamma models, have shown the importance of properly characterising the polarisation looks to retrieve span image texture information. The texture analysis was also capable of detecting poor signal-to-noise ratio at C-band during ocean imaging through the increase randomness of the scene.

The difficulties in operating a SAR in multipolarisation mode have been demonstrated through the analysis of the range ambiguities in a scansar wide swath mode. The results shown the stringent requirements imposed on antenna range sidelobes and cross talk calibration when the instrument is operating on clutter with large copolar to crosspolar power ratio. The presence of near range ambiguities due to the associated larger reflectivity and shorter range with respect to the useful imaged area, not only affected the determination of the weak crosspolar channel but also the retrieval of the horizontally polarised signal in the presence of dominant Bragg

scattering (i.e. imaging of ocean surfaces at large incidence angle). The presence of cross talk leakage further increased the distributed range ambiguity ratio.

The utilisation of orthogonal waveform techniques has been analysed as a way to correct lack of instrument reciprocity and consequently to optimise the merging of the crosspolar channels. The main advantage of this technique is a 3 dB improvement in signal-to noise ratio of the crosspolar channel together with a decrease of the instrument data rate. In case of imaging of point targets such as calibration reflectors, the use of the orthogonal wave techiques in the traditional multipolarisation mode (i.e. alternate orthogonal waveform transmission) will also reduce the crosspolar contamination.

The advantage of the simultaneous estimation of the low resolution Scattering matrix elements as a way to have on-board polarimetric information of the imaged scene has been validated against experimental multipolarisation SAR airborne data.

6.2 *Ideas for further work*

The need to enlarge the flexibility of future spaceborne SARs is demonstrated from the increased number of application areas where this sensor finds utilisations. This is also supported by the large technological development taking place in areas such as active antenna technology and digital signal processing.

The use of an active array antenna in future SARs will permit the exploitation of the echo information at subarray levels. On-board estimation of the speckle power spectrum using the subarray signal availability, will provide direct information on the scene clutter statistics and the capability to adapt the azimuth spatial resolution to variable scene coherence. The suitability of this approach will depend on the capability of improving the signal-to-noise ratio at

subarray level varying the amount of transmitted peak power. This approach should be traded off with traditional spot beam mode, where the azimuth resolution can be improved at the price of a loss of continuous coverage.

The exploitation of the polarisation information will find a large set of applications in future SARs. When applicable, the use of low resolution polarisation information directly on-board, will permit optimisation of the sensor performances to the imaged scene. For instance when flying over forest areas, the crosspolarised power will be typically few dBs lower than the copolarised power and the antenna sidelobe level could be relaxed to improve the signal-to-noise ratio. On the other hand, when operating over ocean area at very large incidence angle, the sensor will probably not be capable of measuring the crosspolarised power due to the large range ambiguity contamination and therefore or the sensor will only operate in dual polarisation mode (i.e. only the two copolar power are alternatively transmitted and detected) or the crosspolar channel shall be properly calibrated and merged. This polarisation flexibility could be obtained directly on-board exploiting the low resolution polarisation information together with the orthogonal waveform technique.

The use of the unpolarised radiation content in the optimisation of the transmitted and receive antenna polarisations is also seen as an area of potential interest for future research. Indeed, for a target with very low unpolarised radiation content, the capability to optimise the antenna polarisation characteristics to increase the target detectabilty will be extremely beneficial. The use of an on-board adaptive matching capability will allow to decrease the sensor data rate at the price of complex on-board processing. Since this approach will mainly be beneficial for quasi-deterministic targets, the need for on-board SAR processing should be assessed.

To conclude, the use of polarisation information in SARs is creating a completely new world of application to be explored. The capability of future research to match the development of improved electromagnetic models and SAR processing techniques with advances in future technology will be the key factors to optimise the utilisation of the polarisation information.

REFERENCES

[1] C.Wiley, "Pulsed Doppler Radar Methods and Apparatus", U.S. Patent 3, 196, 436, Filed August 13, 1954, patented July 20, 1965.

[2] R.L.Jordan, "The SEASAT-A Synthetic Aperture Radar System", IEEE Journal of Oceanic Engineering, Vol. OE-5, No.2, pp. 154 -164, April 1980.

[3] C.Elachi, T.Bicknell, R.L.Jordan and C.Wu, "Spaceborne Synthetic Aperture Imaging Radars: applications techniques and technology", Proc. IEEE, Vol.70, No.10, pp.1174 - 1209, October 1987.

[4] J.Way and E.A.Smith, "The Evolution of Synthetic Aperture Radar Systems and their Progression to the EOS SAR", IEEE Transactions on Geoscience and Remote Sensing, Vol.29, No.6, pp.962 - 985, November 1991.

[5] "ERS-1 A new tool for global environmental monitoring in the 1990's", ESA Publication ,BR-36, ISBN 92-9092-019 X, November 1989.

[6] R.K.Raney, A.P.Luscombe, E.J.Langham and S.Ahmed, "RADARSAT", Proc. IEEE ,Vol.79, No.6, pp.839 - 849, June 1991.

[7] C.Elachi, "Spaceborne Radar Remote Sensing: Applications and Techniques", IEEE Press, 1988, IEEE order number PC 02295, New York.

[8] T.Le Toan, "Study of the potential of Sar for crop identification and monitoring", Proc. Workshop on Thematic Applications of Sar data, pp.73 - 85, Frascati, September 1985.

[9] T.LeToan, A. Beaudoin, J.Riom and D.Guyon, "Relating forest biomass to SAR data", IEEE Transactions on Geoscience and Remote Sensing, Vol.30, No.2, pp.403 - 411, March 1992.

[10] A.K.Fung and K.S.Chen, "Dependence of the surface backscattering coefficients on roughness, frequency and polarisation states", International Journal of Remote Sensing, Vol.13, No.9, pp.1663-1680, 1992.

[11] M.G.Wooding, "Imaging Radar Applications in Europe", ESA Publication, TM-01, October 1988.

[12] E.Rodriguez and J.M.Martin, "Theory and design of interferometric synthetic aperture radars", IEE Proceedings-F, Vol.139, No.2, pp.147-159, April 1992.

[13] C.Elachi and W.E.Brown, "Models of radar imaging of the ocean surface waves", IEEE Transactions on Antennas and Propagation, Vol.AP-25, No.1, pp.84-95, January 1977.

[14] I.Robinson, "Satellite Oceanography", Ellis Horwood 1985, pp.373-394.

[15] R.A.Cordey and J.T.Macklin, "Complex SAR imagery and speckle filtering for wave imaging'", IEEE Transactions on Geoscience and Remote Sensing, Vol.27, No.6, pp.666-673, November 1989.

[16] L.M.J.Brown, J.A.Conway, J.T.Macklin, D.C.Brewster and N.R.Stapleton, "Multipolarisation SAR: fundamental concepts and applications", GEC-Marconi, final report MTR 89/16, pp.79-94, October 1989.

[17] R.Kwok, M.Drinkwater, A.Pang and E.Rignot, "Characterisation and classification of sea ice in polarimetric SAR data", IGARSS 1991, Espoo Finland, Vol.1, pp.81-84, June 1991.

[18] C.E.Cook and M.Bernfeld, "Radar Signals", Academic Press, New York, 1967.

[19] J.R.Klauder, A.C.Price, S.Darlington and W.J.Albersheim, "The Theory and Design of Chirp Radars", The Bell System Technical Journal, Vol. XXXIX, No.4, pp.745-808, July 1960.

[20] J.C.Curlander and R.N.McDonough, "Synthetic Aperture Radar Systems and Signal Processing", Wiley-Interscience Publication, 1991.

[21] R.K.Raney, "Considerations for SAR image quantification unique to Orbital Systems", IEEE Transactions on Geoscience and Remote Sensing, Vol.29, No.5, pp.754-760, September 1991.

[22] A.Freeman, J.Curlander, J.Dubois and J.Klein, "SIR-C Calibration Workshop Report", JPL Technical Report # D-6165, November 1988.

[23] L.Porcello, "Turbulence-induced phase errors in Synthetic Aperture Radars", IEEE Transactions on Aerospace and Electronic Systems, Vol.AES-6, No.5, pp.636-644, September 1970.

[24] R.K.Raney, "SAR response to partially coherent phenomena", IEEE Transactions on Antennas and Propagation, Vol.AP-28, No.6, pp.777-787, November 1980.

[25] K.Tomiyasu, "Conceptual performance of a satellite borne, wide swath Synthetic Aperture Radar", IEEE Transactions on Geoscience and Remote Sensing, Vol.GE-19, No.2, pp.103-116, April 1981.

[26] F.K.Li and W.T.K.Johnson, "Ambiguities in Spaceborne Synthetic Aperture Radar Systems", IEEE Transactions on Aerospace and Electronics Systems, Vol.AES-19, No.3, pp.389-396, May 1983.

[27] F.K.Li, D.N.Held, J.C.Curlander and C.Wu, "Doppler Parameter Estimation for Spaceborne Synthetic Aperture Radars", IEEE Transactions on Geoscience and Remote Sensing, Vol.GE-23, No.1, pp.47-55, January 1985.

[28] J.W.Goodman, "Some fundamental properties of speckle", J.Opt.Soc.Am., Vol.66, No.11, pp.1145-1149, November 1976.

[29] L.J.Porcello, N.G.Massey, R.B.Innes and J.M.Marks, "Speckle reduction in Synthetic Aperture Radar",J.Opt.Soc.Am., Vol.66, No.11, pp.1305-1311, November 1976.

[30] P.Mancini and H.D.Griffiths, "Non-reciprocal antenna pattern for SAR speckle reduction", IGARSS 1991, Espoo Finland, Vol.2, pp.1001-1004, June 1991.

[31] D.H.Hoekman, "An analysis of speckle from forest stands with periodic structures", IEEE Transactions on Geoscience and Remote Sensing, Vol.27, No.3, pp.316-325, May 1989.

[32] M.Born and E.Wolf, "Principles of Optics", Pergamon Press, New York, 1959.

[33] F.K.Li, C.Croft and D.N.Held, "Comparision of several techniques to obtain multiple-look SAR imagery", IEEE Transactions on Geoscience and Remote Sensing, Vol.GE-21, No.3, pp.370-375, July 1983.

[34] A.C.Schell, "The antenna as a spatial filter", in *Antenna Theory,* R.Collin and F.Zucker, eds. McGraw-Hill, New York,1969.

[35] W.M.Brown and L.J.Porcello, "An introduction to Synthetic Aperture Radar", IEEE Spectrum, pp.52-62, September 1969.

[36] W.Caputi, "Stretch: A time-transformation technique", IEEE Transactions on Aerospace and Electronic System, Vol.AES-7, No.2, pp.269-278, March 1971.

[37] B.C.Barber, "Theory of digital imaging from orbital Synthetic Aperture Radar", International Journal of Remote Sensing, Vol.6, N.7, pp.1009-1057, 1985.

[38] G.P.Konnen, "Polarized light in nature", Cambridge University Press, Cambridge, U.K., 1985.

[39] W.M.Boerner and W.L.Yan, "Introduction to Radar Polarimetry", Conference Proceedings of Journees Internationales de la Polarimetrie Radar, Nantes, France, March 1990.

[40] A.B.Kostinski and W.M.Boerner, "On Foundations of Radar Polarimetry", IEEE Transactions on Antennas and Propagation, Vol.AP-34, No.12, pp.1395-1404, December 1986.

[41] M.Born and E.Wolf, "Principles of Optics", Pergamon Press, New York, 1964.

[42] F.T Ulaby and C.Elachi, "Radar Polarimetry for Geoscience Applications", Artech House, April 1990.

[43] H.C.van de Hulst, "Light scattering from small particles", Dover, New York, 1981.

[44] L.Tsang, J.A.Kong and R.T.Shin, "Theory of Microwave Remote Sensing", Wiley-Interscience, New York, 1985.

[45] J.J.Van Zyl, C.H.Papas and C.Elachi, "On the optimum polarizations of incoherently reflected waves", IEEE Transactions on Antennas and Propagation, Vol.AP-35, No.7, pp.818-825, July 1987.

[46] A.Guissard, "The Mueller matrix in radar polarimetric measurements", IGARSS 1993, Tokyo Japan, Vol.1, pp.371-373, August 1993.

[47] J.J.Van Zyl, H.A.Zebker and C.Elachi, "Imaging radar polarization signatures: Theory and observation", Radio Science, Vol.22, No.4, pp.529-543, July-August 1987.

[48] S.R.Cloude, "Vector scattering theory and polarimetry", Conference Proceedings of Journees Internationales de la Polarimetrie Radar, Nantes, France, March 1990.

[49] P.Beckman and A.Spizzichino, "The scattering of electromagnetic waves from rough surfaces", Pergamon Press, Oxford, 1963.

[50] M.Borgeaud, R.T.Shin and J.A.Kong, "Theoretical models for polarimetric radar clutter", Journal of Electromagnetic Waves and Applications, Vol.1, No.1, pp.73-89, 1987.

[51] M.Zuniga, J.A.Kong and L.Tsang, "Depolarization effects in active remote sensing of random media", Journal of Applied Physics, Vol.51, pp.2315-2325, May 1980.

[52] R.K.Raney, A.L.Gray and J.G.Princz, "An effect of coherent scattering in spaceborne and airborne SAR images", International Journal of Remote Sensing, Vol.9, No.5, pp.1039-1049, 1988.

[53] G.De Grandi, "Performance tuning of the Sun Unix implementation of the NASA JPL compression algorithm for multipolarisation SAR data", JRC, ISPRA, internal memorandum.

[54] H.A.Zebker, J.J.Van Zyl and D.N.Held, "Imaging Radar Polarimetry from wave synthesis", Journal of Geophysical Research, Vol.92, No.B1, pp.683-701, January 1987.

[55] J.J.Van Zyl, "Unsupervised classification of scattering behaviour using radar polarimetry data", IEEE Transactions on Geoscience and Remote Sensing, Vol.27, No.1, pp.36-45, January 1989.

[56] R.B.Dybdal and R.H.Ott,."Coherent RF error statistics", IEEE Transactions on Microwave Theory and Techniques, Vol.MTT-34, No.12, pp.1413-1419, December 1986.

[57] R.A.Cordey, "Preliminary Studies of Calibration and Applications of Complex Multipolarisation SAR Images", GEC-Marconi Research Centre, ITM 90/32, Section 218, May 1990.

[58] J.J.Van Zyl, "Calibration of polarimetric radar images using only image parameters and trihedral corner reflector responses", IEEE Transactions on Geoscience and Remote Sensing, Vol.28, No.3, pp.337-348, May 1990.

[59] G.R.Valenzuela, "Theories for the Interaction of Electromagnetic and Oceanic Waves-A Review", Boundary Layer Meteorology, Vol.13, pp.61-85, 1978.

[60] R.K.Raney, "A free 3 dB in Crosspolarized SAR data", IGARSS 1987, Ann Arbor USA, Vol.2, pp.565-569, May 1987.

[61] A.Freeman, "An algorithm for estimating the noise levels in polarimetric SAR image data", International Journal of Remote Sensing, Vol.15, No.9, pp.1791-1798, 1993.

[62] A.Guissard, "Phase calibration of polarimetric radars from slightly rough surfaces", IEEE Transactions on Geoscience and Remote Sensing, Vol.32, No.3, pp.712-715, May 1994.

[63] E.Wolf, "Coherence properties of partially polarised electromagnetic radiation", Il Nuovo Cimento, Vol.XIII, No.6, pp.1165-1181, September 1959.

[64] G.Strang, "Linear Algebra and Its Applications", New York Academic,1976.

[65] K.Tragl, "Optimal polarizations for reciprocal random targets", Direct and Inverse Methods in Radar Polarimetry, Part 1, pp.693-706, Kluwer Academic Publishers, The Netherlands, 1992.

[66] E.Luneburg, V.Ziegler, A.Schroth and K.Tragl, "Polarimetric Covariance matrix analysis of random radar targets", AGARD Conference Proceedings N.501 on "Target and Cutter scattering and their effects on military radar performance", September 1991.

[67] L.M.Novak and M.C.Burl, "Optimal speckle reduction in polarimetric SAR imagery", IEEE Transactions on Aerospace and Electronic Systems, Vol.26, No.2, pp.293-305, March 1990.

[68] L.M.Novak, M.C.Burl, R.D.Chaney and G.J.Owirka, " Optimal Processing of polarimetric Synthetic Aperture Radar Imagery", The Lincoln Laboratory Journal, Vol.3, No.2, pp.273-290, 1990.

[69] A.J.Poelman, "Cross correlation of orthogonally polarised backscatter components", IEEE Transactions on Aerospace and Electronic Systems, Vol.AES-12, No.6, pp.674-681, November 1976.

[70] S.L.Durden, J.J.Van Zyl and H.A.Zebker, "The unpolarised component in polarimetric radar observations of forested areas", IEEE Transactions on Geoscience and Remote Sensing, Vol.28, No.2, pp.268-271, March 1990.

[71] D.Giuli, "Polarization diversity in Radars", Proceedings of the IEEE, Vol.74, No.2, pp.245-267, February 1986.

[72] S.R.Cloude, "Polarimetric optimisation based on the target Covariance matrix", Electronics Letters, Vol.26, No.20, pp.1670-1671, September 1990.

[73] A.A.Swartz, H.A.Yueh, J.A.Kong, L.M.Novak and R.T.Shin, "Optimal Polarisations for achieving maximum contrast in radar images", Journal of Geophysical Research, Vol.93, No.B12, pages 15252-15260, December 1988.

[74] K.Fukunaga, "Introduction to Statistical Pattern Recognition", Academic Press, New York, 1972.

[75] S.M.Verbout, C.M.Netishen and L.M.Novak, "Polarimetric Techniques for enhancing SAR imagery", MIT Lincoln Laboratory, Air Force contract F19628-90-C-0002.

[76] J.A.Cadzow, "Generalized digital matched filtering", Proceedings 12th Southeastern Symposium on System Theory, Virginia Beach, VA, 19-20 May 1980.

[77] J.W.Goodman, "Statistical Optics", New York, Wiley, 1985.

[78] S.Quegan, "Cross talk calibration of the MAESTRO data from the Reedham and Feltwell test sites", Proceedings Maestro Final Workshop, Noordwijk, The Netherlands, February, 1992.

[79] E.Rignot and R.Kwok, "Characterization of spatial statistics of distributed targets in SAR data", International Journal of Remote Sensing, Vol.14, No.2, pp.345-363, 1993.

[80] F.L.Posner, "Texture and speckle in high resolution Synthetic Aperture Radar", IEEE Transactions on Geoscience and Remote Sensing, Vol.31, No.1, pp.192-203, January 1993.

[81] F.T.Ulaby, F.Kouyate, B.Brisco and T.H.L. Williams, "Textural information in SAR images", IEEE Transactions on Geoscience and Remote Sensing, Vol.GE-24, No.2, pp.235-245, March 1986.

[82] W.W.Irving, G.J.Owirka and L.M.Novak, "A new model for high resolution polarimetric SAR clutter data", Proceedings SPIE, Synthetic Aperture Radar, Vol.1630, pp.208-223, Los Angeles, 1992.

[83] L.M.Novak, M.B.Sechtin and M.J.Cardullo, "Studies of target detection algorithms that use polarimetric SAR data", IEEE Transactions on Aerospace and Electronic Systems, Vol.AES-25, No.2, pp.150-165, March 1989.

[84] "Poltool, User's guide", Commission of European Communities, JRC ISPRA IRSA, 1990.

[85] J.D.Klein and A.Freeman, "Design considerations for an advanced multipolarisation SAR", IGARSS 1988, Edinburgh, Scotland, Vol.2, pp.317-321, September 1988.

[86] R.A.Cordey, "Study of system crosstalk requirements for a polarimetric spaceborne SAR", Interim Report, ESTEC contract No.103505, February 1991.

[87] S.R.Cloude, "The importance of polarisation information in Optical Remote Sensing", SPIE, Vol.810, Optical Systems for Space Applications, pp.21-27, 1987.

[88] J.J.Van Zyl, "The effect of topography on radar scattering from vegetated area", IEEE Transactions on Geoscience and Remote Sensing, Vol.31, No.1, pp.153-160, January 1993.

[89] T.Le Toan and J.A.Kong, "Microwave interaction and analysis of polarimetric data: retrieval of forest biomass", ESTEC contract No.9352/91/NL/LC, December 1992.

[90] S.L.Durden, J.D.Klein and H.A.Zebker, "Polarimetric Radar measurements of a forested area near mt.Shasta", IEEE Transactions on Geoscience and Remote Sensing, Vol.29, No.3, pp.444-450, May 1991.

[91] H.A.Zebker, J.J.Van Zyl, S.L.Durden and L.Norikane, "Calibrated imaging radar polarimetry: technique, examples and applications", IEEE Transactions on Geoscience and Remote Sensing, Vol.29, No.6, pp.942-961, November 1991.

[92] G.G.Lemoine, "On polarimetric signatures", IGARSS 1992, Houston Texas, Vol.2, pp.913-915, May 1992.

[93] P.Mancini and H.D.Griffiths, "On the use of the Covariance matrix in polarimetric SAR", Second International Workshop on Radar Polarimetry, IRESTE, Nantes, pp.225-232, September 1992.

[94] P.Mancini and H.D.Griffiths, "Texture analysis in polarimetric SAR using the Covariance matrix", IGARSS 1992, Houston Texas, Vol.2, pp.893-895, May 1992.

[95] A.Freeman, J.Villasenor, J.D.Klein, P.Hoogeboom and J.Groot, "On the use of multi-frequency and polarimetric radar backscatter features for classification of agricultural crops", International Journal of Remote Sensing, Vol.15, No.9, pp.1799-1812, 1994.

[96] A.J.Blanchard and B.R.Jean, "Antenna effects in depolarisation measurements", IEEE Transactions on Geoscience and Remote Sensing, Vol.GE-21, No.1, pp.113-117, January 1983.

[97] D.H.Lukert and A.J.Blanchard, "Azimuth depolarisation in Synthetic Aperture Radar", International Journal of Remote Sensing, Vol.9, No.3, pp.527-542, 1988.

[98] R.K.Raney and J.Princz, "Reconsideration of azimuth ambiguities in SAR", IGARSS 1986, Zurich Switzerland, Ref. ESA SP-254, pp.1175-1178, September 1986.

[99] I.G.Cumming, P.F.Kavanagh and M.R.Ito, "Resolving the Doppler ambiguity for spaceborne Synthetic Aperture Radar", IGARSS 1986, Zurich Switzerland, Ref. ESA SP-254, pp.1639-1643, September 1986.

[100] R.Cordey and P.Mancini, "Range ambiguities for a Polarimetric Spaceborne SAR", IGARSS 1992, Houston Texas, Vol.1, pp.637-640, May 1992.

[101] P.Mancini and H.D.Griffiths, "On-board polarimetric processing for Synthetic Aperture Radar", IGARSS 1991, Espoo Finland, Vol.1, pp.295-297, June 1991.

[102] D.Giuli, L.Facheris, M.Fossi and A.Rossettini, "Simultaneous Scattering matrix measurements through signal coding", Proceedings IEEE International Conference, RADAR-90, pp.258-262, Washington 1990.

[103] F.K.Li and R.M.Goldstein, "Studies of multi-baseline spaceborne interferometric Synthetic Aperture Radar", IEEE Transactions on Geoscience and Remote Sensing, Vol.28, No.1, pp.88-97, January 1990.

[104] R.M.Barnes, "Roll-Invariant decompositions of the Polarisation Covariance matrix", MIT, Lexington, MA 02713-0073, 1988.

[105] W.A.Holm and R.M.Barnes, "On radar polarisation mixed state decomposition theorems", Proceedings of 1988 USA National Radar Conference, pp.248-254, April 1988.

[106] S.R.Cloude, "Physical realisability of matrix operators in polarimetry", SPIE Vol.1166, Polarisation considerations for optical systems II, pp.177-185, August 1989.

[107] S.R.Cloude, "Uniqueness of target decomposition theorems in radar polarimetry", Direct and Inverse methods in Radar Polarimetry, Part 1, NATO-ARW, Eds. W.M.Boerner et al., Kluwer Academic publishers, ISBN 0-7293-1498-0, pp.267-296, 1992.

[108] S.V.Nghiem, S.H.Yueh, R.Kwok and F.K.Li, "Symmetry properties in polarimetric remote sensing", Radio Science, Vol.27, No.5, pp.693-711, September- October 1992.

[109] H.Mott, "Antennas for Radar and Communications", Wiley, 1992.

[110] J.J.Van Zyl, "Applications of Cloude's target decomposition theorem to polarimetric imaging radar data", SPIE, Vol.1748, Radar Polarimetry, pp.184-212, 1992.

[111] J.S.Lee and I.Jurkevich, "Speckle filtering of SAR images: a review", Remote Sensing Reviews, Vol.8, pp.313-340, 1994.